Insights into Velopharyngeal Closure Biomechanics Revealed using MRI and Computational Modeling

---

A Dissertation

Presented to

the faculty of the School of Engineering and Applied Science

University of Virginia

---

in partial fulfillment
of the requirements for the degree

Doctor of Philosophy

by

Catherine Marie Pelland

May 2019

APPROVAL SHEET

This Dissertation
is submitted in partial fulfillment of the requirements
for the degree of
Doctor of Philosophy

Author Signature: 

This Dissertation has been read and approved by the examining committee:

Advisor: Silvia S. Blemker

Committee Member: Matthew Panzer

Committee Member: George Christ

Committee Member: Patrick Cottler

Committee Member: Craig Meyer

Committee Member: Jamie Perry

Accepted for the School of Engineering and Applied Science:

Craig H. Benson, School of Engineering and Applied Science

May 2019

Insights into Velopharyngeal Closure Biomechanics Revealed using MRI and Computational Modeling

Catherine M. Pelland

Research is what I'm doing when I don't know what I'm doing.

- Wernher von Braun

Abstract

Healthy speech requires proper function of the velopharyngeal mechanism, which consists of the hard palate, velum (soft palate), lateral and posterior pharyngeal walls, and the musculature that drives movement of these structures. The function of the VP mechanism is to close the VP port, an orifice between the velum and pharyngeal walls, and completely separate the nasal and oral cavities. When the VP mechanism cannot achieve this closure, VP dysfunction results. In speech, VPD manifests as hypernasality, nasal air emission, and fatigue, in addition to frequent unintelligibility. VP dysfunction is a common occurrence for children with repaired cleft palate; approximately 1 in 1000 children are born with cleft palate and 25% have VP dysfunction after primary palate repair. VPD is also associated with 22q11.2 deletion syndrome, and VPD in this population is not easily treated. The critical barrier for prevention and effective treatment of VPD has been the primarily observational nature of studies examining the VP mechanism. Insights into VP function and its relationship with anatomy are limited by the number and types of measurements that are feasible *in vivo*, and causal relationships cannot be examined due to the sheer number of clinical cases required to isolate the effects of pre-repair or surgically reconstructed anatomy.

Our understanding of the complex relationship between VP structure and *in vivo* function remains limited. In this dissertation, I developed methods to empower this investigation. The levator veli palatini is the primary muscle of VP closure, so knowledge of its *in vivo* function is essential to understanding VP mechanics during speech. Therefore, I developed a method to measure LVP lengths and velocities during speech production using dynamic MRI. Results obtained using this method revealed that LVP shortening and contraction velocity scale with VP

port depth. In the 22q11.2 DS population, the relationship between anatomy and function is likely more complex than in healthy individuals. Simulations using a computational model optimized for anatomical parameter sensitivity revealed that LVP cross-sectional area is a disadvantageous feature in all 22q11.2 DS anatomies. However, no other anatomical measure was consistently disadvantageous for VP closure across all anatomies, supporting an anatomy-informed, rather than "one size fits all", approach to treatment of VPD in children with 22q11.2 DS. Finally, we do not understand how each muscle of the VP mechanism affects VP closure, which limits our ability to prevent and treat VPD. I developed a novel MRI-finite element modeling framework to probe the roles of two VP muscles – the palatopharyngeus and palatoglossus – in VP closure.

Ultimately, the framework developed in this dissertation integrates the wealth of literature with MRI-based anatomy and validation to provide new insights into VP biomechanics. Coupling imaging and computational modeling empowers us to unravel the complexities of the VP structure-function relationship and improve the lives of children born with cleft palate and those living with VPD.

Acknowledgements

For as long as I can remember, I planned to attend graduate school. But in all of my years of planning, I never imagined the surprising joys, innumerable doubts, sheer excitement of scientific discovery, or ever-present, never-ending “to do” list. This true rollercoaster of an experience has challenged and strengthened me in so many ways. None of this would have been possible without the many people who accompanied and supported me in this journey.

First, I would like to thank my advisor and friend, Silvia Blemker. I cannot imagine a more optimistic advisor who found excitement in seemingly mediocre data, supported my pursuit of opportunities, including a yearlong “research walkabout” to Australia, and always, always showed how much she cares about my life and well-being. The first time we met, we bonded over math parties (if you don’t know what those are, you are missing out!), and to this day, every time we meet, I discover something new we have in common. Thank you for taking a chance on a math major with no engineering background.

I also owe a great deal of my success to the rest of the Multiscale Muscle Mechanophysiology Lab (formerly the Multiscale Muscle Mechanics Lab). I cannot imagine graduate school without Katie K.’s research insights and friendship throughout the years. I am so grateful that we got over our uncharacteristic shyness at that first lab meeting to become Wine-and-Design buddies and Zumba Zisters. I also have to thank the third Zister in our trio, Vi, who is the kindest person I have had to privilege to know. You are a beacon of positivity, and I am very lucky to have you as my palate project co-worker. I want to thank Amanda for ordering our current lab chairs, in which I have spent far too many hours but have escaped mostly back pain-free, and for her friendship. Thank you to Xiao for answering random AMPS and other questions throughout the years and for being a model of productivity. I am also grateful to Brian for always answering questions about FEBio and providing excellent advice for random life things. To Hunter, thank you for being pseudo-lab manager and for the years of helpful comments. Thank you, Emily, for being M3’s statistics and cluster computing guru; my results were significantly better with your assistance. Thanks to Adrienne for useful comments throughout the years and especially for helping me convince children to willingly hop in the MR scanner and speak on cue. Ben, thanks for always smiling and brightening the lab. To Ridhi, thanks for being so upbeat and supportive (especially on weekends) and for letting me talk your ear off about Ireland. Matt, thanks for your positive energy and your well-timed, quick-witted comments. Finally, I must thank former members of the M3 Lab: Kelley for her friendship and constant productivity that I could only hope to match on my best days; Evan for his kindness and patience in all aspects of life, including softball; John for his friendliness and volleyball prowess; Shawn for his perspective on research, presentations, and beer at 3:30pm on a weekday; Josh for his many trips to Chick-fil-A and pioneering the palate project; Geoff for constantly leading “thought experiments” and always offering assistance when needed; and Nic for setting a very high bar for all M3 Lab graduate students and welcoming me to the lab when I wandered in for my interview many years ago.

Several people at UVA have made my graduate work more rigorous and impactful, especially the members of my committee, who always pushed me to think critically about every aspect of my research, which lead to great improvements in my work – Matt Panzer, Craig Meyer, Patrick Cottler, and George Christ. To Kathleen Borowitz, thank you for providing the speech pathology perspective throughout this project and for fun Indianapolis and Pittsburgh adventures. I also want to thank Kant Lin, who invited me to several cleft palate repairs during the start of this project and was always a fervent supporter. Finally, much of work I've completed during my time as a graduate student is possible only because of a collaboration with Jamie Perry. Thank you for sharing your knowledge, time, and resources and for your constant optimism about the direction of this project.

I also must thank the many subjects who volunteered (or were slightly compensated) for the studies in this dissertation. I very much appreciate your time and spent energy; these projects would not exist without you. I am also exceptionally grateful for my graduate funding sources: Clare Boothe Luce Graduate Fellowship (Henry Luce Foundation) and National Science Foundation Graduate Research Fellowship Program.

Graduate school is a long commitment made fun by the friends I've had along the way. Being an honorary member of the BME department allowed me to make and stay friends with some incredibly smart, talented, and caring people. I won't try to name all of you because I've been at UVA for so long and I'm bound to forget too many important friends in my dissertation-addled brain. You know who you are, and thank you for the martini nights, hours of Queer Eye, wine tastings, and so much more.

Outside of the department, I have an incredible community of support. To the last remaining members of Shock and Awe, thanks for being a bright spot in every week, win, lose, or draw. Although relatively new to my life, the Drinking Club with a Reading Problem is another beacon of fun not only because it forces me to read non-scientific books but also because I get to spend time with smart, talented, self-assured women. On the other end of the spectrum, thanks to the people I've known my entire life – my Hampden-Sydney and Farmville community. I wouldn't trade growing up in my small town for anything; knowing that a whole community of people were cheering me on and supporting me, no matter what, was always a comfort in times of doubt.

My mom, dad, and brother have been a constant source of support throughout my entire education, but especially during my PhD. There was never a time when you doubted my ability to succeed, even in my moments of utmost frustration and uncertainty. Every milestone, no matter how small, was to be celebrated (often with a trip to Disney World), and I cannot wait to celebrate this PhD milestone with all of you on our Alaskan cruise in two short months. Mom, all that'll be left is two states (one each), four Disney resorts, seven (?) MLB ballparks, and about a million places on our "to go" list.

Lastly, I have to thank my best friend and cat co-parent, Matt. This dissertation would not have been completed without you behind the scenes encouraging, entertaining, and often making food for me. Thank you for being the most supportive partner I could ever imagine.

Table of Contents

List of Figures

List of Tables

List of Equations

Chapter 1

Introduction

Nothing in life is to be feared, it is only to be understood.
Now is the time to understand more, so that we may fear less.

- Marie Curie

1.1 Overview

Speech is an integral part of everyday communication, but often overlooked is the complex coordination of muscles required to achieve healthy speech. In particular, proper function of the velopharyngeal (VP) mechanism is vital for healthy speech. The VP mechanism consists of the hard palate, velum (soft palate), posterior and lateral pharyngeal walls, and the musculature that drives movement of the passive soft tissues (Figure 1.1). The VP mechanism functions to completely close the velopharyngeal port, separating the nasal and oral cavities, during speech and swallowing. Five muscles insert into or are intrinsic to the velum; of these, the levator veli palatini (LVP) is the primary muscle of VP closure (20,67,82,111,169).

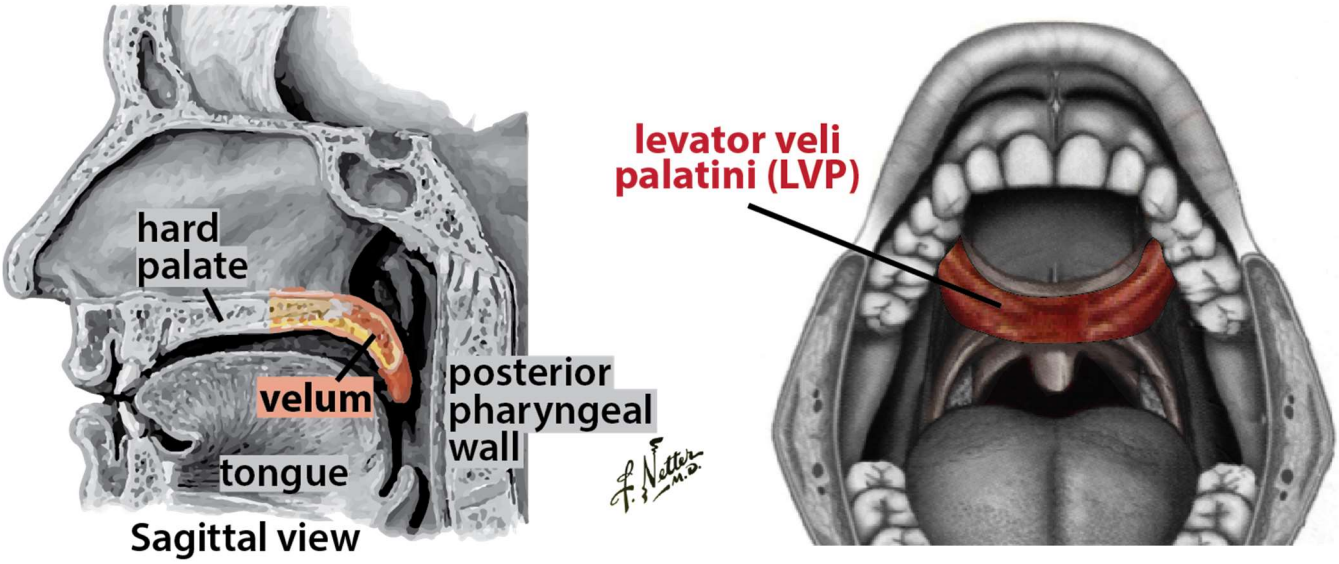

Figure 1.1 Velopharyngeal Mechanism Anatomy
The VP mechanism consists of the hard palate, velum, pharyngeal walls, and the associated musculature. The primary muscle of VP function is the levator veli palatini.

When the VP mechanism is unable to achieve consistent closure of the port, velopharyngeal dysfunction (VPD) occurs (Figure 1.2). This leads to hypernasality, nasal air emission, and fatigability during speech and often unintelligibility. VPD can result from a variety of causes, including genetic syndromes or cleft palate. The most common congenital cause of VPD is 22q11.2 deletion syndrome, and 75% of children with 22q11.2 DS have a velopharyngeal abnormality (31,95,194). Cleft palate is one of the most common birth defects in the United States (159), and 25% of children with repaired cleft palates have VPD (136).

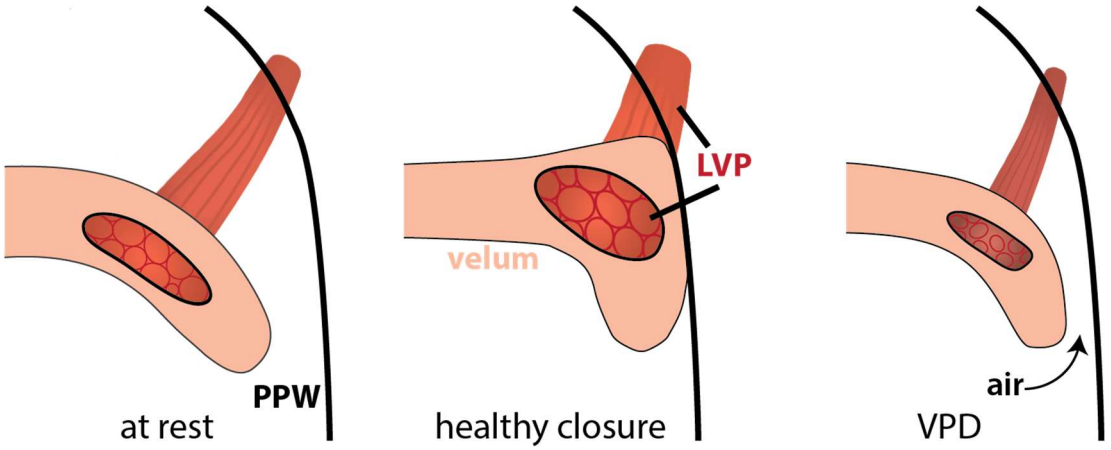

Figure 1.2 Velum at rest, Healthy closure versus closure in VPD
In a healthy anatomy, the VP port completely closes, separately the nasal and oral cavities. However, in velopharyngeal dysfunction (VPD), the VP port is not completely sealed, so air can escape into the nose and nasal cavity.

The critical barrier for preventing VPD has been the primarily observational nature of studies examining the VP mechanism in healthy individuals and those with VPD. These studies have amassed data on velopharyngeal anatomy (e.g. (10,59,68,82,98,103,106,158,169,185)), velum movement (e.g. (81,104,142,189)), muscle activations (e.g. (14,20,107,108,113,143)),

and VP closure force (e.g. (112,143,144)). However, insights into VP function and its relationship with anatomy are limited by the number and types of measurements that are feasible *in vivo*. Outcome studies have reported and compared surgical success rates (e.g. (48,152,176,197,204,225)) but cannot provide the underlying cause of surgical success or failure. Cause-and-effect relationships cannot be examined due to the sheer number of clinical cases required to isolate the effects of pre-repair or surgically reconstructed anatomy.

In both healthy speakers and individuals with VPD, the relationship between anatomy and VP function is not well understood. Previous studies have hypothesized that certain VP dimensional extrema exist, such as a minimum ratio between velum length and VP port dimensions (187), outside of which healthy speech is unachievable (173). These hypotheses are supported by imaging results demonstrating that individuals with VPD have significantly different anatomical dimensions than healthy speakers (68,103,167) and a computational modeling study highlighting the effect of VP port depth on closure (88). However, there is lacking data as to the anatomical dimensions and functional outcomes that constitute a healthy structure-function relationship and how this relationship differs in individuals with VPD. An increased understanding of this relationship is vital for prevention of VPD where possible (e.g. due to a failed cleft palate repair) and development of effective treatments for VPD.

We believe that investigation of the VP mechanism is an ideal opportunity to couple novel magnetic resonance imaging (MRI) techniques with computational modeling. With recent advances in MRI, we can capture VP anatomy with sufficient resolution to visualize all of the VP musculature or *in vivo* during natural speech production. These MRI methods not only expand our understanding of *in vivo* LVP function but also empower the use of computational models

to provide novel insights difficult to reveal with experimental methods alone. Computational models can be used to determine cause-and-effect relationships, ask “what if” questions, and generate new hypotheses to advance the study of VP function in healthy individuals and individuals with VPD.

The levator veli palatini (LVP) is known to be the primary muscle of VP closure, but our knowledge of LVP behavior during speech is limited, even in healthy individuals. *In vivo* LVP function determines the possible LVP force generation due to the force-length and force-velocity relationships of skeletal muscle (12,36,51,66,78,84,180). Therefore, evaluation of *in vivo* lengths and velocities is critical to an increased understanding the VP structure-function relationship. In Chapter 2, we developed a new method to quantify LVP muscle lengths and velocities during speech using dynamic MRI. Using our method, we demonstrated that LVP shortening and contraction velocities differ between sounds in healthy individuals. These LVP functional measures correlated with VP port depth, suggesting that an individual’s VP anatomy influences *in vivo* function in healthy speech.

In a clinical population, such as children with 22q11.2 DS, how do alterations in VP anatomy affect function? There are inconsistent findings about how VP anatomy differs in patients with 22q11.2 DS compared to healthy individuals (45,56,77,97,185,215,226), but the importance of these anatomical alterations is how they affect functional outcomes. In Chapter 3, we adapted an existing computational modeling framework to investigate the effect of anatomic variability on VP closure in children with 22q11.2 DS and how that closure differs from healthy children. We first showed that this framework was able to distinguish between healthy and 22q11.2 DS anatomies. We then used the model to probe which features in

22q11.2 DS anatomies most affect VP closure. The model predicted that LVP cross-sectional area most disadvantaged closure in all 22q11.2 DS anatomies. However, comparable changes in anatomic measures affect VP closure to different degrees, and not every 22q11.2 DS anatomy is affected in the same way. These results support a clinical approach where patient anatomy is considered when devising surgical intervention for VPD in all patients but especially those with 22q11.2 DS.

We first focused on the LVP as the primary muscle of VP closure, but in addition to the LVP, there are four other muscles of the VP mechanism: musculus uvulae, tensor veli palatini (TVP), palatopharyngeus, and palatoglossus. Electromyography (EMG), anatomical dissection, and computation modeling studies have shown that the musculus uvulae is a space occupier and velar extensor, which assists the LVP in achieving VP closure (8,26,86,108,165,205). Previous work suggests that the stiffness in the anterior velum from the TVP tendon benefits VP closure, but TVP muscle activation has little effect on velum movement (13,80). However, how the palatopharyngeus and palatoglossus affect VP function is not fully understood. Isolating the contributions of each muscle is challenging using experimental methods alone. Therefore, in Chapter 4, we constructed a finite element model of the VP mechanism to probe the roles of the palatopharyngeus and palatoglossus muscles in VP function. Our simulations predicted that palatoglossus, and to a lesser extent, the palatopharyngeus, act as LVP antagonists, but the effect of both muscles' contraction is dependent on the current state of LVP activation.

Ultimately, we developed a novel framework to investigate the VP mechanism that combines MRI and computational modeling. Both imaging and modeling results demonstrate the effect of VP anatomy, especially VP portal dimensions, on LVP function and consequently

VP function and speech. We also hypothesize that the roles of the LVP antagonist muscles vary based on velum position and are likely context dependent, as previously postulated (107,145,189). Lastly, which we discuss in Chapter 5, this imaging-modeling framework lays the foundation for investigation of VP mechanics in other populations, especially individuals with repaired cleft palate.

1.2 Background

1.2.1 Velopharyngeal Mechanism Anatomy

The velopharyngeal (VP) mechanism consists of the bony hard palate, velum (soft palate), lateral and posterior pharyngeal walls, and associated musculature (Figure 1.3). The orifice between the velum and pharyngeal walls is called the VP port. The muscles of the VP mechanism coordinate to close the VP port, which completely separates the nasal and oral cavities. This complete closure of the VP port is required for production of oral speech sounds. (Only three sounds in English are produced properly without VP port closure.) In healthy individuals, elevation and retraction of the velum accounts for the majority of VP port closure (163). Anteriorly, the velum is attached to the posterior edge of the hard palate, called the posterior nasal spine (PNS). The velum is a passive soft tissue composed of tendinous, muscular, adipose, connective, and glandular tissue (53,110), that courses from the PNS to the uvula. Velum displacement and deformation toward the posterior pharyngeal wall is caused primarily by levator veli palatini (LVP) muscle contraction. Thus, the LVP is the primary muscle of VP closure (20,67,82,111,169). The LVP consists of two muscle bundles, each of which originate on the petrous portion of the temporal bone (82). The two LVP halves course

anteriorly, inferiorly, and medially to insert into the velum, where they interdigitate to form the LVP sling (26).

The second of five VP muscles is the musculus uvulae, which is intrinsic to the velum and courses posteriorly from the anterior velum along the nasal surface of the velum. The musculus uvulae adds bulk to the nasal surface of the velum to maximize contact between the velum and posterior pharyngeal wall (8,83). In isolation, the musculus uvulae can minimally extend the velum, and activation of the musculus uvulae reduces the LVP activation necessary to achieve touch closure (86). Thus, the musculus uvulae assists the LVP in achieving VP closure by acting as a space occupier and velar extensor (86,108,205).

The tensor veli palatini (TVP) muscle originates at the base of the medial pterygoid plate of the sphenoid bone and the lateral edges of the Eustachian tube (1,13). The path of the TVP runs nearly parallel to the LVP path, coursing medially and inferiorly until the hook of the hamulus. The TVP muscle terminates in a tendon that courses around the hamulus and inserts into the anterior velum to form the palatal aponeurosis. This aponeurosis stiffens the anterior velum posterior to the hard palate and acts as a buffer between the soft velar tissue and bony hard palate (163). Contraction of the TVP muscle has been suggested to tense and slightly depress the anterior velum, which would aid in VP closure (1,49,70). However, TVP stimulation resulted in negligible velum movement (80), and an anatomic study observed that the TVP inserts on the hamulus (13), limiting the effect of TVP contraction on velar movement. Despite these disagreements, the stiffness in the anterior velum from the TVP tendon that limits anterior velum elevation is agreed to be advantageous for VP closure.

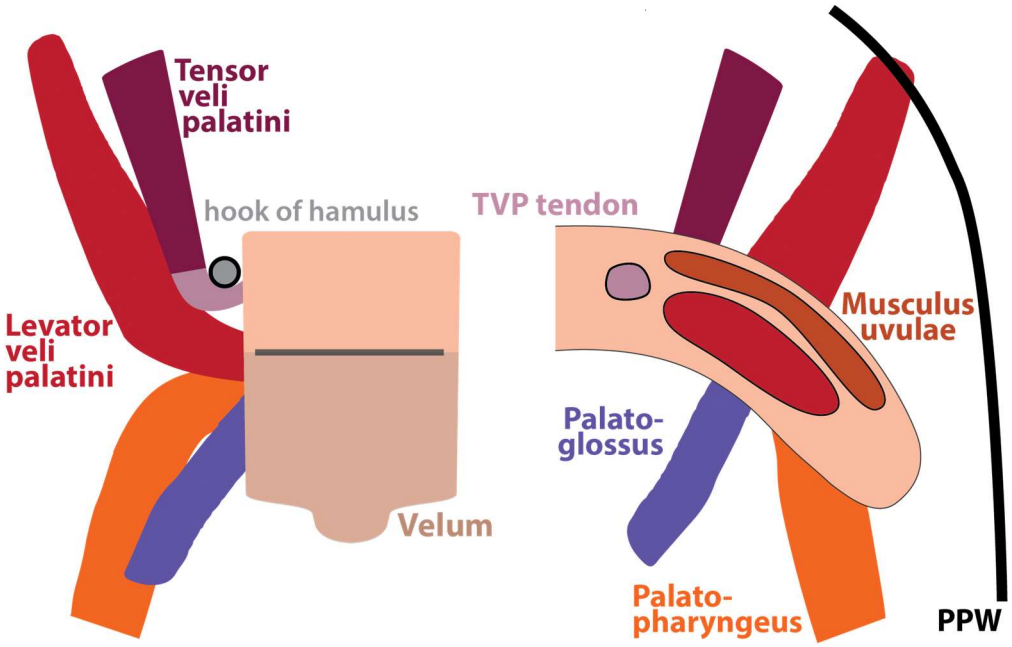

Figure 1.3 Five muscles of the velopharyngeal mechanism

At rest, both the palatopharyngeus and palatoglossus muscles are positioned anatomically as antagonists to the LVP muscle (82,130,206). The palatopharyngeus is oriented primarily vertically and courses inferiorly from the velum to insert into the lateral pharyngeal walls. The palatopharyngeus is generally agreed to be more active during swallowing than speech (163), but given the anatomic orientation of the palatopharyngeus, anatomic and EMG studies postulate that palatopharyngeus contraction adjusts velum position during elevation (107,189). The palatoglossus muscle courses from the lateral velum to insert into the lateral aspect of the tongue and has been shown to be active (131) and inactive (20) in velum lowering. An EMG study reported that both muscles coactivate with the LVP and suggested that they position the tongue and velum during speech. However, muscle activity for both muscles was to be found to be more variable than that of the LVP and possibly sound-specific (145).

1.2.2 Velopharyngeal Dysfunction

Velopharyngeal dysfunction (VPD) is a condition in which the VP mechanism cannot close the VP port consistently or completely when closure is required, e.g. during oral speech production (Figure 1.4). VPD manifests as hypernasality, nasal air emission, and other speech impairments in which air escapes from the oral cavity into the nasal cavity or nose during speech (156,196). Speakers with VPD can become fatigued and are often unintelligible. Additionally, individuals with hypernasal resonance disorders tend to be perceived as less intelligent, less reliable, and less kind than those with normal resonance and even those with other voice disorders (117).

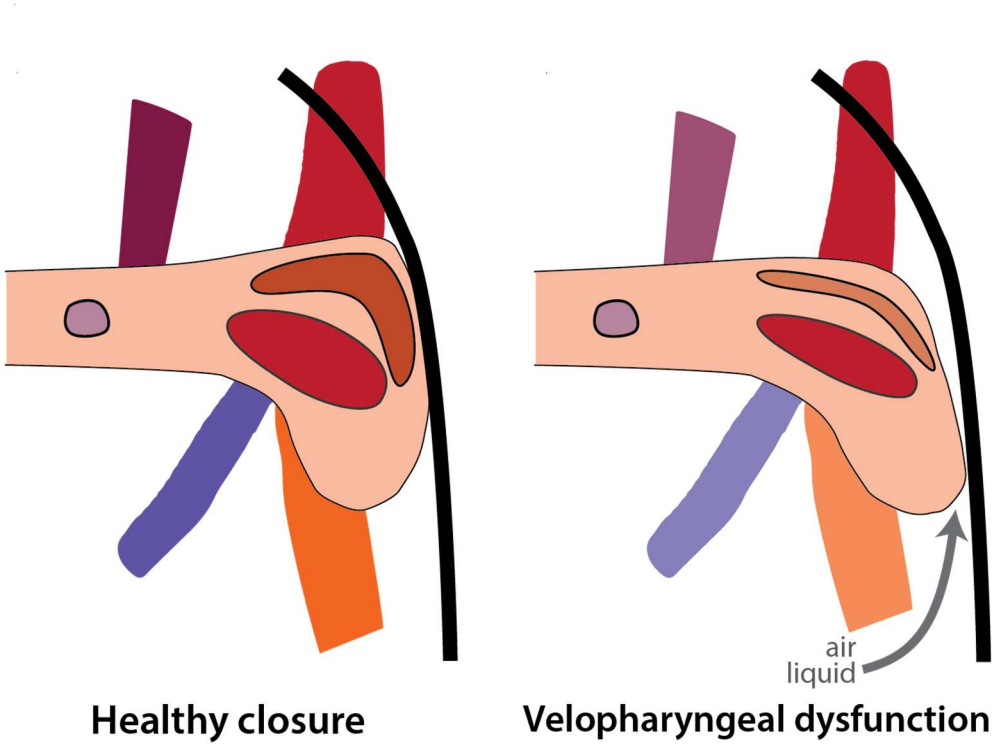

Figure 1.4 Healthy closure and Velopharyngeal dysfunction with all 5 muscles
The VP mechanism can complete close the VP port in a healthy speaker, but not in an individual with velopharyngeal dysfunction (VPD). During speech, air can escape from the oral cavity into the nasal cavity and nose to cause hypernasality and nasal air emission.

The term VPD does not attempt to suggest the cause of incomplete VP closure (115,224) and encompasses three types of disorders. VP insufficiency is caused by an anatomic or structural defect that prevents complete closure, such as a velum that is too short to sufficiently reach the posterior pharyngeal wall (224). VP insufficiency is the most common type of VPD (115). The second disorder, VP incompetence, is due to neuromuscular causes that lead to poor mobility of the VP structures. Lastly, VP mislearning is a behavioral condition that leads to misarticulation during specific sounds. The VP mechanism is capable of completely closing the VP port consistently but remains partially open during speech production. This dissertation is primarily concerned with VP insufficiency and VP incompetence, as these are structural or neuromuscular disorders that cannot be successfully treated with speech therapy alone. These disorders require surgical or prosthetic intervention. The most common surgical options are pharyngeal flap and sphincter pharyngoplasty, both of which decrease the size of the open VP port (224). In the case of VPD due to failed cleft palate repair, surgical options also include Furlow palatoplasty (32,162,195) and palatal re-repair (198,199). VP mislearning, on the other hand, is successfully treated only by speech therapy. Of note, however, is that many individuals with VP insufficiency develop misarticulations (VP mislearning) to compensate for the inability to achieve VP closure (196) and require speech therapy even after the structural defects have been repaired.

The most common cause of VP insufficiency is failed cleft palate repair (115). Approximately one in 1000 children are born with cleft palate, making it one of the most common birth defects in the United States (159). Children born with cleft palate undergo surgery typically between six and twelve months of age with the goal of reconstructing the

altered VP anatomy to promote proper function (Figure 1.5). Between 20 and 30% of patients with repaired cleft palate will have VPD (137,181,222). At present, the type of cleft palate repair surgery is based on surgeon preference, rather than patient anatomy. Reconstruction of the LVP sling is a primary goal of primary repair (118), but the other muscles are rarely, if ever, considered during repair. Some surgical techniques involve fracturing the hamulus to release the TVP (42,47,93,153), and it is unknown how the VP muscles, other than the LVP, are reoriented during surgery. Although not the focus of this dissertation, we believe the framework introduced here will promote the development of surgical plans based on patient anatomy that optimize structure and function post-surgery.

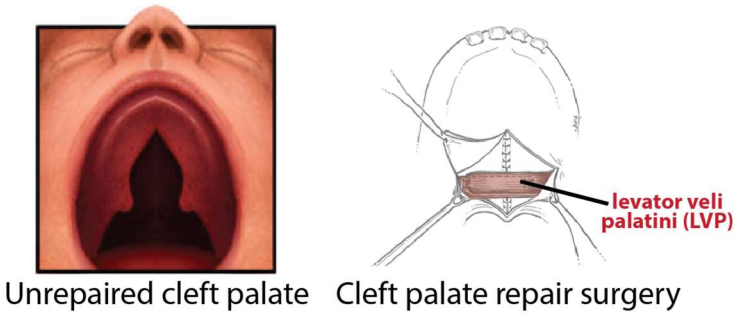

Figure 1.5 Unrepaired cleft palate (before surgery) and cleft palate repair surgery
VP anatomy, primarily levator veli palatini (LVP), is reconstructed to promote healthy function

VPD can also result from a genetic syndrome, such as 22q11.2 deletion syndrome, also known as velocardiofacial syndrome. 22q11.2 DS is caused by a chromosomal deletion and affects approximately one in 4000 births (15,18). The phenotypes of 22q11.2 DS vary from patient to patient, but 75% of children with 22q11.2 DS have a palatal anomaly (31) and 22q11.2 DS is the most common congenital cause of VPD (95,194). Hypernasality is a common

indicator of 22q11.2 DS and can be due to a variety of VP anatomical anomalies, including but not limited to cleft palate (18). Treatments for VPD in the 22q11.2 DS population are generally less successful than in non-syndromic cases (16,43,129,141,201). This is due in part to the complex etiologies of VPD in children with 22q11.2 DS and the difficulty distinguishing the structural causes of VPD from the neuromuscular causes (18,96).

1.2.3 Magnetic Resonance Imaging to Evaluate Velopharyngeal Anatomy and Function

Before rapid advances in magnetic resonance imaging (MRI) over the past 30 years, our knowledge of VP anatomy came primarily from anatomical dissection (111). However, VP anatomy is not accessible without disturbing the overlying tissues, so anatomical landmarks can be destroyed and relative locations distorted. In addition, dissection does not allow for the study of VP anatomy in living subjects.

MRI allows for visualization of the VP structures of interest in living subjects without disturbing tissues superficial to the VP structures. Since development of these sequences, VP anatomy has been studied extensively using MRI in healthy adults (e.g. (10,54,164,169,171, 172)), healthy children (e.g. (100,166,173)), children born with repaired cleft palate before and after primary repair (e.g. (106,173,174,210)), adults with repaired cleft palate (e.g. (68,103, 167)), and in individuals with 22q11.2 deletion syndrome (e.g. (56,98,158)). These imaging data sets have promoted discovery of a sex-related differences in LVP length measures in adults that do not appear consistently in pre-pubescent children, as well as race-related differences in velar length and thickness in children and adults (101,166,171,172). These MRI studies have also revealed that adults with repaired cleft palate have shorter and thinner LVP muscles with more acute angles of origin, shorter and thinner velum, shorter and smaller musculus uvulae

muscles, and greater pharyngeal depths than healthy adults (68,103,165,167). Three-dimensional (3D) sequences are the current gold standard when acquiring MRI data for study of VP anatomy. 3D image sequences can be post-processed to identify planes containing the structures of interest (175), rather than depending on correct selection of imaging plane during two-dimensional acquisition, which can be challenging and time-consuming, as 3D data sets.

Rapid acquisition MRI techniques allow for visualization of VP structures during speech production (6,9,19,50,91,175,193), but thus far, dynamic MRI has been limited primarily to research. Clinically, nasopharyngoscopy and videofluoroscopy are used to assess VP function (175,223). Nasopharyngoscopy provides a top-down view of the VP port during speech but with possible camera distortion (177); it allows for excellent qualitative evaluation of speech, but quantitative information is not feasible. Videofluoroscopy requires exposure to radiation and is limited to the midsagittal plane. Neither modality allows for visualization or measurement of the LVP muscle during speech.

Dynamic MRI is not limited to a specific plane and allows the user to choose the imaging plane best suited for the current investigation. Four imaging planes have been recommended for optimal study of VP function (50,175): mid-sagittal to evaluate velum elevation, frontal to assess lateral pharyngeal wall motion, axial to view the VP port, and oblique-coronal to visualize the LVP during VP function. Ideally, dynamic MRI would be captured three-dimensionally in real time to assess multiple planes simultaneously. Although this is not yet achievable, simultaneous acquisition of two intersecting planes during real-time speech production has been demonstrated for the mid-sagittal and oblique-coronal planes (55). Simultaneous images in

these two planes promotes investigation of *in vivo* LVP muscle function and its effect on velum elevation.

With dynamic MRI, there is a trade-off between temporal resolution, spatial resolution, and signal-to-noise ratio (125). Most of the VP structures are small, so small variations in structure size or location could be important to function; therefore, optimal in-plane spatial resolution is under 2 x 2 mm^2 (125). Frame rate is of particular importance when imaging VP function, as the velar elevation can occur in under 100 milliseconds (104). Many of the first MRI studies to assess VP function had frame rates under 6 frames per second, requiring the use of sustained phonation (e.g. (3,54,92,214)). While nasopharyngoscopy and videofluoroscopy produce video displays (175), dynamic MRI collects images at distinct time points. Therefore, the minimum frame rate for effective imaging is 10-20 frames-per-second (150,175,207). Gated sequences have been used to increase frame rate (91,94,193), but differences between repetitions of a speech sample limit the use of gated sequences for evaluation of VP function during speech (151). Frame rates over 100 frames-per-second have been achieved (60,61) but required an in-plane spatial resolution larger than sequences with frame rates between 15.8 and 30 frames-per second that fulfill recommended spatial resolution requirements (55,175).

1.2.4 Computational Modeling of the Velopharyngeal Mechanism

The velopharyngeal (VP) mechanism demonstrates complex morphological changes *in vivo* that benefit from investigation with a three-dimensional (3D) modeling framework. Although observational and experimental studies have generated tremendous insights into VP function (e.g. (90,101,166,175,211)), there are limits to the types and quantity of data these methods can provide. Computational modeling is a powerful tool that can integrate the wealth

of literature describing the VP mechanism to investigate cause-and-effect relationships, ask "what if" questions, and isolate the effect of specific parameters on function. The type of modeling framework used can be optimized for the relationships being investigated.

Understanding velum and VP muscle deformation is crucial to interpretation of VP function; to represent the velum shape changes observed during speech production, we utilize 3D finite element modeling. The first two finite element modeling investigations of the VP mechanism were limited to two dimensions and used vector forces to represent muscle contributions (22,203). Insights from these models and experimental studies examining velum and VP port configurations during closure (e.g. (89,142,179)) demonstrated the importance of 3D representations of the VP mechanism that include the velum, posterior wall, and musculature.

In our 3D finite element models, we model each of the VP muscles as a transversely isotropic, hyperelastic, nearly incompressible material (24). In hyperelastic materials, stress and strain are related by:

$$\boldsymbol{S} = 2\frac{\partial W}{\partial \boldsymbol{C}} \qquad \textbf{(Equation 1.1)}$$

where $\boldsymbol{S}$ is the second Piola-Kirchoff stress tensor, W is the strain energy density function, and $\boldsymbol{C}$ is the right Cauchy-Green strain tensor. This constitutive model uses an uncoupled form of strain energy to simulate near-incompressibility (216). The model separates the dilatational (volumetric) and deviatoric (distortional) tissue responses (217) and utilizes physically-based strain invariants (Figure 1.6) that relate material parameters to physically meaningful measures (39), resulting in the following strain energy density function:

$$W(\lambda, \alpha, B_1, B_2, J) = W_{vol}(J) + W_{dev}(\lambda, \alpha, B_1, B_2)\ . \qquad \textbf{(Equation 1.2)}$$

Volume changes are penalized in the volumetric portion of the strain energy density function (W_{vol}), where K is the bulk modulus and J is the relative change in volume:

$$W_{vol}(J) = \frac{K}{2}\ \ln(J)^2 \qquad \textbf{(Equation 1.3)}$$

The first term of the deviatoric component of the strain-energy density function (W_{dev}) represents the strain energy due to along fiber stretch (λ) and muscle activation (α). Muscle activation (α) scales the force-length relationship of muscle fibers (f_{active}) and is added to the passive force ($f_{passive}$) determined by fiber length (λ). W_1 assumes a peak isometric stress (σ_{max}) that occurs at optimal fiber length (λ_{OFL}). The deviatoric component of the strain energy density function (W_{dev}) includes the contributions from along-fiber shear (B_1) and cross-fiber shear (B_2), where G_1 and G_2 are the along-fiber and cross-fiber shear moduli, as shown below:

$$W_{dev}(B_1, B_2, \lambda, \alpha) = W_1(\lambda, \alpha) + G_1 B_1^2 + G_2 B_2^2 \qquad \textbf{(Equation 1.4)}$$

where $$\lambda \frac{dW_1}{d\lambda} = \sigma_{max}\left[f_{passive}(\lambda) + \alpha \cdot f_{active}(\lambda)\right] \frac{\lambda}{\lambda_{OFL}} \qquad \textbf{(Equation 1.5)}$$

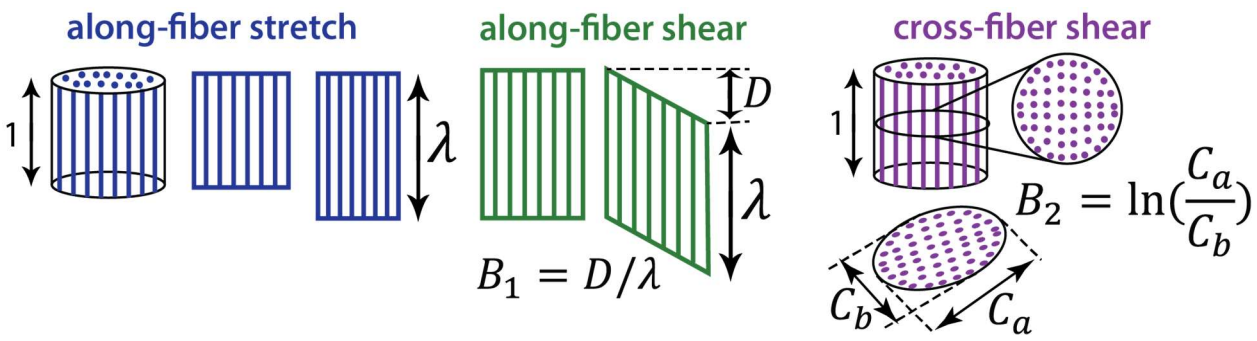

Figure 1.6 Physically-based strain invariants

Two previous studies of the VP mechanism implemented this constitutive model to represent muscle in finite element simulations of VP closure (86,87). The first study examined the effect of LVP overlap on VP closure force with a model of the velum, posterior pharyngeal wall, and LVP muscle and validated with literature closure force data (87). The other study quantified the effect of musculus uvulae activation on VP closure by comparing VP closure simulations in models with and without inclusion of the musculus uvulae (86). Both studies provided new insight into VP function but had geometries based primarily on average adult anatomical measurements, rather than subject-specific geometry and validation.

Computational models based on subject geometry have simplified LVP and other VP structure geometry to investigate various aspects of VP or upper airway function (88,126–128). Inouye et al. used a geometric model of the LVP, velum, and posterior pharyngeal wall, which we adapt in Chapter 3, to probe the effects of anatomy on healthy VP closure in adults (88). 3D models of the upper airway that include the velum have been built with subject-specific geometry to investigate obstructive sleep apnea, but the muscles were either not included or grouped together in one mid-velar layer (126–128).

Chapter 2

A Dynamic MRI-Based Method to Examine *In Vivo* Levator Veli Palatini Muscle Function during Speech

Acknowledgements: Xue Feng, Kathleen C. Borowitz, Craig H. Meyer, Silvia S. Blemker

XKCD – The General Problem

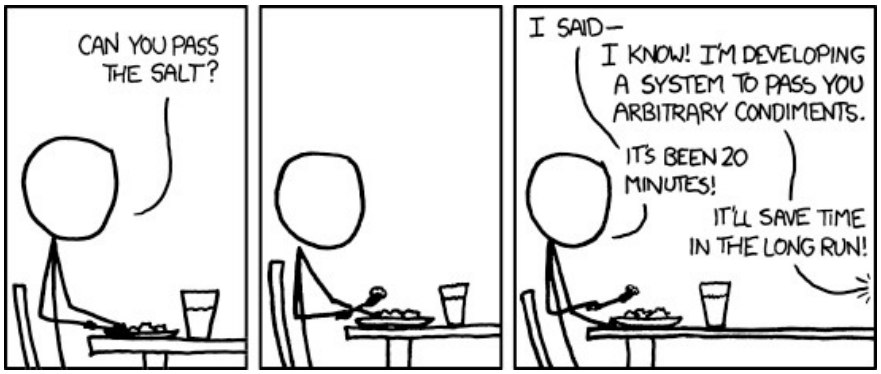

2.1 Abstract

Purpose: To develop a method able to quantify levator veli palatini (LVP) muscle shortening and contraction velocities using dynamic magnetic resonance imaging (MRI) throughout speech samples and relate these measurements to velopharyngeal portal dimensions.

Method: Six healthy adults (three males and three females, *M* = 24.5 years) produced syllables representing four different manners of production during real-time dynamic MRI scans. We acquired an oblique-coronal slice of the velopharyngeal mechanism, which captured the length of the LVP, and manually segmented each frame. LVP shortening and muscle velocities were calculated from the acquired images.

Results: Using our method, we found that subjects demonstrated greater LVP shortening and higher maximum contraction velocities during fricative and plosive syllable production than during nasal or vowel syllable production. LVP shortening and maximum contraction velocity positively correlated with velopharyngeal port depth.

Conclusions: *In vivo* LVP function differs between manners of production, as expected, and an individual's velopharyngeal portal dimensions influence LVP function. These measures contextualized with the force-length and force-velocity muscle relationships, provide new insight into LVP function. Future studies could use this method to investigate LVP function in healthy speakers and individuals with repaired cleft palate and how function relates to velopharyngeal anatomy.

2.2 Introduction

The velopharyngeal (VP) mechanism consists of the velum, lateral pharyngeal walls, posterior pharyngeal wall, and associated musculature. Proper function of the VP mechanism is necessary for acceptable and perceptually normal speech production. During oral speech production in healthy individuals, the VP muscles, primarily the levator veli palatini (LVP), move the velum superiorly and posteriorly into contact with the posterior pharyngeal wall (82,169). This action, in conjunction with lateral wall contraction seals the VP port, completely separating the nasal and oral cavities, which is required for oral speech production. VP dysfunction (VPD) occurs when the VP mechanism is unable to close the port completely and is a common issue for individuals with repaired cleft palate. How VP anatomy affects function in healthy anatomies is unknown; furthermore, an understanding of how this structure-function relationship differs in repaired cleft palate remains limited. The LVP is the primary muscle of VP closure (20), so a method to measure *in vivo* LVP function is needed to empower investigation of the VP structure-function relationship.

The LVP is one of over 600 skeletal muscles in the body (132), all of which are characterized by two properties intrinsic to skeletal muscle and related to muscle force-producing capability: force-length and force-velocity relationships. These two fundamental relationships describe how muscle length and contraction velocity affect the muscle's force-generating potential. Maximum isometric active force is produced when a muscle is at or near optimal length, and force decreases as the muscle lengthens or shortens away from optimal length (36,51,66,84,180). For non-isometric contraction, the velocity of the muscle contraction

affects its force-generating potential. As contraction velocity increases, force decreases until a maximum velocity is reached at which no force can be generated (12,78).

If muscle force-generating potential is diminished due either to muscle length, muscle velocity, or both, two possibilities exist. Either the LVP cannot achieve the force necessary for effective closure of the VP mechanism, and thus, hypernasality and dysfunctional speech result; or if closure is possible, greater LVP muscle activation is required to achieve closure, and repeated activations cause fatigue during speech. A computational modeling study predicted that certain advantageous VP anatomies could produce nearly twice the degree of closure, as measured by closure force, as less advantageous anatomies for the same LVP activation level (88). In that study, the disadvantageous anatomies required greater amounts of LVP shortening, moving the muscle farther away from optimal fiber length, and consequently, decreasing the force-generating ability of the muscle. These results highlight the need for further investigation into the relationship between VP anatomy and LVP muscle lengths and velocities. In order to test the hypotheses posed above and quantitatively establish what constitutes healthy LVP function, a new experimental method to capture LVP muscle lengths and velocities *in vivo* is needed.

The goals of this study are to (i) develop a new methodology for determining LVP muscle shortening (length change) and muscle velocities during speech production using real-time dynamic MRI; and (ii) demonstrate our method's utility to advance understanding of *in vivo* LVP function by comparing LVP function in syllables that represent four different manners of production and relating these LVP functional measures to VP anatomy. We describe a method for calculating LVP muscle shortening and contraction velocity from oblique-coronal static and

dynamic MRI that can be utilized with any speech sample, and our method is exhibited for a sampling of English syllables. We predict that measures derived from our method will be able to distinguish oral consonants requiring high oral pressures from vowels and nasal consonants, which require lower oral pressures (4). Additionally, we expect that our LVP functional measures will correlate with VP port depth. We applied our method for calculating LVP length and muscle velocity to six adults with healthy VP anatomy producing a sampling of English syllables. Based on these results, we examined the relationship between VP anatomical parameters and LVP muscle shortening and velocity.

2.3 Methods

Participants

Six Caucasian healthy adults, consisting of 3 males and 3 females, between the ages of 21 and 29 years old (*M* = 24.5 years, *SD* = 3.3 years) with body mass index less than 27, participated in this study. All participants were native English speakers, and none reported history of musculoskeletal disorders, sleep apnea, or neurologic disorders that could affect the study's region of interest. Additionally, each participant was judged by first author to have normal resonance. No subjects had any contraindications for magnetic resonance imaging scans. Informed consent was obtained for each participant, and this study was approved by the institutional review board of the University of Virginia.

Magnetic Resonance Imaging

All participants were scanned using a Siemens Avanto 1.5 Tesla magnetic resonance (MR) scanner with head and neck coil arrays. After localizer scans, two three-dimensional (3D)

anatomic scans were performed while each participant was at rest. Each subject was instructed to breathe normally through the nose and swallow as infrequently as possible to minimize velum motion and image blurring. A high-resolution, T2-weighted turbo-spin-echo scan with the optimized SPACE (sampling perfection with application optimized contrasts using different flip angle evolution) protocol (147) was used to acquire images in both static scans (details in Table 2.1). Sagittal images acquired from the first 3D scan were used to identify an oblique-coronal plane containing the length of the LVP. Images from the second 3D scan were parallel to this oblique-coronal plane. Scan time for each static scan was slightly more than 8 minutes. Images of the VP mechanism during speech were acquired using a real-time spiral gradient echo (GRE) sequence (55). This sequence allows for simultaneous acquisition of two non-parallel slices. For most effective evaluation of velar and LVP motion during speech, a mid-sagittal slice and an oblique-coronal slice along the length of the LVP (parallel to the static oblique-coronal plane) were chosen. Images from the static oblique-coronal scan were used determine the optimal location for the dynamic oblique-coronal slice. Each dynamic slice has temporal resolution of 18.2 frames-per-second (fps) and spatial resolution of 1.2 x 1.2 mm^2 with a 156 x 156 mm^2 field-of-view and slice thickness of 8 mm. Each participant completed eight dynamic scans while producing a different English syllable for 6.6-second real-time scan. Participants were asked to produce two plosive consonant syllables (/bʌ/, /kʌ/), two fricative consonant syllables (/sʌ/, /fʌ/), two nasal consonant syllables (/mʌ/, /nʌ/), and two vowel syllables (/æ/, /i/). Participants repeated the chosen syllable three times at a self-selected comfortable pace during the dynamic scan. Duration of each vowel syllable production was no more than 0.5 seconds for any subject.

Static 3D MRI parameters	
Pulse Sequence	SPACE: T2 turbo-spin-echo, flip angle: 150
Field of View	256 x 256 x 159/119 (sag/ob-cor) mm3
Repetition Time	1000 ms
Echo time	121/122 (sag/ob-cor) ms
Echo train length	59 ms
Averages	2
Resolution	1.0 mm isotropic
Length of scan	8 min 22 s for 1 static volume

Table 2.1 Static MRI Protocol, 1.5 T

Image Analyses

Both the high-resolution static images and real-time oblique-coronal dynamic images were analyzed to determine LVP muscle lengths during speech (Figure 2.1). In the static images, in which the LVP body can be easily identified, we defined reference lines and quantified the relationship between these reference lines and the LVP path. Then, in the lower-resolution dynamic images that capture velum movement, once the reference lines were placed, we used the previously quantified relationship to determine the LVP path in each dynamic frame. All image analyses were completed in OsiriX (183). The high-resolution static oblique-coronal image corresponding to the location of the dynamic oblique-coronal slice was determined by location recorded by the scanner and manually confirmed. On the chosen static image, we placed two inferior-superior (vertical in 2D image) reference lines on each lateral edge of the VP port (Right Lateral Line, Left Lateral Line, Figure 2.1). Additionally, we placed two lateral reference lines (horizontal in 2D image) at the superior and inferior boundaries of the velum

(Superior Velum Line, Inferior Velum Line, Figure 2.1). These references lines were chosen specifically because their locations are easily identifiable in both the high-resolution static image and the lower-resolution dynamic images. All references for image analysis are detailed in Table 2.2.

The body of the LVP in the oblique-coronal image was identified similarly to previous studies (100,164,175) with the origin designated the LVP origin point (LOP). We estimated the path of the LVP as a two-segment, three-vertex line with each vertex positioned on the LVP body. The vertices were defined such that one vertex is the LOP; the middle vertex, called Velar Boundary Point (VBP), lies along the Left Lateral Line (LLL), and the final vertex, noted Mid-Velum Point (MVP), is halfway between the Right Lateral Line (RLL) and LLL. With the LVP path determined, scaling factors were defined to quantify the relationship between the LVP path vertices and the Superior and Inferior Velum Lines (SVL and IVL respectively). The mid-velum scaling factor, MV_f, is the in-plane vertical distance between MVP and SVL divided by the velar thickness. Similarly, the velar boundary scaling factor, VB_f, is the in-plane vertical distance between VBP and SVL divided by the velar thickness. These factors were determined per subject (Figure 2.1C) and led to the following relationship between LVP path vertices and reference lines:

$$MVP_x = (LLL_x + RLL_x)/2$$

$$MVP_y = SVL_y - MV_f * (SVL_y - IVL_y)$$

$$VBP_x = LLL_x$$

$$VBP_y = SVL_y + VB_f * (SVL_y - IVL_y).$$

A dynamic image acquired with the velum at rest and the selected static image were manually aligned using anatomical features and landmarks clearly distinguishable in both images, such as head outline, bottom teeth profile, and VP port location. Reference lines and LVP origin point (LOP) from the higher resolution static images were overlaid on the dynamic image (Figure 2.1D). The Left and Right Lateral port reference lines (LLL, RLL) and LVP origin point remained constant throughout each dynamic image series. The Superior and Inferior Velum lines were placed manually in each dynamic image based on current velum location. The intravelar segment of the LVP was estimated as a straight line segment between Mid-Velum Point and Velar Boundary Point, and the extravelar segment was estimated as a straight line segment from Velar Boundary Point to LVP Origin Point. The total length measurement of the LVP was the sum of the intra- and extravelar segment lengths. LVP length was calculated for each frame of every dynamic series. LVP resting length was defined as the maximum LVP length calculated across all frames in each dynamic series. For each frame, LVP shortening, in units of mm, was calculated as the difference between resting length and LVP length in the current frame, i.e. LVPrest – LVPframe. The largest shortening value calculated for each sample was defined to be the maximum shortening for the given speech sample. Normalized LVP shortening for each frame was calculated as LVP shortening divided by resting length, and maximum relative LVP shortening was determined for each speech sample. LVP lengths were plotted versus time to create a time course of LVP length throughout each speech sample (normalized example in Figure 2.2A).

Plane	Reference	Definition
oblique-coronal	Levator Origin Point (LOP)	point located at LVP origin
	Superior Velum Line (SVL)	in-plane horizontal line denoting the superior-posterior boundary of velum
	Inferior Velum Line (IVL)	in-plane horizontal line denoting the inferior-anterior boundary of velum
	Right Lateral Line (RLL)	in-plane vertical line at the right lateral boundary of the VP port
	Left Lateral Line (LLL)	in-plane vertical line at the left lateral boundary of the VP port
	Mid-Velum Point (MVP)	point identified on LVP path located in the middle of the velum (equidistant from the RLL and LLL)
	Velar Boundary Point (VBP)	point identified at the intersection of LVP path and LLL
	Measure	**Definition**
mid-sagittal	pharyngeal depth	posterior nasal spine to posterior pharyngeal wall along plane of hard palate
	sagittal angle	angle between line defined by anterior boundaries of 3rd and 4th cervical vertebrae and the line along LVP length
	velar length	length of curvilinear line from posterior nasal spine to the tip of the uvula through the middle of the velum
oblique-coronal	port depth	linear distance from the anterior, mid-sagittal point on the surface of the velum to the posterior, mid-sagittal point in the oblique-coronal plane on the surface of the posterior pharyngeal wall
	velar thickness (VT)	in-plane vertical distance between superior velum line and inferior velum line (also defined in mid-sagittal plane as distance from velar knee to velar dimple)
	ΔMV	in-plane vertical distance between MVP and SVL
	ΔVB	in-plane vertical distance between VBP and SVL

Table 2.2 Reference point and lines and measurements taken for image analysis

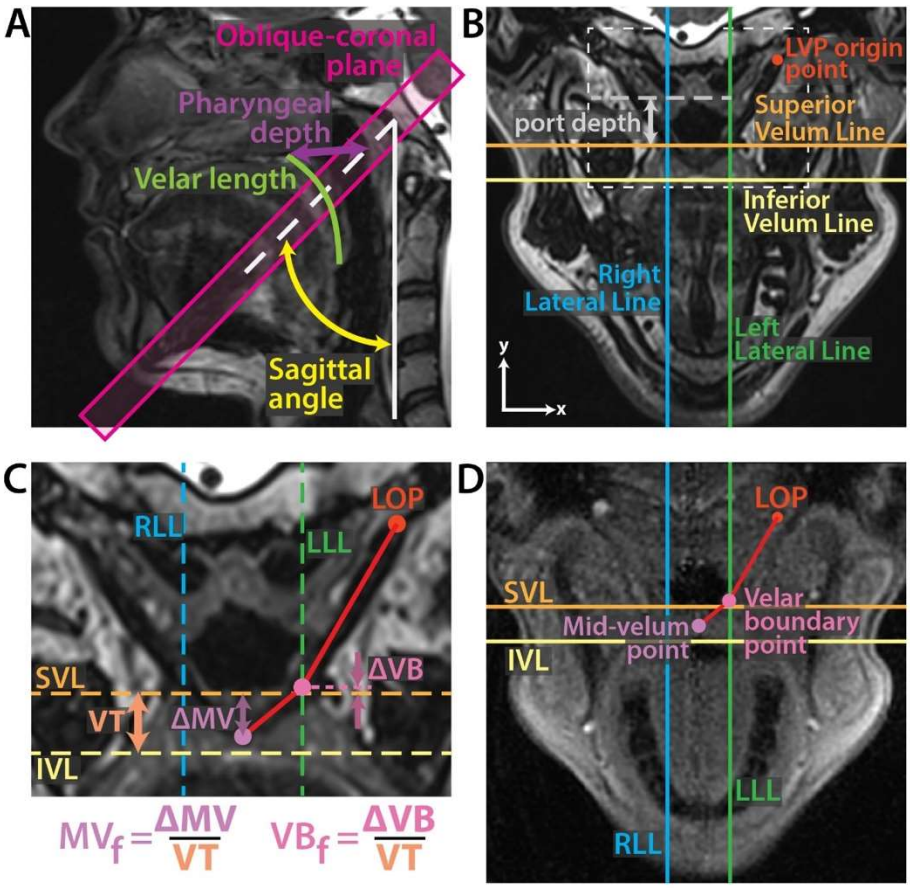

Figure 2.1 Imaging planes, reference lines, and measurements used for analysis.
A. Static, midsagittal view displays oblique-coronal imaging plane along the length of LVP; pharyngeal depth (defined as posterior nasal spine to PPW along plane of hard palate); velar length; and sagittal angle (the angle between the line defined by anterior boundaries of 3rd and 4th cervical vertebrae and line along the LVP length).
B. Static oblique-coronal view, defined in A, displays the LVP origin point (LOP) and four reference lines used to calculate LVP length, as well as velopharyngeal port depth. In the image plane, two reference lines are horizontal: superior velum line (SVL) and inferior velum line (IVL); two are vertical: right lateral line (RLL) and left lateral line (LLL). C. Static, oblique-coronal view with boundaries denoted by white dotted box in B. The two-segment path of LVP is determined such that the end vertex (mid-velum point) lies halfway between RLL and LLL; the middle vertex (velar boundary point) lies on LLL; and the end vertex is the LOP.
C. Once the path is determined, scaling factors are defined to quantify the relationship between mid-velum and velar boundary points and superior and inferior velum lines for dynamic analysis. Velar thickness (VT), ΔMV, and ΔVB are defined as the in-plane vertical distances between SVL and IVL, MVP and SVL, and VB and SVL respectively. The scaling factor MVf is ΔMV divided by VT; similarly, scaling factor VBf is ΔVB divided by VT.
D. Dynamic, oblique-coronal image with velum at rest displays reference lines and points with LVP path calculation. As the velum moves vertically in plane throughout the image series, SVL and IVL are adjusted in each frame. MVP and VBP are recalculated, and the two-segment path of the LVP is determined for that frame.

We fit a piecewise cubic spline to the LVP length versus time data in MATLAB (The Mathworks Inc, Natick, MA, USA). We then computed the derivative with respect to time of the cubic spline and evaluated the derivative at each time point in the dynamic series to determine LVP muscle velocity. Non-normalized LVP lengths were used to calculate LVP velocities in units of mm/second, and normalized LVP lengths were used to calculate normalized LVP velocities in units of muscle lengths/second (Figure 2.2). Positive velocities correspond to muscle lengthening and negative velocities to muscle shortening. Therefore, maximum contraction velocity for each speech sample was defined as the minimum calculated velocity (most negative).

Mid-sagittal dynamic images were used to confirm VP closure during analysis of oblique-coronal images. In each subject's static, oblique-coronal image, acquired with the velum was at rest, we measured VP port depth as the linear distance from the anterior, mid-sagittal point on the surface of the velum to the posterior, mid-sagittal point in the oblique-coronal plane on the surface of the posterior pharyngeal wall. In each subject's static, mid-sagittal image, acquired while the velum was at rest, we made three additional anatomical measurements: pharyngeal depth, defined as linear distance between the posterior nasal spine (PNS) and the posterior pharyngeal wall along the plane of the hard palate; velar length, defined as the curvilinear length from PNS to the tip of the uvula; and sagittal angle, the angle between the line defined by anterior boundaries of 3rd and 4th cervical vertebrae and line along the LVP length.

Statistical Analysis

LVP shortening and maximum LVP contraction velocities were tested for normality using the Shapiro-Wilk test. Assumptions of normality for LVP shortening and normalized shortening

values were met (p = .153 and p = .267 respectively) but were violated for LVP contraction velocities and relative contraction velocities (p < .001 for both). However, following a logarithmic transformation, assumptions of normality were met for both contraction velocities and relative contraction velocities (p = .443 and p = .604 respectively). Mauchly's Test of Sphericity indicated that assumptions of sphericity had not been violated for any LVP function measure: shortening: $\chi^2(5, N = 48) = 3.115$, p = .684; normalized shortening: $\chi^2(5, N = 48) = 2.298$, p = .807; contraction velocity: $\chi^2(5, N = 48) = 1.657$, p = .895; and relative contraction velocity: $\chi^2(5, N = 48) = 1.688$, p = .891.

Differences in LVP shortening and maximum LVP contraction velocities between types of sounds were analyzed using a repeated measures Analysis of Variance (rANOVA). Pairwise differences between types of sounds were compared using paired t tests with Holm-Bonferroni corrected critical values to minimize the effect of multiple comparisons and to control the familywise (Type I) error rate. The relationship between VP port depth and each LVP function measure (shortening or maximum contraction velocity) was analyzed using linear regression between each subject's VP port depth measurement and average LVP measure across all sounds. Similarly, the relationships between each of pharyngeal depth, velar length, and sagittal angle and LVP shortening and maximum contraction velocity were analyzed using linear regression.

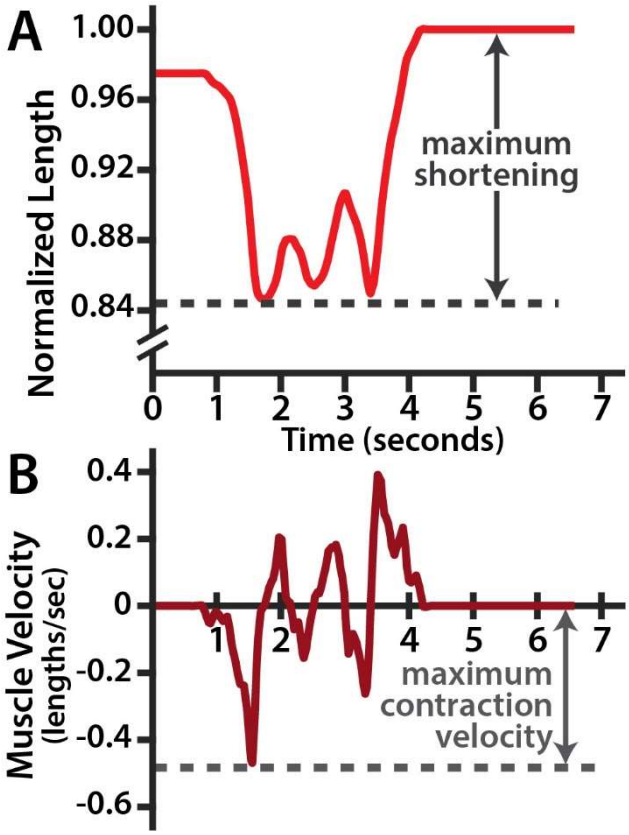

Figure 2.2 Time course of normalized LVP length and muscle velocity
Normalized LVP length is relative to resting length. Subject is producing /kʌ/ three times during the 6.6 second scan.
A. The length of the LVP shortens for the first utterance and relaxes slightly before shortening for the second and third utterances. Maximum shortening is calculated as the difference between the shortest LVP length and LVP resting length, defined per subject.
B. Muscle velocity is the time derivative of LVP length. Negative velocity indicates muscle shortening, and maximum contraction velocity is defined as the minimum calculated (most negative) muscle velocity.

2.4 Results

Across all speech samples for all subjects, LVP shortening relative to resting length varied an average of 1.7% between the three productions of the sample syllable. LVP shortening measured during vowel and nasal consonant syllables was consistently lower than shortening during plosive and fricative syllable production for all but one subject. For that subject, shortening during /kʌ/ was similar to shortening during vowel production for all three productions, and shortening was greatest during other plosive and fricative syllable production. LVP shortening relative to resting length varied significantly between manners of production, as determined by a rANOVA, $F(3, 33) = 43.86$, $p < .001$. Subjects demonstrated the greatest LVP shortening during production of fricative, $M = 17.8$, 95% Confidence Interval (CI) [14.7, 20.9], and plosive, $M = 17.5$, 95% CI [14.4, 20.6], syllables. Maximum LVP shortening values (% resting length) measured during both plosive and fricative speech samples were significantly greater ($ps < .001$) than those during nasal consonant production, $M = 10.1$, 95% CI [7.5, 12.8], or vowel production, $M = 13.9$, 95% CI [11.2, 16.6] (Figure 2.3A, Table 2.3). The LVP shortened significantly more ($p < .001$) during vowel production compared to nasal production (Table 2.3, Figure 2.3B). Additionally, maximum LVP shortening (mm) significantly differed between each manner of production, $F(3, 33) = 39.54$, $p < .001$. The magnitudes of shortening were significantly different ($ps < .001$) between all pairs, except for between plosives and fricatives (Table 2.4).

A similar trend held true for LVP maximum contraction velocities; maximum contraction velocities varied significantly across the four manners of production, $F(3, 33) = 16.00$, $p < .001$. Relative maximum contraction velocity (muscle lengths/second) was highest during fricative

syllables, *M* = 0.67, 95% CI [0.50, 0.90], followed by plosive syllables, *M* = 0.62, 95% CI [0.48, 0.81] (Figure 2.3B). Maximum contraction velocities for both fricatives and plosives were greater than contraction velocities demonstrated during vowel, *M* = 0.38, 95% CI [0.31, 0.47], or nasal consonant production, *M* = 0.34, 95% CI [0.25, 0.48] (Table 2.3). In addition, maximum contraction velocities (mm/second) varied significantly between sound types. $F(3, 33) = 16.09$, $p < .001$.

The relationship between each measurement and VP port depth was examined to provide insight into how LVP function relates to subject anatomy. Average maximum shortening (mm) across speech samples positively correlated with VP port depth, $R^2 = 0.89$, $F(1, 4) = 32.57$, $p = .005$ (Figure 2.4A). Similarly, maximum contraction velocities (mm/second) positively correlated with VP port depth, $R^2 = 0.82$, $F(1, 4) = 18.26$, $p = .005$ (Figure 2.5A). Maximum contraction velocities also positively correlated with pharyngeal depth, though to a lesser extent than with port depth, $R^2 = 0.69$, $F(1, 4) = 9.02$, $p = .040$. Neither LVP shortening nor maximum contraction velocity correlated positively or negatively with sagittal angle or velar length (Figure 2.4 and Figure 2.5). Relative maximum shortening and relative maximum contraction velocity also positively correlated with VP port depth, $R^2 = 0.86$, $F(1, 4) = 23.60$, $p = .008$ and $R^2 = 0.71$, $F(1, 4) = 9.99$, $p = .034$, respectively.

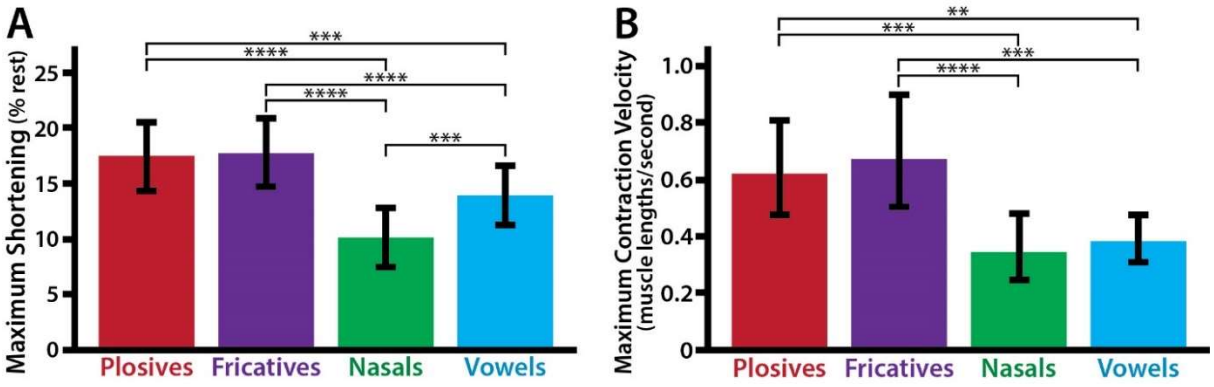

Figure 2.3 Maximum shortening and contraction velocity across sounds

A. Maximum shortening, relative to resting length, for the four types of sounds (bars indicate mean ± 95% confidence interval)

B. Maximum contraction velocity in muscle lengths per second across the four types of sounds (bars indicate ± 95% confidence interval). P values and significance were determined using paired t tests with Holm-Bonferroni corrected critical values. **p<0.01; ***p<0.001; ****p<0.0001

	Normalized Shortening (% Rest)				Shortening (mm)			
	Mean	Standard Deviation	Lower 95% CI	Upper 95% CI	Mean	Standard Deviation	Lower 95% CI	Upper 95% CI
Plosives	17.5	4.9	14.4	20.6	8.4	2.7	6.7	10.1
Fricatives	17.8	4.8	14.8	20.9	8.5	2.7	6.8	10.3
Nasals	10.1	4.2	7.5	12.8	4.8	2.2	3.5	6.2
Vowels	13.9	4.2	11.2	16.6	6.7	2.3	5.2	8.1

	Relative Contraction Velocity (lengths/sec)					Contraction Velocity (mm/sec)				
	Raw Mean#	Standard Deviation#	Trans-formed Mean^	Lower 95% CI^	Upper 95% CI^	Raw Mean#	Standard Deviation#	Trans-formed Mean^	Lower 95% CI^	Upper 95% CI^
Plosives	0.67	0.31	0.62	0.48	0.81	32.2	15.1	29.3	22.1	38.9
Fricatives	0.74	0.35	0.67	0.50	0.90	35.4	18.0	31.8	23.6	43.0
Nasals	0.39	0.21	0.34	0.25	0.48	18.5	10.6	16.2	11.6	22.6
Vowels	0.40	0.15	0.38	0.31	0.47	19.3	8.0	18.0	14.1	23.0

- Raw Mean and Standard Deviation calculated from un-transformed data

^ - Due to violation of normality assumption, means and confidence intervals were calculated from data following logarithmic transformation and then back-transformed to determine Transformed Mean and Confidence Intervals

Table 2.3 Means, standard deviations, and confidence intervals for LVP shortening and contraction velocity

		Normalized Shortening (% Rest) p value	Shortening (mm) p value	Relative Contraction Velocity (lengths/sec) p value	Contraction Velocity (mm/sec) p value
Plosives	**Fricatives**	0.704	0.656	0.477	0.469
Plosives	**Nasals**	<0.001	<0.001	<0.001	<0.001
Plosives	**Vowels**	<0.001	<0.001	0.002	0.002
Fricatives	**Nasals**	<0.001	<0.001	<0.001	<0.001
Fricatives	**Vowels**	<0.001	<0.001	<0.001	<0.001
Nasals	**Vowels**	<0.001	<0.001	0.471	0.469

Table 2.4 P values for all pairwise comparisons

P values calculated using paired t test with significance determined using Holm-Bonferroni corrected critical values.

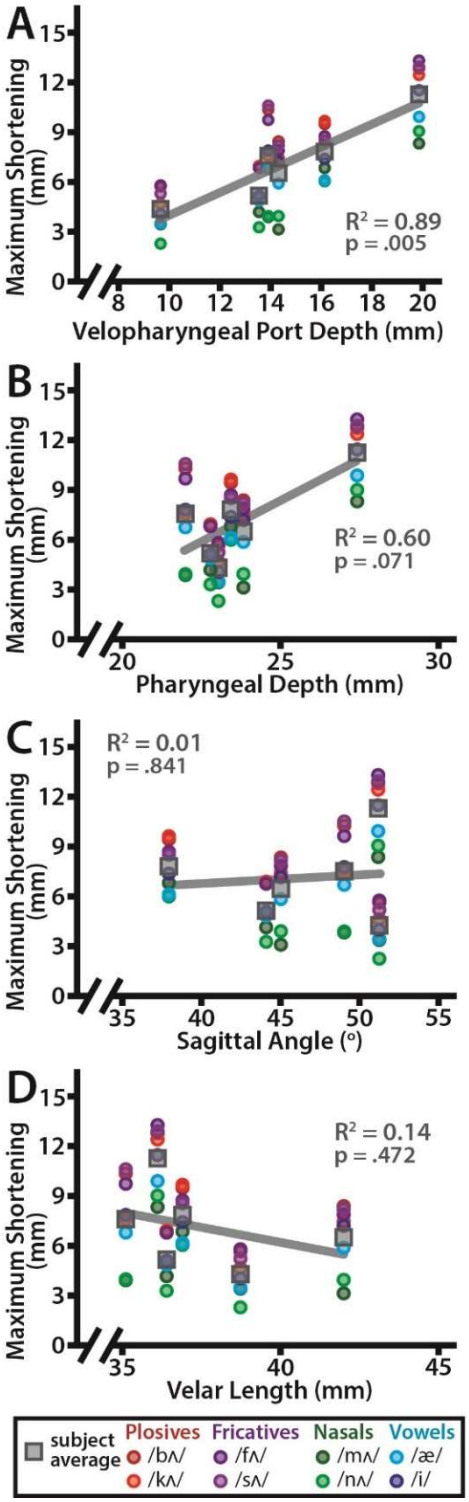

Figure 2.4 Maximum shortening correlations with anatomical measures
Maximum shortening, measured in mm, positively correlates with velopharyngeal port depth (A) and moderately positively correlates with pharyngeal depth (B). Maximum shortening does not significantly correlate with sagittal angle (C) or velar length (D).

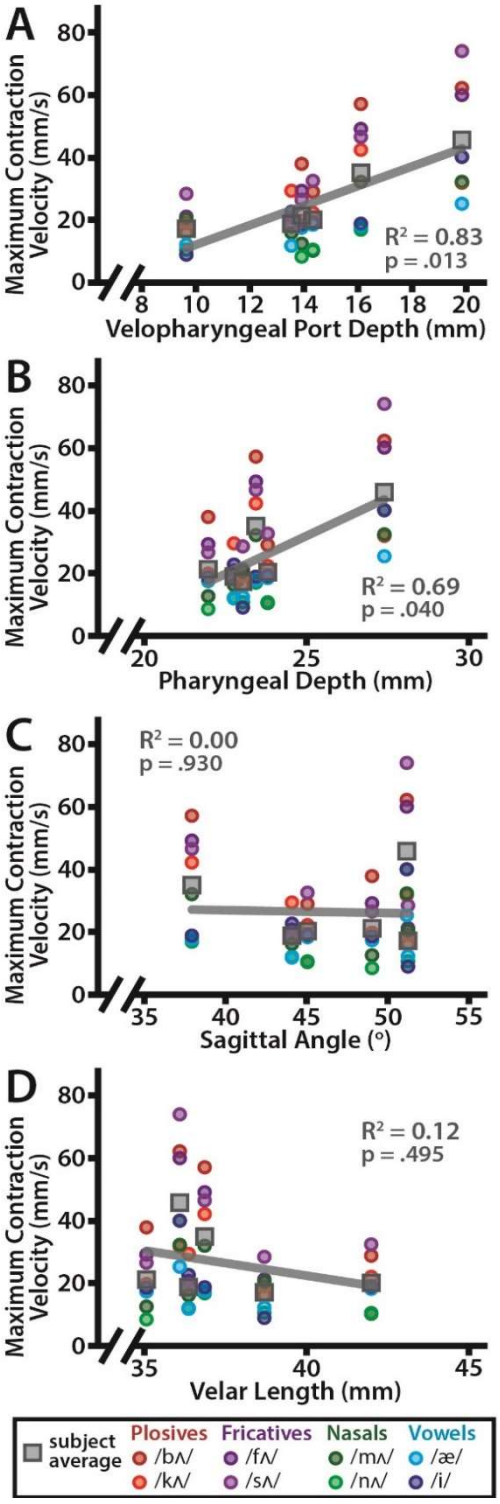

Figure 2.5 Maximum contraction velocity correlations with anatomical measures
Similar to maximum shortening, maximum contraction velocity, measured in mm/second, positively correlates with velopharyngeal port depth (A). Maximum contraction velocity also significantly positively correlates with pharyngeal depth (B) but does not significantly correlate with sagittal angle (C) or velar length (D).

2.5 Discussion

The purpose of this study was to develop a new method for evaluating LVP muscle behavior during real-time speech using dynamic MRI and demonstrate this method by comparing LVP function between sounds and probing the relationship between VP anatomy and *in vivo* LVP function. Experimental investigation into how VP anatomical variability affects LVP function was impossible without a method to measure LVP function *in vivo*. Our described method combines static and real-time dynamic MRI, both acquired in the plane of the LVP, to measure LVP length and velocities during speech production. Our results demonstrate that our method is capable of determining the variation in LVP function between different manners of production, as well as providing LVP muscle shortening and velocity measures that can be used to investigate the VP structure-function relationship.

Our dynamic LVP shortening results are comparable to LVP shortening values reported in previous studies. Average LVP shortening was reported to be 19% during sustained fricative production (54), similar to the our average shortening of 17.8% during dynamic fricative syllable production (*SD* = 4.8). Ettema et al. reported greatest amounts of LVP shortening during fricative production, followed by vowel, and lastly nasal production. The present study found the same progressive decrease in LVP shortening, and the real-time nature of our method enabled us to demonstrate that LVP contraction velocities are greater during plosive and fricative syllable production than during nasal or vowel production. Our shortening results also compare favorably to length changes reported during real-time production of the nonsense word “ansa”. Perry et al. reported average LVP shortening values across ten subjects, ranging from 5% during /n/ to 16% during the final /a/ production (175). In our six subjects, LVP

shortening ranged from 10.1% (*SD* = 4.2) during nasal production to 17.8 % (*SD* = 4.8) during fricative production.

Relating LVP shortening and velocity measurements to VP port depth provided new insights into the relationship between VP anatomy and *in vivo* LVP function. We found that both LVP shortening and maximum contraction velocities positively correlate with VP port depth. This suggests that individuals with a shallower VP port require less muscle shortening and shortening at a slower rate than individuals with a deeper VP port do. Additionally, maximum contraction velocities positively correlated with pharyngeal depth, whereas LVP lengths and velocities did not correlate with either sagittal angle or velar length (*ps* > .05, Figure 2.4 and Figure 2.5). VP port depth and pharyngeal depth are both indicative of the physical distance the LVP must contract to achieve VP closure. These correlative relationships imply that a subject's VP port dimensions affect LVP muscle function and provide evidence to support the hypothesis that a range of ratios between VP portal and LVP muscle dimensions exists, outside of which healthy VP closure is unachievable (88,173,187).

Given the context of the force-length relationship, our dynamic MRI-based method provides new and valuable insights into LVP muscle mechanics during speech. Our method facilitates novel functional insights during speech that are similar to insights gained using ultrasound imaging to investigate lower limb muscle mechanics during walking and other locomotion (28,41,121). These *in vivo* imaging methods are required to evaluate typical muscle behavior and its effect on function in healthy and pathological populations. During speech production, when the LVP contracts and shortens to close the VP port the muscle moves away from optimal length, reducing force-generating capacity. When less shortening occurs, due to

either the type of sound or the speaker's VP anatomy, the LVP is operating near the peak of the force-length curve. The reduction in LVP force-generating capability is minimal for our observed range of shortening (5.6% to 26.3% across all subjects, Figure 2.6A) if we assume that optimal fiber length occurs at resting length, similar to previous studies (e.g. (87)). However, the ascending limb of the force-length curve becomes very steep as fibers continue to shorten from optimal fiber length. As the LVP muscle shortens more substantially, force-generating potential sharply decreases. Further studies are needed to determine how much the LVP shortens in individuals with repaired cleft palate and if that level of shortening results in a meaningful reduction in muscle force generation.

Our method provides measurements of LVP contraction velocities during speech, which are functionally meaningful due to the force-velocity relationship of muscle. As muscle velocity increases, the force produced decreases until a maximum velocity (v_{max}) is achieved at which no force can be produced. V_{max} of the LVP is unknown, but using the fiber type distribution (Moon, et al., 1998) and known v_{max} for each fiber type (Larsson & Moss, 1993), we estimate LVP v_{max} as 1.5 lengths/second. In our limited speech sample, the LVP operated at contraction velocities between 0.39 and 0.74 muscle lengths/second. Contraction velocities of this magnitude lead to substantial reductions in LVP force-generating potential (Figure 2.6B). For effective production of sounds with higher contraction velocities, the LVP would need greater activation to achieve the force required, leading to possible muscle fatigability, especially in individuals with undersized LVP muscles. There is a tradeoff, however, between muscle force generation and power production. Muscle power, i.e. the product of force and contraction velocity, is maximized near $0.3v_{max}$. In our group of healthy adults, the LVP is operating close to $0.3v_{max}$ for

many of the sounds included, leading to near maximal power output. The contraction velocities observed in healthy speakers yield enough force to achieve sufficient closure for plosive and fricative sounds while remaining near peak power. However, LVP contraction velocities and their effects on force generation, power production, and VP function in individuals with repaired cleft palate are unknown and warrant investigation.

An understanding of how differences between repaired cleft and healthy anatomies affect VP function remains limited. More severe cases of VPD tend to have a shorter effective velar length, defined as the linear distance from posterior nasal spine to center of LVP muscle (81). Additionally, hypernasality persisted when total velar length did not increase after secondary palate repair (44,63). Other studies have proposed that there exist VP dimensional extrema, e.g. minimum ratio of velar length to pharyngeal depth (187) or range of LVP lengths and angles of origin (173), outside of which healthy speech is unachievable. LVP muscles from children with cleft palate consist of more connective tissue and less contractile tissue within the muscle, a higher proportion of type II, fast-twitch fibers, and noted hypoplasia compared to muscles from noncleft children (120,124). By adulthood, individuals with repaired cleft palate demonstrate shorter and thinner LVP muscles, reduced LVP volume, more acute LVP angles of origin, and greater pharyngeal depths than healthy adults (68,103,167). These inherent morphological and structural differences between healthy and repaired anatomies lead to the hypothesis that LVP shortening magnitudes and velocities differ between healthy speakers and individuals with repaired cleft palate. Future studies can utilize this method to investigate this hypothesis and the effects of altered anatomy on LVP function.

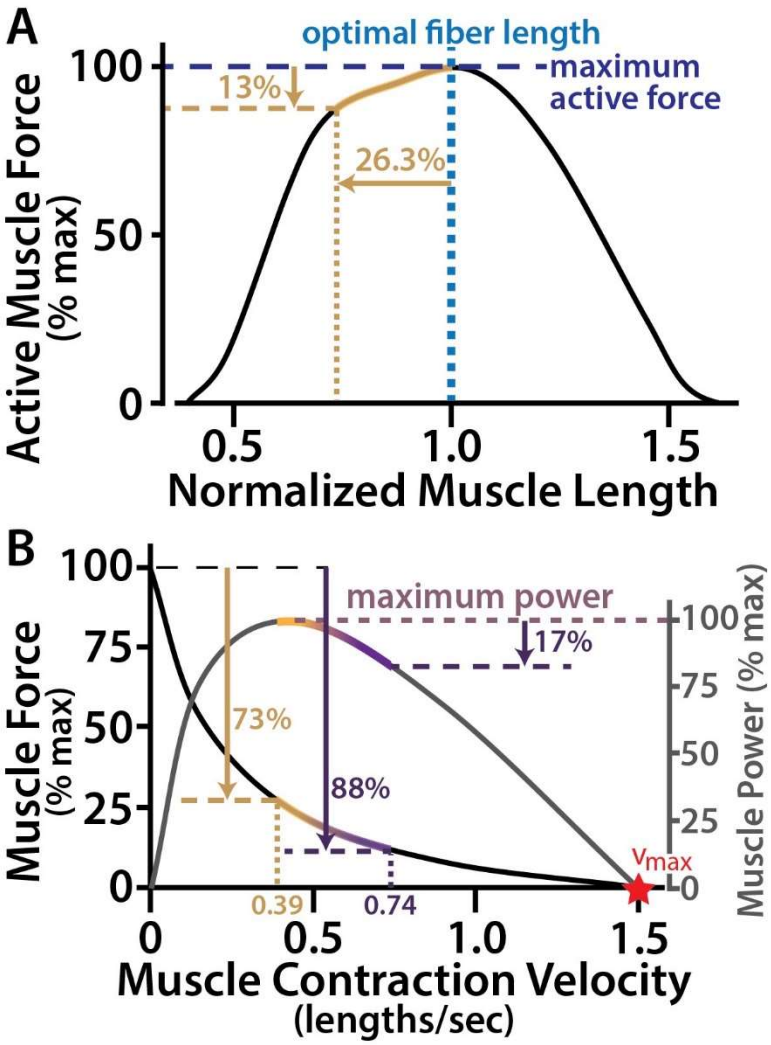

Figure 2.6 Fundamental relationships of skeletal muscle.
A. Force-length relationship. Active muscle force is maximized at optimal fiber length. Active force-generating potential decreases as the muscle shortens or lengthens from optimal fiber length. At 26.3% shortening from optimal fiber length (the maximum demonstrated in our subjects), LVP active force-generating capability is approximately 13% less than maximum active force.
B. Force-velocity-power relationship. A muscle produces maximum muscle force when muscle contraction velocity is zero. As a muscle shortens more quickly, it can produce less force. A muscle can produce no force when contraction velocity reaches v_{max}. Muscle power, defined as force*velocity, is maximized when contraction velocity is ~$0.3v_{max}$. We estimated LVP v_{max} from levator fiber type distribution and muscle fiber type v_{max}s (119,146). For the demonstrated range of LVP contraction velocities (0.39 to 0.74 muscle lengths/second), muscle force is decreased between 73% and 88% from maximum. However, at these contraction velocities, the LVP is producing near maximum power.

A critical limitation of this study is the dynamic imaging frame rate of 18.2 fps. Velar elevation can occur in or under 100 ms (104), making the minimum frame rate for effective imaging of the VP mechanism at least 10 fps (150,175,207). Our frame rate of 18.2 fps is well above that minimum, but there is the possibility that our images missed the exact instant of maximum LVP shortening. This would result in possible random underestimation of true LVP shortening values and possible addition of noise to our measurements. Despite this possibility, we were able to capture differences between sounds representing different manners of production greater than the potential noise. As stated above, our LVP shortening results compare favorably with shortening values determined from dynamic scans at 30 fps (175), giving us confidence that our method is able to capture LVP behavior trends. Additionally, our reported contraction velocity values are average velocities over the 55 ms between frames, rather than instantaneous velocities, so our reported values could possibly underestimate true maximum LVP contraction velocities. Future studies would benefit from a higher frame rate to minimize the time over which the velocity measurement is averaged, moving closer to a true instantaneous velocity measurement. A higher frame rate would be especially important when examining specific phonemes in various contexts, such as differentiating LVP behavior in a connected speech sample.

There are other limitations of this study that should be mentioned. First, the oblique-coronal plane containing the length of the LVP must be chosen appropriately during scanning; otherwise, it is impossible to make accurate LVP muscle length measurements. In healthy anatomies, these planes can be found in a straightforward manner using anatomical landmarks.

However, it is unknown whether a plane containing the entirety of the LVP exists in individuals with repaired cleft palate or how systematically it can be determined during scanning.

Second, the LVP is estimated as the union of two line segments, a simplification of the LVP path in healthy individuals and possibly an oversimplification in pathological populations. However, our measurements of healthy LVP shortening were comparable with previously reported length measurements. Manual image registration and segmentation requires a substantial time commitment for data analysis; future work is necessary to automate these procedures. Therefore, we sought a balance between anatomic accuracy and time burden for analysis. LVP geometry has been simplified to reduce computation time in previous computational studies (22,87,203), including one with a two-segment representation of the LVP (88), and these studies nevertheless provided meaningful insights into the relationship between VP anatomy and function. The other VP muscles could affect the VP structure-function relationship; in particular, the musculus uvulae can act agonistically to the LVP as a velar extensor and reduce the burden of the LVP during VP closure (86,108). Without the musculus uvulae, we found positive correlative relationships between LVP function and VP portal dimensions, but inclusion of the musculus uvulae in our analysis could help explain the variability in our correlations and should be considered in future studies.

Finally, the speech sample in our protocol included only four manners of production and a mix of voiced and voiceless consonants. As with all consonant-vowel productions, there is a coarticulatory effect (21), and the results of our consonant-vowel samples could vary with inclusion of different vowels. However, the purpose of our study was to introduce a new method capable of measuring *in vivo* LVP function, and our results support hypotheses that LVP

function differs significantly between manners of production and provided insight into how VP anatomy affects LVP function. Future studies should consider inclusion of multiple vowels in consonant-vowel samples to examine differences in production. Additionally, our study reported shortening and contraction velocities across a speech sample and did not distinguish between phonemes within the syllables. Future studies should collect audio recordings during image acquisition that can be further analyzed, e.g. spectrographic analysis, to determine phoneme-specific LVP lengths and velocities.

This study introduces a method for measuring *in vivo* LVP function, which promotes an increased understanding of the relationship between VP anatomy and LVP function. Our method can be applied to a variety of real-time speech samples, from isolated syllable utterances to full sentence production, and our results augment the limited existing literature reporting LVP shortening during speech. We also presented, to our knowledge, the first evaluation of LVP muscle shortening velocity during speech and laid the groundwork for experimental investigation of VP structure-function relationship. Results from our limited samples and sample population suggest that certain VP anatomical dimensions strongly influence *in vivo* LVP function, and consequently, achievable force generation and overall VP function. Future studies should explore LVP behavior and its relationship with VP anatomy with a more comprehensive speech sample in both healthy speakers and individuals with repaired cleft palate. The method presented here could be used to elucidate this relationship, as well as compare LVP function between healthy and clinical populations. An increased understanding of the VP structure-function relationship will lead to increased prevention of VPD and more effective treatments for individuals with dysfunctional speech disorders.

Chapter 3

The Effect of Anatomical Variability on Velopharyngeal Closure in Children with 22q11.2 Deletion Syndrome

Acknowledgements: Lakshmi Kollara, Jamie L. Perry, Silvia S. Blemker

"It matters not what someone is born, but what they grow to be."
- Albus Dumbledore, *Harry Potter and the Goblet of Fire* (author: J.K. Rowling)

3.1 Abstract

Objective: The purpose of this study is to establish a computational modeling framework capable of distinguishing between healthy and 22q11.2 DS anatomies based solely on anatomic dimensions. We also sought to identify which anatomical features in 22q11.2 DS anatomies most influence velopharyngeal (VP) closure.

Methods: We created computational models for 13 children with 22q11.2 DS and 26 healthy control children, which included representations of the levator veli palatini (LVP), velum, and posterior pharyngeal wall. We activated the LVP to simulate VP closure and calculated LVP shortening, minimum LVP activation to touch closure, and maximum closure force. In our 22q11.2 DS models, we substituted the healthy control value for each input parameter to determine the effect on closure.

Results: Our model predictions of LVP shortening, minimum LVP activation, and maximum closure force were significantly different ($p = 0.0025$, $p = 0.0170$, $p < 0.0001$ respectively) between healthy and 22q11.2 DS anatomies. Substitution of healthy control LVP cross-sectional area values increased maximum closure force in every 22q11.2 DS anatomy. However, substitution of most input parameters had a variable effect across the 22q11.2 DS anatomies.

Conclusions: The anatomical differences in 22q11.2 DS lead to model-predicted functional differences. Overall, increases in LVP cross-sectional area, or LVP strength, could be beneficial to children with 22q11.2 DS with (or without) VP dysfunction. However, patient anatomy should be considered when devising VP dysfunction treatments for children with 22q11.2 DS.

3.2 Introduction

22q11.2 Deletion Syndrome, also known as velocardiofacial syndrome, is a microdeletion syndrome caused by gene deletion on chromosome 22. Over 180 different physical and behavioral features have been associated with this genetic syndrome, including clinical phenotypes affecting nearly every organ system (182,194). 75% of patients with 22q11.2 DS demonstrate some velopharyngeal (VP) structural abnormalities (31,95), and 22q11.2 DS is the most common congenital cause of velopharyngeal dysfunction (VPD) (95,194). VPD in 22q11.2 DS individuals has a complex and multi-faceted etiology and can occur with or without occurrence of overt or submucous cleft palate (95). VPD in 22q11.2 DS is treated with a variety of surgical procedures, including Furlow Z-plasty (16,43,141), intravelar veloplasty (27,139), pharyngeal flap (17,184,208,222,227), Honig velopharyngoplasty (201,218), and sphincter pharyngoplasty (17,129,141,221,222,227). Success rates for VPD treatment in 22q11.2 DS range from nearly all failures to equivalent with non-syndromic VPD depending on the treatment technique and the criteria for success (200). This treatment success rate discrepancy could be due to the many contributory causes of VPD in patients with 22q11.2 DS, including morphological variations of VP structures, and the considerable difficulty in distinguishing structural causes of VPD from other, non-anatomical causes.

There are inconsistent findings about how VP anatomy in patients with 22q11.2 DS differs from healthy individuals, especially concerning velar dimensions. For example, the velum has been shown to be shorter and thinner in 22q11.2 DS when compared to healthy controls (226), shorter than healthy with no report of thickness (56), thinner but not shorter (97), and neither shorter nor thinner (185). Several studies have demonstrated greater pharyngeal depth

in individuals with 22q11.2 DS (56,77,97,215), while others found no significant differences in pharyngeal depth measures (45,185). However, there is general agreement that the levator veli palatini (LVP) muscles differs significantly from healthy in several measures: LVP length (56,97), thickness (56,97,158), origin-to-origin distance (56,97), and angle of origin (56,97). VP dysmorphology in 22q11.2 DS has a negative effect on speech outcomes (18,95,226), but how individual anatomical measures affect VP function in 22q11.2 DS is unknown.

Computational modeling is a powerful tool that can be used to increase our understanding of VP mechanics. Models can integrate the wealth of literature about VP anatomy and function with data from magnetic resonance imaging (MRI) and knowledge of physical relationships to investigate cause-and-effect relationships that are unfeasible, time-consuming, or impossible with experimental methods or clinical trials. Previous models of the VP mechanism have demonstrated this utility by simulating VP closure and evaluating velar configurations during VP closure (22), determining how LVP overlap alters closure (87), quantifying the contributions of the musculus uvulae to closure (86), investigating the effects of LVP angle of origin and palatopharyngeus on VP closure (203), and probing the effect of anatomical variability on closure in healthy adult males (88). However, no modeling study to date has examined the effect of pathological anatomies on VP closure and which altered anatomical features most affect VP function.

The goals of this work were to investigate how differences in 22q11.2 DS anatomies affect VP function. Specifically, this study aimed to i) test the hypothesis that the modeling framework can distinguish between anatomies from healthy children and those with 22q11.2 DS and ii) identify which anatomical features in 22q11.2 DS anatomies most influence VP closure. We

adapted an existing computational modeling framework (88) to represent anatomies from children with 22q11.2 DS and age-matched healthy controls. Our model predicted differences between 22q11.2 DS and healthy control anatomies and that comparable changes in different anatomical features in isolation affect VP closure to varying degrees.

3.3 Methods

Participants

In accordance with local institutional review boards, a total of 39 participants were included in the study. The 22q11.2 DS group consisted of thirteen children (four males, nine females) diagnosed with 22q11.2 deletion and confirmed with fluorescence *in situ* hybridization assay. The mean age for this group was 8.5 years (SD = 2.6 years). All but one of the participants were self-reported to be of European descent for three generations (white) with one half-Hispanic. The remaining participant is half-white, half-African American. Four had normal resonance, six had mild hypernasality, one had moderate hypernasality, and two had severe hypernasality, as judged by two trained speech-language pathologists. Participants were excluded if there was evidence of overt cleft palate or history of cleft palate surgery that could affect regions relevant to this study. None of the participants with 22q11.2 DS had any other genetic disorders and were at least six months post-adenoidectomy or tonsillectomy.

The group of healthy controls consisted of 26 children (11 males, 15 females) with normal velopharyngeal anatomy and judged by two trained speech-language pathologists to have normal resonance. All control participants were native English speakers. The control group was age- and sex-matched to the 22q11.2 DS group to control for the effects of growth and sex.

The mean age for this group was 7.7 years (SD = 2.6 years). Additionally, all participants in the control group were self-reported to be of European descent for three generations (white), except for one healthy control of African-American descent, to control for the effect of race on velar length and thickness (101).

Magnetic Resonance Imaging

We utilized a child-friendly MRI protocol to allow for successful image acquisition without the use of sedation (99,100,170). For participants with 22q11.2 DS, additional modifications were enacted to ensure data collection (97,98). Images were acquired with each participant at rest and breathing nasally in a supine position to minimize motion in our region of interest. Participant image data were collected across four MRI sites using sequences with comparable parameters, all of which have been described previously (100–102,170,175). At MRI site one, we used a 3D turbo-spin-echo (TSE) sequence called Sampling Perfection with Application optimized Contrasts using different flip angle Evolution (SPACE) on a Siemens 3 Tesla Trio system (Erlangen, Germany) (147). MRI site two also used the SPACE sequence with similar parameters to site one on a Siemens 3 Telsa Skyra system (Erlangen, Germany). The final MRI site used a T2-fluid attenuation inversion recovery (FLAIR) sequence on a General Electric 3 Tesla scanner. Five healthy control participants were imaged at the MRI site four using a TSE sequence on a 1.5 Tesla Philips Gyroscan system.

Measurements from MRI

In each participant's MRI data, we completed a series of nine measurements that have been described previously and used routinely in MRI studies of the VP mechanism in healthy

individuals (54,60,101,155,166,169,171,175,188,209), those with repaired cleft palate (68,103,167), and individuals with 22q11.2 DS (56,97,102,158). Measures in the oblique-coronal plane, defined to lie along the length of the LVP, and mid-sagittal plane included dimensions of the LVP, velum, and VP port (Table 3.1). In addition, the cross-sectional area (CSA) of the LVP was measured at five locations along the LVP's length: mid-sagittal, each origin, and at the velar boundary on each side (Figure 3.1). These five measurements were averaged to calculate the LVP CSA measurement. For healthy controls, all measurements were completed five times in OsiriX software (183). For participants with 22q, measurements were completed in Amira 6 Visualization Volume Modeling software (Visage Imaging GmbH, Berlin, Germany).

	Measurement	**Description**
Mid-sagittal	Effective Velar Length	linear distance from posterior nasal spine to velar knee
	Velar Thickness	distance from velar knee to velar dimple
	Velum-LVP Angle	angle between line connecting PNS to center of mid-sagittal LVP and line defining oblique-coronal plane
	LVP Cross-sectional Area	two-dimensional (2D) area of LVP muscle in plane
Oblique-coronal	Origin-to-origin	distance between right and left points of origin of LVP muscle
	Extravelar LVP length	length of LVP muscle between origin and point of LVP insertion into the body of the velum
	Velar Insertion Distance	distance between points of LVP insertion into the body of the velum on right and left sides
	VP port depth	mid-sagittal anterior-posterior distance of VP port
	VP port width	in-plane width of the VP port
(LVP = levator veli palatini, VP = velopharyngeal)		

Table 3.1 Measurements from static MRI data

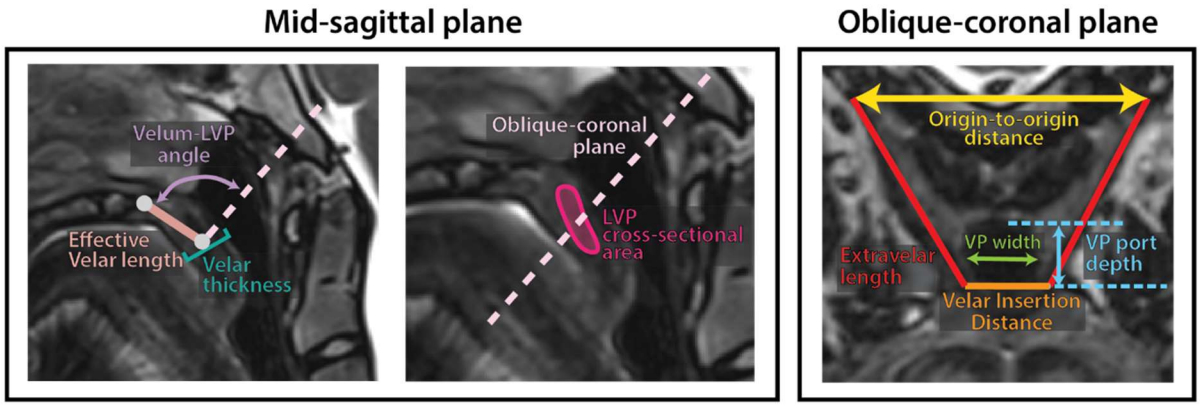

Figure 3.1 Model Inputs
Measures taken in the mid-sagittal and oblique-coronal planes used as model inputs (also see Table 3.1). Additional LVP cross-sectional area measurements were made at the velar boundary and origin of each LVP side.

Modeling Framework

Measurements from MRI were used to create line segment representations of the velum, LVP, and posterior pharyngeal wall in three-dimensional (3D) space, as described previously (88). Representation of the LVP muscle included active contraction along the muscle's length, which incorporates the force-length relationship of muscle (36,51,66,84,180). Maximum force occurs when the muscle is at optimal length, i.e. LVP stretch = $\lambda_{LVP} = 1$, and force decreases as the muscle lengthens or shortens, i.e. $\lambda_{LVP} > 1$ or $\lambda_{LVP} < 1$ (Figure 3.2). As in previous studies (87,88), we assume LVP optimal length occurs at resting length. The line of action of the LVP muscle runs along its length, so we assumed that active muscle force is proportional to LVP CSA. Muscle peak isometric stress (σ_{max}) was chosen to be 0.03 MPa after parametrization determined that 0.03 MPa best reproduced experimental closure force data (114) for healthy adult male anatomies (88). Therefore, LVP muscle force was determined as:

$$F_{LVP} = \sigma_{max} * CSA * P_{FL}(\lambda_{LVP}) * act_{LVP}, \qquad \textbf{(Equation 3.1)}$$

where = σ_{max} is peak isometric stress, CSA is LVP cross-sectional area, $P_{FL}(\lambda_{LVP})$ is percentage of maximum force possible based on LVP stretch (λ_{LVP}), as determined by the force-length relationship, and act_{LVP} is LVP muscle activation, ranging from 0% (rest) to 100% (full activation).

The velum was modeled as a simple spring with resting length equal to measured effective velum length. The Young's modulus was 1 kPa (23,88), and velum CSA was defined to be the product of velum thickness (VT) and velar insertion distance (VID). The velum spring constant is defined as the product of Young's modulus and velum CSA, i.e.

$$k_{velum} = E_{velum} * VT * VID. \quad \textbf{(Equation 3.2)}$$

Velum stretch (λ_{velum}) is defined as the ratio of stretched effective velum length to resting effective velum length. Velum force is calculated as:

$$F_{velum} = k_{velum} * (\lambda_{velum} - 1). \quad \textbf{(Equation 3.3)}$$

The posterior pharyngeal wall (PPW) was represented as a rigid body with width equal to VP port width. Geometric configurations of the velum, LVP, and PPW were determined for rest and LVP contraction with closure force calculated based on the geometry at VP closure and static force balance. An inferior force equivalent to the superior component of velum force was included to keep the LVP in the oblique-coronal plane (Figure 3.3).

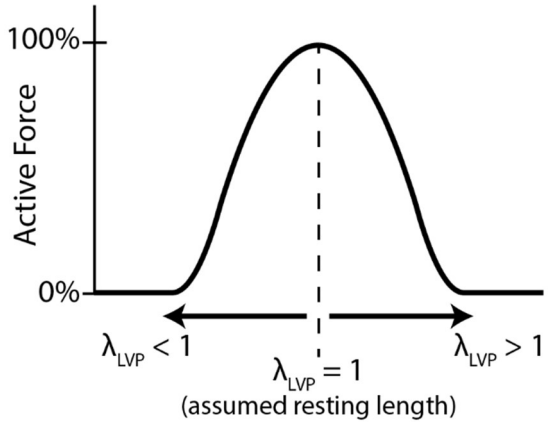

Figure 3.2 Force-length curve of skeletal muscle
The force-length relationship of skeletal muscle was used to determine active muscle tension based on amount of LVP shortening.

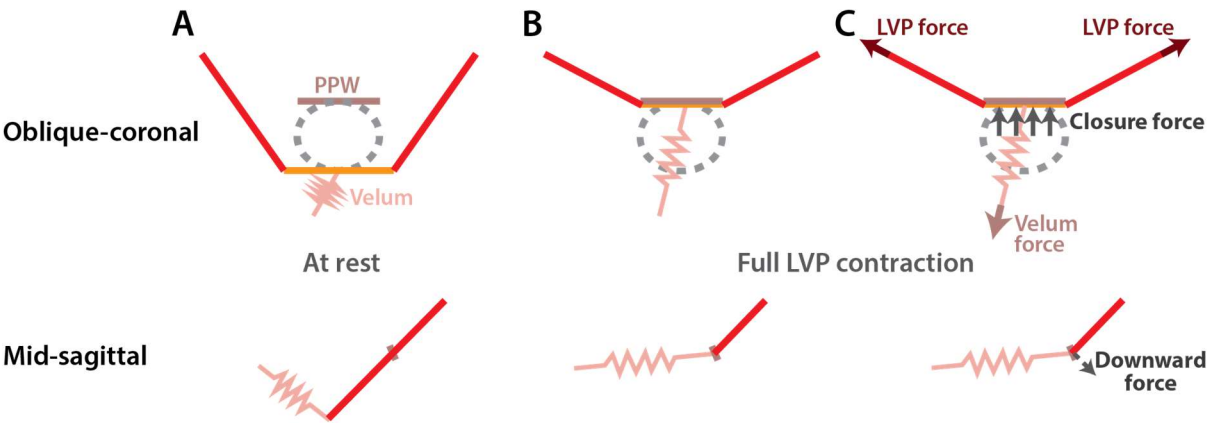

Figure 3.3 Model configuration in the oblique-coronal (top) and mid-sagittal planes
(A) at rest, (B) during VP closure, and (C) with forces designated used to determine model outputs

Simulations

Simulations of VP function were driven by activation of the LVP, ranging from 0% to 100%, which was a simulation input variable. LVP activation caused the LVP to contract and the velum to move posteriorly and superiorly. Primary simulation outputs were maximum LVP shortening, measured as resting LVP length – shortest LVP length, i.e. $\lambda_{LVPrest} - \lambda_{LVPmin}$; LVP muscle force required to attain closure; minimum LVP activation required to attain initial contact the posterior pharyngeal wall; and maximum VP closure force, measured as the magnitude of the total force exerted on the posterior pharyngeal wall during closure. We assume that lower minimum LVP activation, higher closure force, and less LVP shortening is indicative of better VP function.

We completed two sets of model simulations. First, for each anatomy, we created a model for each set of measurements (5 per healthy control and 1 per child with 22q11.2 DS). We simulated closure with each model to determine if our modeling framework can distinguish between healthy and 22q11.2 DS anatomies. Output values from the 22q11.2 DS anatomy model simulations were used as the baseline for the second set of simulations. In the second set, for each 22q11.2 DS anatomy, we perturbed input parameters in isolation to determine how each parameter affects VP closure within the physiologic range for our healthy child subjects. For each age and gender in our healthy control cohort, we calculated the average value for each input parameter to serve as the matched healthy control value. Then, for each 22q11.2 DS anatomy, we substituted this healthy control value for one parameter while holding all input parameters at their measured value. We repeated this for each model input and compared simulation outputs to the baseline output values.

Analysis

In first set of simulations, for each model output, we grouped the healthy anatomy values separately from the 22q11.2DS to establish two groups. We used an F test to determine if the variances between the two groups were equal before performing a two-tailed Student's t test to compare differences between the healthy control and 22q11.2 DS groups. Because each healthy control anatomy was represented by five models, we used the average output value across the five models for further analysis. Additionally, for both the healthy control and 22q11.2 DS anatomy groups, to determine the predictive power of each input parameter on model outputs, the relationship between each input parameter and each model output was analyzed using linear regression.

We also performed a cluster analysis that utilizes multi-dimensional data for each subject's anatomy in MATLAB (The Mathworks Inc., Natick, MA, USA). Each anatomy is represented by a data point in n-dimensional space, where each of n dimensions represents a different variable included in the cluster analysis. In our first cluster analysis, we included all MRI measures that served as inputs to the model (9 in total). Each anatomy is a point in 9-dimensional space, with x_1 = effective velar length measure for that anatomy, x_2 = velum-LVP angle for that anatomy, and similarly for $x_3 – x_9$. The distance between each pair of anatomies is determined using Euclidean distance. To start, each anatomy is its own cluster, and two clusters are combined using Ward's method, which minimizes the within-cluster variance that results from combining the two clusters. This process continues until all anatomies are contained in one cluster. Our second cluster analysis was focused on output metrics, and we included maximum closure force, minimum LVP activation, LVP shortening, and resting LVP length as

cluster variables. Before inputting variables into the cluster analysis, we standardized the range of each variable across all anatomies to give each variable equal weighting in the analysis.

For the second set of simulations, we calculated the percent change in parameter value relative to the measured value for each input parameter and each 22q11.2 DS anatomy. For each input parameter, we calculated the change in output metric (compared to baseline) when the healthy control average value was substituted for the measured input parameter. We calculated both the raw change in output metric, i.e. $output_{substituted} - output_{baseline}$, and the relative change for each output metric, i.e. $(output_{substituted} - output_{baseline})/output_{baseline}$. Lastly, the relationship between percent change in each input parameter and raw change in output metric was analyzed using linear regression.

3.4 Results

Our first set of simulations revealed that our modeling framework is able to distinguish between healthy and 22q11.2 DS anatomies. For all model output parameters except minimum LVP activation for touch closure, our assumption of equal variances between the healthy and 22q11.2 DS anatomy groups was upheld ($p > 0.05$), and we used a t test assuming equal variances for the following comparison. However, for minimum LVP activation, the assumption of equal variances was violated ($p < 0.0001$), so we used a t test assuming unequal variances for LVP activation comparison between our groups. Model predictions of LVP muscle force required were not significantly different between healthy and 22q11.2 DS anatomy groups ($p > 0.05$); however, minimum LVP activation and LVP shortening were both significantly lower ($p = 0.0171$ and $p = 0.0025$ respectively) in the healthy group than in the 22q11.2 DS anatomy group

(Figure 3.4). The model predicted higher maximum closure forces for the healthy control anatomies than 22q11.2 DS anatomies ($p < 0.0001$).

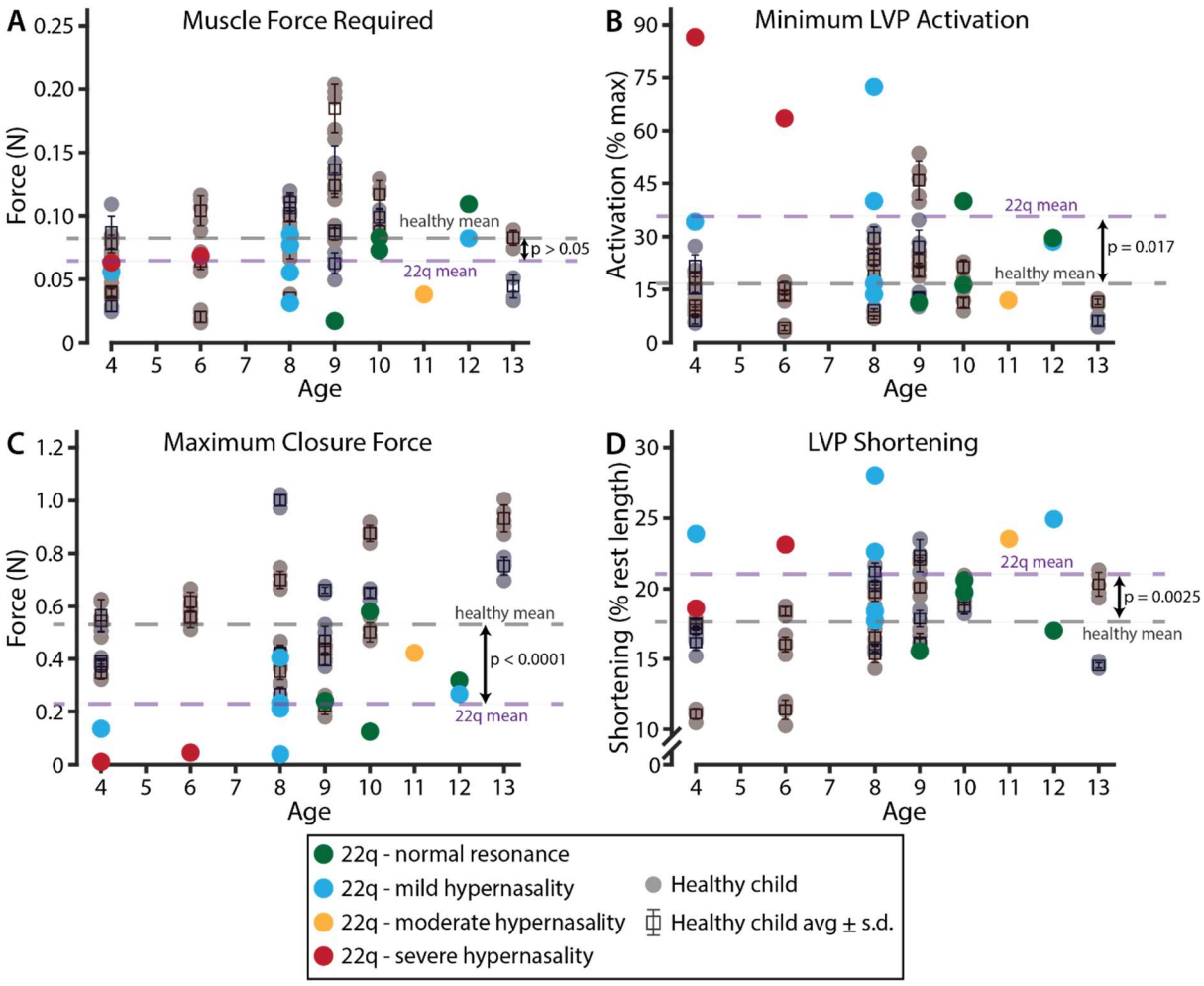

Figure 3.4 Model predictions of outputs
Assuming that lower minimum LVP activation, less LVP shortening, and greater closure force are indicative of better VP function, healthy anatomies are more advantageous for achieving VP closure. **A**. Model predictions of LVP muscle force required are variable across the healthy and 22q anatomies; however, differences between groups were not statistically significant. **B**. Minimum LVP activation to touch closure, as predicted by the model, is significantly higher for 22q anatomies than for healthy control anatomies. **C**. Predictions of maximum closure force are significantly lower for 22q anatomies compared to healthy control. **D**. Similar to minimum LVP activation, LVP shortening is greater in 22q anatomies than healthy controls.

Model-predicted LVP muscle force required for closure positively correlated with VP port depth in healthy anatomies ($R^2 = 0.7142$, $p < 0.0001$), indicating that deeper VP ports require more LVP muscle force for closure. This relationship was not significant in the 22q11.2 DS anatomies (Figure 3.5A). No other parameter was a statistically significant predictor of muscle force required. Minimum LVP activation significantly correlated with VP port depth in both healthy ($R^2 = 0.6278$, $p<0.0001$) and 22q11.2 DS anatomies ($R^2 = 0.4380$, $p = 0.0137$) (Figure 3.5C). Additionally, in 22q11.2 DS anatomies, minimum LVP activation significantly correlated with LVP CSA ($R^2 = 0.4171$, $p = 0.0171$). Closure force in 22q11.2 DS anatomies significantly positively correlated with origin-to-origin distance ($R^2 = 0.3967$, $p = 0.0211$), extravelar LVP length ($R^2 = 0.3222$, $p = 0.0430$), and LVP CSA ($R^2 = 0.8819$, $p < 0.0001$). Closure force in healthy anatomies also positively correlated with LVP CSA ($R^2 = 0.7304$, $p < 0.0001$) (Figure 3.6). Finally, in both healthy and 22q11.2 DS anatomies, LVP shortening positively correlated with VP port depth ($R^2 = 0.7759$, $p < 0.0001$ and $R^2 = 0.6339$, $p = 0.0011$ respectively) (Figure 3.5B), and LVP shortening in healthy anatomies positively correlated with VP port width ($R^2 = 0.2086$, $p = 0.0190$). All regression results can be found in Table 3.2.

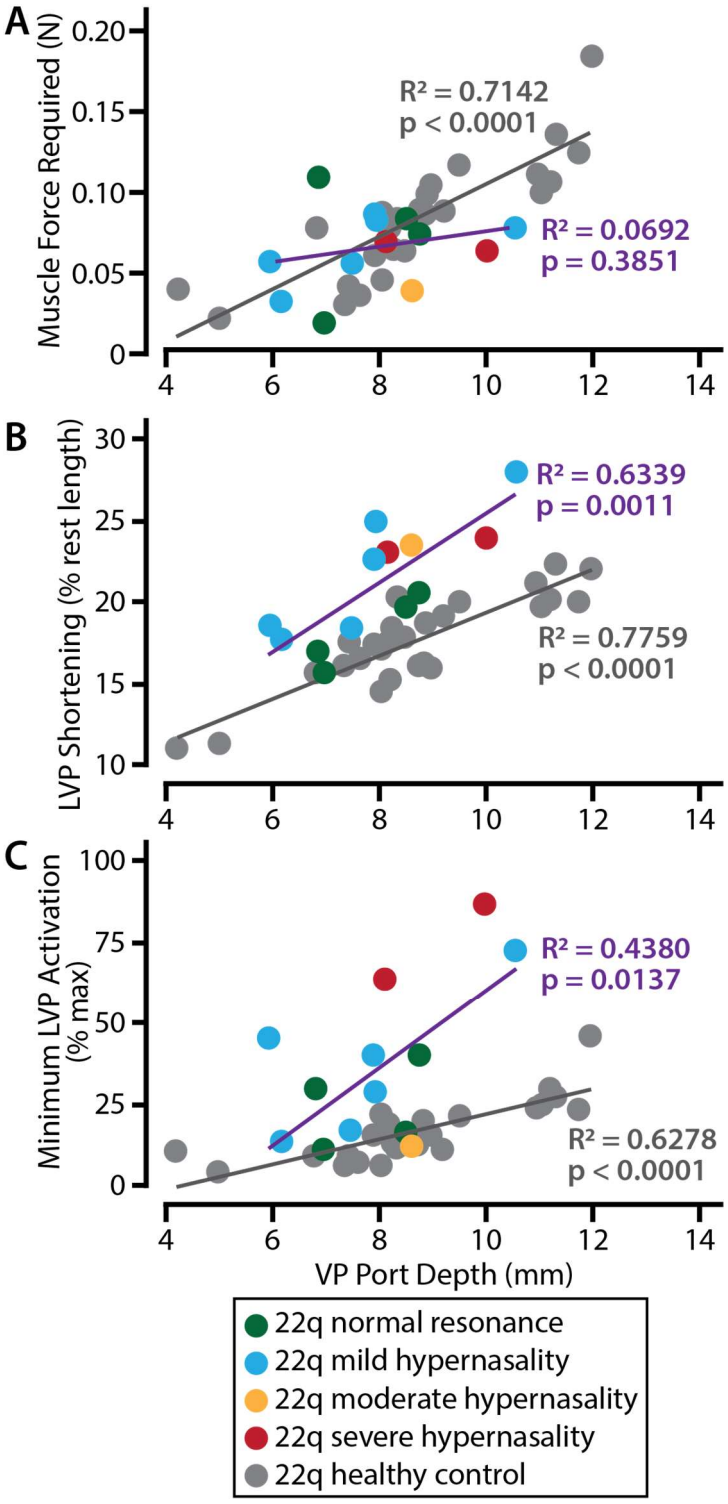

Figure 3.5 Model outputs versus VP port depth
(A) Muscle force required positively correlated with VP port depth in healthy anatomies but not 22q11.2Ds anatomies. However, both (B) LVP shortening, and (C) minimum LVP activation positively correlated with VP port depth for both healthy and 22q11.2DS anatomies.

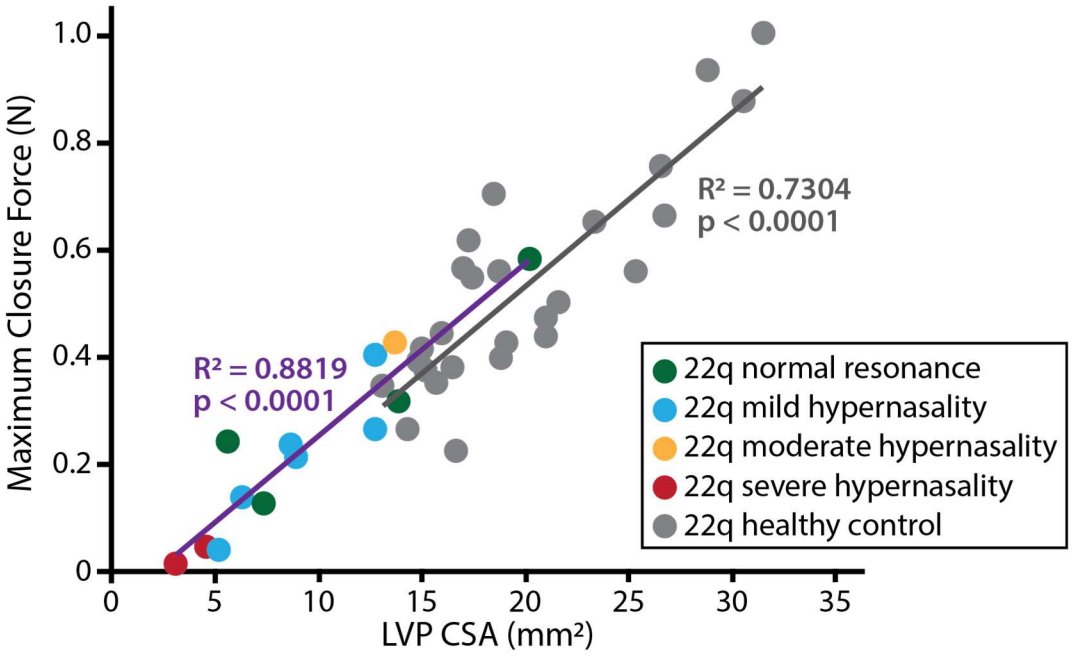

Figure 3.6 Maximum closure force versus LVP CSA
In both healthy and 22q11.2DS anatomies, maximum closure force significantly positively correlates with levator veli palatini cross-sectional area (LVP CSA).

	Muscle Force Required				Minimum LVP Activation				Closure Force				LVP Shortening			
	healthy		22q11.2DS		healthy		22q11.2DS		healthy		22q11.2DS		healthy		22q11.2DS	
Input Parameter	**R^2**	**p value**	**R^2**	**p value**	**R^2**	**p value**	**R^2**	**p value**	**R^2**	**p value**	**R^2**	**p value**	**R^2**	**p value**	**R^2**	**p value**
Effective Velar Length	0.0348	0.3616	0.0916	0.3149	0.0086	0.6517	0.0003	0.9533	0.0008	0.8941	0.0706	0.3801	0.0015	0.8494	0.0053	0.8129
Velum-LVP Angle	0.0011	0.0874	0.2577	0.0766	0.0009	0.8875	0.0824	0.3416	0.0073	0.6767	0.1309	0.2245	0.0483	0.2808	0.0228	0.6221
Velar Thickness	0.0276	0.4172	0.2868	0.0593	0.0000	0.9769	0.2075	0.1177	0.0765	0.1715	0.2039	0.1214	0.0082	0.6602	0.2335	0.0944
Origin-to-Origin	0.0766	0.1711	0.0017	0.8923	0.0419	0.3157	0.2411	0.0884	0.0011	0.8743	**0.3967**	**0.0211**	0.0047	0.7383	0.2001	0.1254
Extravelar LVP Length	0.0777	0.1678	0.0018	0.8896	0.0222	0.4678	0.1884	0.1384	0.0637	0.2137	**0.3222**	**0.0430**	0.0377	0.3417	0.1013	0.2891
Velar Insertion Distance	0.0610	0.2238	0.1307	0.2249	0.0327	0.3764	0.1923	0.1339	0.0200	0.4910	0.1305	0.1712	0.0788	0.1648	0.0030	0.8592
VP Port Depth	**0.7142**	**<0.0001**	0.0692	0.3851	**0.6278**	**<0.0001**	**0.4380**	**0.0137**	0.0114	0.0915	0.0756	0.3634	**0.7759**	**<0.0001**	**0.6339**	**0.0011**
VP Port Width	0.1252	0.0761	0.1434	0.2020	0.1322	0.0678	0.0068	0.7885	0.0026	0.8044	0.0093	0.7538	**0.2086**	**0.0190**	0.0017	0.8925
LVP CSA	0.0111	0.6091	0.0981	0.2973	0.0993	0.1169	**0.4171**	**0.0171**	**0.7304**	**<0.0001**	**0.8819**	**<0.0001**	0.0117	0.5986	0.0419	0.5024

Table 3.2 Regression results between model input parameters and model outputs.
Statistically significant results ($p<0.05$) in bold. Plots of example statistically significant regression relationships are in **Figure** 3.5 and **Figure** 3.6.

When clustering all input parameters, the sets of parameters from 22q11.2 DS anatomies clustered together with two exceptions; both 10-year-old female anatomies with normal resonance clustered with healthy control anatomies (Figure 3.7A). Only two normal resonance 22q11.2 DS anatomies clustered with healthy anatomies when clustered by model-predicted closure force, minimum LVP activation, LVP shortening, and geometrically calculated LVP length at rest (Figure 3.7B). The remaining 22q11.2 DS anatomies clustered separately from healthy anatomies. One of the 10-year-old female normal resonance anatomies remained clustered with healthy, while the other moved to the 22q11.2 DS cluster. The 9-year-old male normal resonance anatomy moved from the 22q11.2 DS input cluster to the predominantly healthy anatomy cluster.

Our second set of simulations revealed that the advantageousness of certain anatomical features varies widely across 22q11.2 DS anatomies. For example, substitution of healthy values of LVP CSA led to the greatest decreases in minimum LVP activation, ranging from 51% decrease to a 79% decrease (Figure 3.8). Substituting effective velar length decreased LVP activation for all but one 22q11.2 DS anatomy, whereas substituting healthy velar thickness increased LVP activation for all 22q11.2 DS anatomies. When substituting the healthy control value for VP port depth, results were mixed; for normal resonance and some mild hypernasality anatomies, LVP activation increased, but for the moderate and severe hypernasality anatomies, LVP activation decreased. Table 3.3 contains the percent change in each output metric for substitution of each input parameter grouped by resonance category.

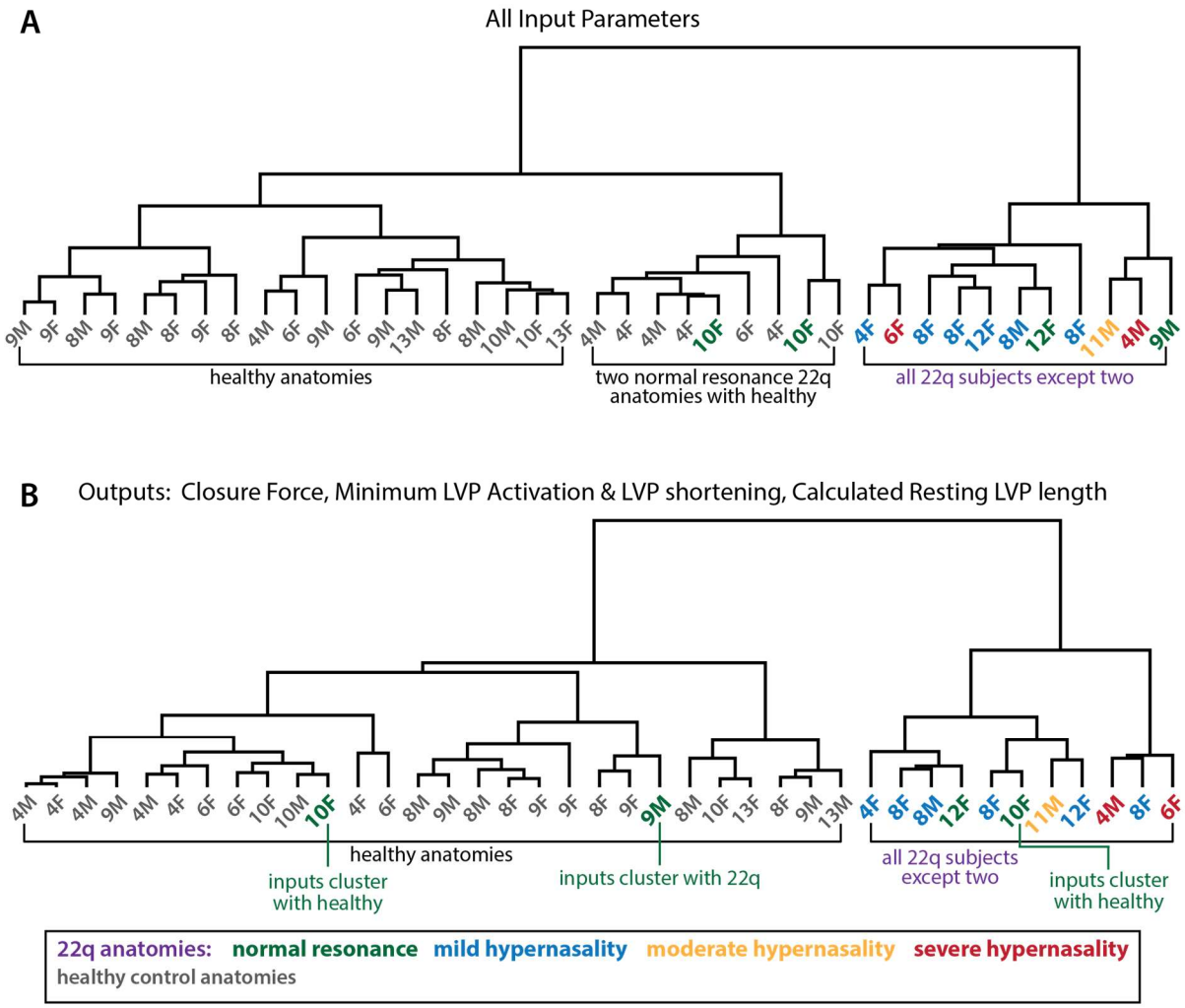

Figure 3.7 Clustergrams of Model Inputs and Outputs

A. Only two normal resonance 22q11.2DS anatomies cluster with the healthy anatomies when including all input parameters as cluster variables; the remaining 22q anatomies cluster together separately from healthy. **B**. Similarly, when clustering based on model-predicted closure force, minimum LVP activation, LVP shortening, and geometrically calculated LVP length at rest, all but two 22q anatomies cluster separately from healthy

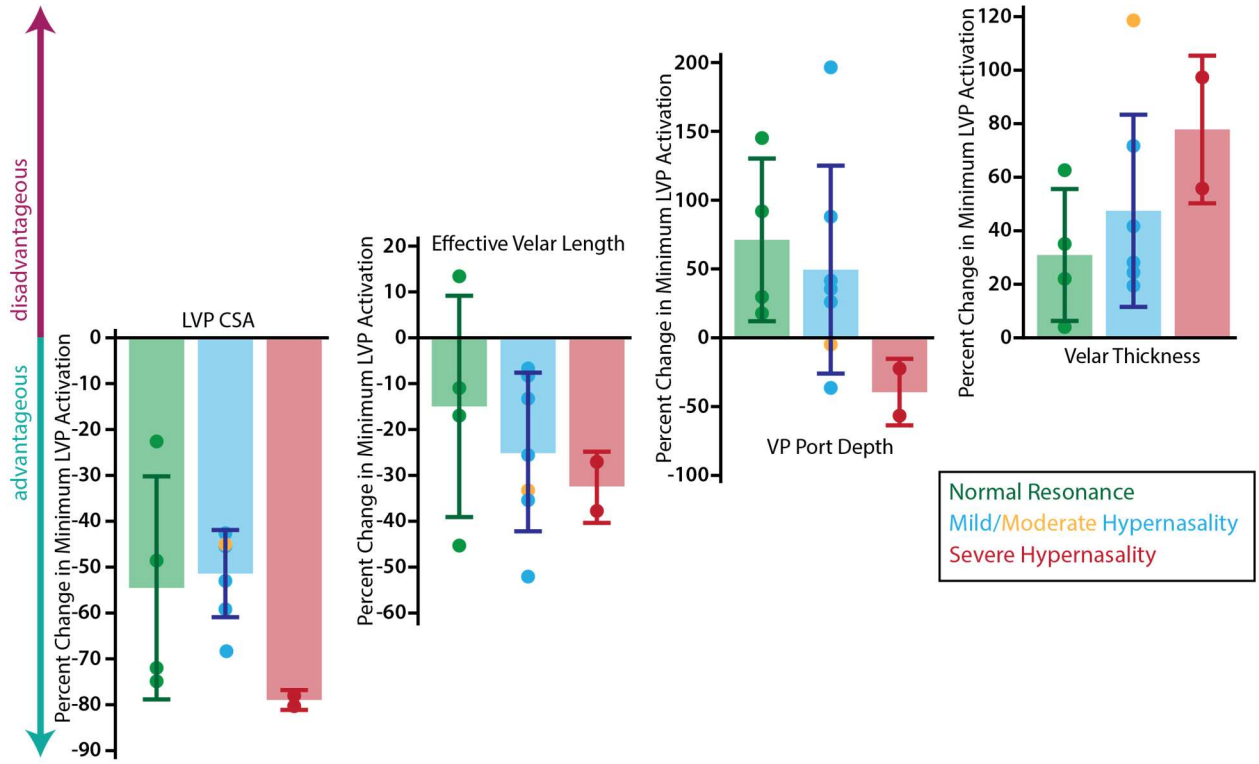

Figure 3.8 Effect of various parameter substitutions on minimum LVP activation
Substitution of healthy control LVP CSA values decreased minimum LVP activation in every 22q11.2 DS anatomy while substitution of healthy velar thickness increased model predictions of minimum LVP activation. Substitution of most anatomical parameters, such as effective velar length and VP port depth, advantaged some anatomies and disadvantaged others, as determined by model predictions of minimum LVP activation.

	Muscle Force Required						Minimum LVP Activation					
	normal resonance		mild/mod hypernasality		severe hypernasality		normal resonance		mild/mod hypernasality		severe hypernasality	
Input Parameter	**mean**	**S.D.**	**mean**	**S.D.**	**mean**	**S.D.**	**mean**	**S.D.**	**mean**	**S.D.**	**mean**	**S.D.**
Effective Velar Length	-15%	24%	-25%	17%	-32%	8%	-15%	24%	-25%	17%	-32%	8%
Velum-LVP Angle	5%	51%	-4%	29%	14%	32%	5%	51%	-4%	29%	14%	32%
Velar Thickness	31%	25%	48%	36%	78%	28%	31%	25%	48%	36%	78%	28%
Origin-to-Origin	37%	30%	-665%	2023%	-234%	549%	30%	24%	83%	154%	9%	154%
Extravelar LVP Length	-11%	14%	-22%	6%	-34%	0%	-12%	14%	-26%	6%	-36%	0%
Velar Insertion Distance	-3%	15%	-2%	11%	-1%	1%	-2%	20%	-2%	16%	-5%	2%
VP Port Depth	61%	50%	42%	65%	-36%	23%	71%	59%	50%	76%	-39%	24%
VP Port Width	5%	12%	6%	11%	21%	18%	9%	21%	10%	16%	25%	21%
LVP CSA	-	-	-	-	-	-	-55%	24%	-51%	10%	-79%	2%
	Closure Force						**LVP Shortening**					
	normal resonance		mild/mod hypernasality		severe hypernasality		normal resonance		mild/mod hypernasality		severe hypernasality	
Input Parameter	**mean**	**S.D.**	**mean**	**S.D.**	**mean**	**S.D.**	**mean**	**S.D.**	**mean**	**S.D.**	**mean**	**S.D.**
Effective Velar Length	2%	8%	12%	12%	145%	139%	-	-	-	-	-	-
Velum-LVP Angle	6%	15%	15%	32%	-42%	82%	-	-	-	-	-	-
Velar Thickness	-9%	10%	-24%	34%	-100%	0%	-	-	-	-	-	-
Origin-to-Origin	-31%	25%	-80%	26%	-100%	0%	-18%	12%	-57%	20%	-59%	36%
Extravelar LVP Length	23%	27%	66%	64%	288%	183%	-2%	3%	-10%	7%	-6%	2%
Velar Insertion Distance	-1%	8%	-5%	15%	15%	15%	-4%	17%	-2%	11%	-8%	7%
VP Port Depth	-27%	18%	-3%	67%	287%	331%	18%	15%	10%	15%	-13%	9%
VP Port Width	-6%	21%	-11%	15%	-63%	52%	12%	25%	5%	8%	5%	3%
LVP CSA	233%	180%	226%	249%	1995%	1476%	-	-	-	-	-	-

Table 3.3 Relative changes in model outputs for substitution of healthy control value
Age-, sex-matched healthy control values were substituted into 22q11.2 DS anatomies for each input parameter

Lastly, changes in input parameters affected the model outputs in varying amounts, as indicated by the slope of the line of best fit between the change in input parameter (from measured baseline) and the raw change in model output from baseline. For example, changes in velum-LVP angle have the greatest effect on changes in minimum LVP activation, followed by changes in VP port depth (Figure 3.9). As noted above, substitution of healthy LVP CSA resulted in the greatest decreases in minimum LVP activation. However, LVP CSA demonstrated the greatest changes in parameter value between baseline and the healthy control value, which leads to the large changes in minimum LVP activation. Regression analysis results, including slope, R^2, and p values, for all relationships between percent change in input parameter and raw change in output are in Table 3.4.

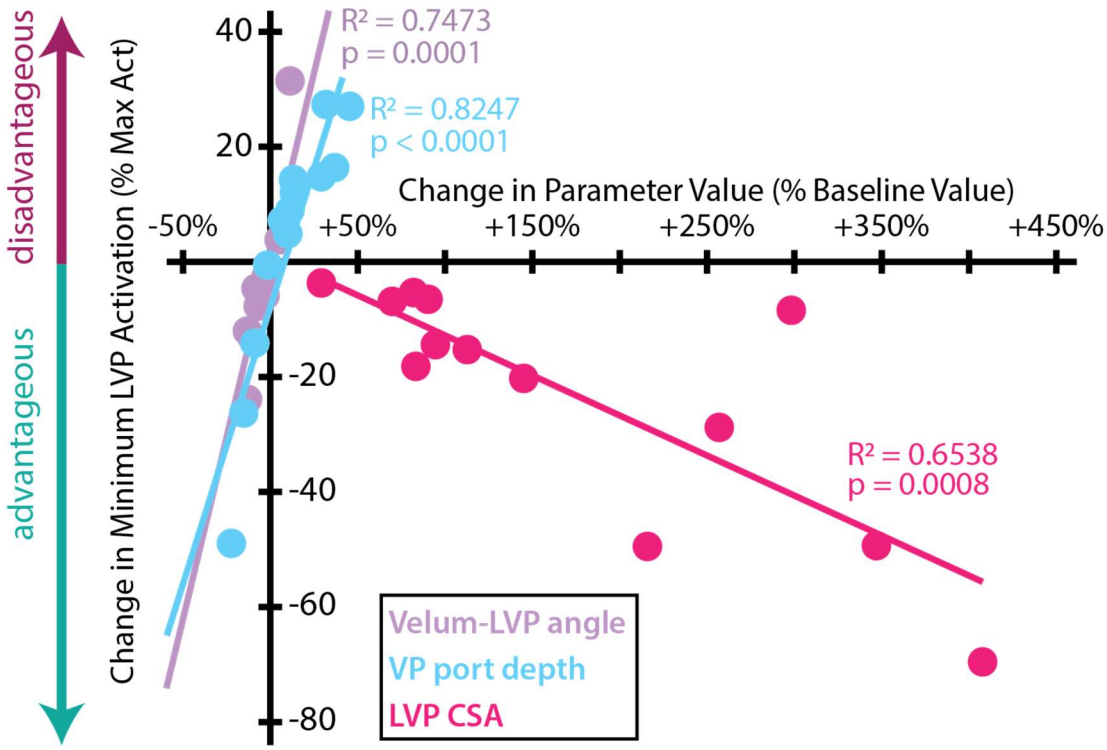

Figure 3.9 Effect of relative changes in input parameters on minimum LVP activation
When healthy LVP CSA values were substituted into 22q11.2 DS anatomies, all 22q11.2 DS anatomies demonstrated the greatest decreases in minimum LVP activation compared to substitution of other input parameters. Substitution of velum-LVP angle values demonstrated the greatest effect on minimum LVP activation per percent change in parameter value. This positive correlative relationship indicates that increases in velum-LVP angle disadvantage VP closure and increase minimum LVP activation.

	Muscle Force Required			Minimum LVP Activation			Maximum Closure Force			LVP Shortening		
Input Parameter	**slope**	**R^2**	**p value**	**slope**	**R^2**	**p value**	**slope**	**R^2**	**p value**	**slope**	**R^2**	**p value**
Effective Velar Length	**-0.0851**	**0.8750**	**<0.0001**	**-0.4229**	**0.4555**	**0.0114**	**0.1289**	**0.8985**	**<0.0001**	N/A	N/A	N/A
Velum-LVP Angle	**0.2197**	**0.9276**	**<0.0001**	**1.2653**	**0.7473**	**0.0001**	**-0.2656**	**0.8953**	**<0.0001**	N/A	N/A	N/A
Velar Thickness	**0.0431**	**0.6310**	**0.0012**	**0.4580**	**0.3871**	**0.0232**	**-0.0274**	**0.3137**	**0.0465**	N/A	N/A	N/A
Origin-to-Origin	-2.0619	0.1208	0.2445	-0.8357	0.0497	0.4641	-0.3242	0.1638	0.1702	**-42.9976**	**0.7748**	**0.0001**
Extravelar LVP Length	-0.0268	0.3110	0.0477	-0.2299	0.1843	0.1432	**0.2110**	**0.5150**	**0.0057**	**-4.9410**	**0.3698**	**0.0275**
Velar Insertion Distance	**0.0305**	**0.8096**	**<0.0001**	**0.2488**	**0.6992**	**0.0004**	**-0.0529**	**0.6591**	**0.0008**	**14.8230**	**0.9812**	**<0.0001**
VP Port Depth	**0.1350**	**0.7553**	**0.0001**	**0.9631**	**0.8247**	**<0.0001**	**-0.3158**	**0.8159**	**<0.0001**	**15.5637**	**0.9402**	**<0.0001**
VP Port Width	**-0.0253**	**0.6181**	**0.0014**	**-0.2601**	**0.3418**	**0.0359**	**0.1756**	**0.6410**	**0.0010**	**-9.3149**	**0.7518**	**0.0001**
LVP CSA	N/A	N/A	N/A	**-0.1392**	**0.6538**	**0.0008**	0.0584	0.2081	0.1172	N/A	N/A	N/A

Table 3.4 Regression results between percent change of each model input parameter and change in model output
Inputs and outputs were relative to each subject baseline valuerelative to baseline model output value respectively. Statistically significant results ($p<0.05$) in bold. An example plot of these regression analyses in Figure 3.9.

3.5 Discussion

In this study, we aimed to investigate how differences in 22q11.2 DS anatomies affect VP function by adapting a previously developed computational modeling framework. Model predictions of minimum LVP activation to closure, maximum closure force, and LVP shortening were significantly different between the healthy control and 22q11.2 DS anatomies. Healthy and 22q11.2 DS anatomies primarily cluster separately when considering either model input parameters or a subset of model outputs. In addition, the effect on VP closure is not consistent when healthy input parameters are substituted into 22q11.2 DS anatomies one at a time; comparable changes in anatomic measures affect VP closure to varying degrees.

A primary assumption of our modeling framework is that lower LVP activation, higher closure force, and less LVP shortening are indicative of an advantageous anatomy with better VP function, as mentioned in (88). The modeling predictions presented here support with that hypothesis. These three outputs statistically differ between healthy and 22q11.2 DS anatomies with the healthy control anatomies remaining more advantageous across the three outputs (Figure 3.4). Within the 22q11.2 DS group, the average closure force was highest for the normal resonance group (0.32 +/- .19 N), compared to the mild or moderate hypernasality group (0.24 +/- 0.14 N) and the severe hypernasality group (0.028 +/- 0.024 N), though none of these differences were statistically significant. This is due at least partially to our small and unequal sample sizes, and we expect these differences would be significant with a larger number of participants in each resonance category.

Model predictions of LVP muscle force required to achieve closure were mostly consistently across our healthy and 22q11.2 DS anatomies. Similar to above, we assume that an

anatomy with biomechanical advantage for VP closure would have a lower LVP muscle force required than a more disadvantageous anatomy. Therefore, to produce the same closure, the disadvantageous anatomy requires greater LVP muscle force, which is possible with a larger LVP CSA, less LVP shortening, or higher levels of activation. Given that the LVP muscles in children with 22q11.2 DS are smaller and shorter (56,97,158) than healthy children and have comparable or deeper VP ports (56,77,97,215), this likely means greater levels of LVP activation and probable fatigue.

Cluster analysis revealed that measures of VP anatomy taken as a group are distinguishable between healthy and 22q11.2 DS anatomies, as expected given the many anatomical differences noted previously (56,77,97,215,226). However, one 9-year-old male normal resonance 22q11.2 DS anatomic switches from the 22q11.2 DS input cluster to the healthy output cluster. Although the majority of his anatomic measures are similar to the remaining 22q11.2 DS measures, some features of his anatomy drive his closure to more resemble closure in healthy anatomies. Although this particular anatomy has a small LVP CSA more similar to 22q11.2 DS anatomies, it also has a long LVP and shallow VP port. This allows for minimal LVP shortening, and due to the force-length relationship, less reduction in muscle force production compared to an anatomy with a shorter LVP or deeper VP port.

No one anatomic measure is able to explain the variability demonstrated in VP closure across our subjects. Although our regression results demonstrate that model outputs correlated strongly with certain anatomic measures, no single parameter is sufficient to predict VP closure for a given anatomy. Interestingly, in healthy anatomies, muscle force required for closure is a predictor of minimum LVP activation for touch closure ($R^2 = 0.8025$, $p < 0.0001$), but this does

not hold for 22q11.2 DS anatomies (Figure 3.10). Because the LVP is appropriately sized and positioned to compensate for the rest of VP factors in healthy anatomies, LVP activation follows from required muscle force in a straightforward manner. However, the variability in LVP measures among children with 22q11.2 DS confounds this relationship.

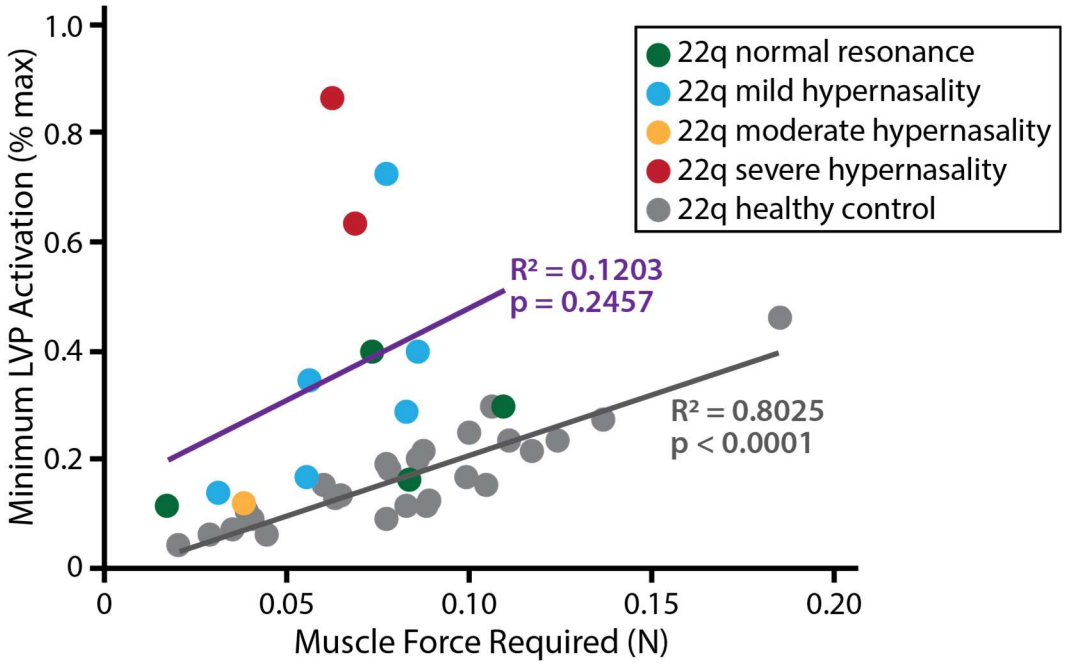

Figure 3.10 Minimum LVP activation versus muscle force required
In healthy anatomies, minimum LVP activation required for touch contact strongly positively correlates with LVP muscle force. However, for 22q11.2DS anatomies, this correlative relationship does not hold.

LVP CSAs were lower in all 22q11.2DS anatomies than healthy matched controls, and changes in VP closure result from those differences. For all 22q11.2 DS anatomies, substitution of healthy LVP CSA values decreased minimum LVP activation and increased maximum closure force more than any other input parameter substitution. CSA is an important muscle parameter because maximum muscle force is proportional to CSA. Increases in LVP thickness and reductions in hypernasality have been demonstrated with continuous positive airway pressure (CPAP) therapy, a sort of resistance training for the LVP and other VP muscles (11,30,105,109). However, additional studies are needed to determine the long-term efficacy of these and other therapies on increasing LVP CSA and improving VP function.

For the purposes of this study, we assumed that LVP muscle in individuals with 22q11.2 DS has the same intrinsic properties as muscle from a healthy individual. Although little is known about the inherent properties of LVP muscles in individuals with 22q11.2 DS, there are documented differences between cleft palate and healthy LVP muscle (73,74,124). However, our modeling framework was able to distinguish between healthy and 22q11.2 DS anatomies based solely on anatomical measures, even with our assumption that 22q11.2 DS muscle behaves the same as healthy muscle.

The simplicity of this modeling framework has significant advantages, such as computational efficiency and ease of parameter adjustment, but there are some drawbacks that warrant mentioning. Our framework represents each component as a line segment, simplifying all geometries and not allowing for analysis of soft tissue deformation of the muscles or velum. However, for rapid adjustment of parameters, as is necessary for this type of computational analysis, low computational cost outweighed geometric complexity. Results

from this work could empower design of future computational modeling studies with greater complexity, e.g. finite element analysis.

Additionally, our modeling framework represents the velum as a spring with spring constant proportional to velar thickness, meaning that thinner velums are more advantageous for VP closure in our models. The velums in our 22q11.2 DS participants were consistently thinner than those in the healthy matched controls, consistent with previous studies (97,226) and at odds with another (185). Therefore, substituting the larger healthy velar thickness values into 22q11.2 DS anatomies results in higher minimum LVP activations (Figure 3.8). However, a too thin velum could result in increased transpalatal transmission of sound and lead to increased perception of hypernasality (79,97,138,158). Therefore, optimal velar thickness is a balance between thin enough to minimize resistance to stretch and thick enough to prevent transmission of sound.

The current simplicity of our model limits our ability to consider the roles of other VP muscles in VP closure. Although the LVP is the primary muscle of VP closure (20,82,169), the LVP cannot account for variability in closure between sounds and subjects (114). In particular, the musculus uvulae assists the LVP in VP closure (20,82,169), but as an intrinsic velar muscle, our current modeling framework is ill-equipped to consider its contribution. However, a main purpose of this study was investigation of 22q11.2 DS anatomies, and the musculus uvulae might not exist in these individuals or be severely hypoplastic (97). Our model also assumes symmetry between right and left sides of LVP muscle, which is often assumed in studies of individuals with healthy VP anatomy (169,211). However, this assumption is likely invalid for individuals with 22q11.2 DS, given documented asymmetries in LVP thickness (158) and upper

airway measures (31). The current modeling framework could be extended to represent asymmetry in future studies, or a more complex modeling techniques could be utilized to quantify the functional effect of VP structural asymmetry.

This study demonstrated that our computational modeling framework is able to distinguish between 22q11.2 DS and healthy anatomies based solely on measurements of anatomic features. In particular, our model predicts that differences in LVP CSA between healthy and 22q11.2 DS anatomies lead to VP functional differences. However, comparable changes in anatomic measures do not affect VP closure equivalently. Although 22q11.2 DS anatomies differ consistently from healthy for some anatomic measures, this assumption is not valid for all VP anatomic measures. Patient anatomy should be considered when performing surgical intervention for VPD in all patients but especially those with 22q11.2 DS.

Chapter 4

The Roles of the Palatopharyngeus and Palatoglossus Muscles in Velopharyngeal Closure Revealed by a Computational Model

Acknowledgements: Vi Tran, Jamie Perry, Silvia Blemker

We will always have STEM with us. Some things will drop out of the public eye and will go away, but there will always be science, engineering, and technology. And there will always, always be mathematics.

- Katherine Johnson

4.1 Abstract

Proper function of the velopharyngeal (VP) mechanism requires coordination of multiple muscles to achieve the closure necessary for healthy speech. However, the contributions of the palatopharyngeus and palatoglossus muscles to closure, especially relative to changes in levator veli palatini (LVP) activation, warrant further investigation. The goals of this study were to (i) construct a 3D finite element model of the VP mechanism, including the LVP, musculus uvulae, palatopharyngeus, and palatoglossus, with geometry based on one subject's VP anatomy, (ii) validate the model with comparisons to subject-specific dynamic MRI and experimental closure force measurements, and (iii) probe the contributions of the palatopharyngeus and palatoglossus muscles to VP closure at various LVP activation states and compare their contributions to those of the LVP and musculus uvulae. Model predictions of velum shape matched well with *in vivo* velum shapes observed in dynamic MRI. In isolation, both the palatopharyngeus and palatoglossus move the velum anteriorly and inferiorly away from the posterior pharyngeal wall, but shortening of neither muscle resulted in large velum displacement. Palatoglossus activation had a greater effect on decreases in closure force than palatopharyngeus activation. For both muscles, the magnitude of this effect was dependent on current LVP activation.

4.2 Introduction

The velopharyngeal (VP) mechanism is a multi-component valve consisting of the hard palate, velum (soft palate), lateral and pharyngeal walls, and associated musculature. The muscles of the VP mechanism coordinate to completely seal the VP port, separating the nasal and oral cavities during speech and swallowing. Much of VP port closure is accomplished by elevation and retraction of the velum, but pharyngeal wall movement may also contribute (163). Proper function of the VP mechanism is required for healthy speech, and velopharyngeal dysfunction (VPD) occurs when complete closure is not possible. VPD is especially common in individuals with repaired cleft palate (115), but the disadvantageous biomechanics leading to VPD are not well understood. However, for improved design and more effective implementation of treatments for VPD, a thorough understanding of healthy VP mechanics is needed (163), particularly regarding the contributions of each muscle to VP closure.

Five muscles have velar insertions, but the levator veli palatini (LVP) is the primary muscle of velar elevation (20,67,82,111,169) and the muscle most considered during primary cleft palate repair (118). The musculus uvulae assists the LVP in VP closure as a slight velar extensor and space occupier near the superior surface of the velum (8,26,83,86,108,178). However, these two muscles cannot account for the variability in velar elevation and VP closure force measured during speech in healthy individuals (107,114,189). The palatopharyngeus and palatoglossus muscles coactivate with the LVP during phonation, but activity in these muscles was more variable than LVP activity and likely sound-dependent (107,131,145). Palatopharyngeus activation adjusted velar position when velum was elevated (189), and the effect of palatoglossus contraction is postulated to depend on velar elevation (130).

Additionally, a given velar position is hypothesized to result from different muscle activation patterns (107,145). Despite decades of insightful experimental work, the roles of these two muscles are still debated and unlikely to be resolved using available experimental methods alone.

Computational modeling has demonstrated utility in investigation of VP function (22,86–88,203). Models can integrate our knowledge of VP anatomy, physical properties, and kinematics from literature to systematically investigate causal relationships. In particular, models can predict quantities that are challenging to measure experimentally or isolate the effects of a specific feature or parameter, such as muscle contraction, on VP closure and velum deformations. This is nearly impossible with observational studies due to limitations in possible *in vivo* measurements and the sheer number of trials necessary to isolate the effects of specific parameters. Previous finite element modeling studies to examine VP function have included only the LVP or LVP and musculus uvulae (86,87) or been limited to two dimensions and used force vectors to represent muscle contraction (22,203). A recent study included all five VP muscles to investigate muscle activation in obstructive sleep apnea but grouped all the muscles together in one layer and did not simulate VP closure (128). To explore the roles of individual muscles in VP closure and how these contributions could differ in various contexts, a three-dimensional (3D) model that includes individual geometric representations of each muscle is necessary.

The goals of this study were to (i) construct a 3D finite element model of the VP mechanism, including the LVP, musculus uvulae, palatopharyngeus, and palatoglossus, with geometry based on one subject's VP anatomy, (ii) validate the model with comparisons to

subject-specific dynamic MRI and experimental closure force measurements, and (iii) probe the contributions of the palatopharyngeus and palatoglossus muscles to VP closure at various LVP activation states and compare their contributions to those of the LVP and musculus uvulae. We created a model that could replicate mid-sagittal velum configurations demonstrated in dynamic magnetic resonance imaging (MRI) and corresponded well with experimental closure force data. The model predicted that palatopharyngeus and palatoglossus contraction both oppose VP closure but palatoglossus activation had a greater effect on closure force decreases than palatopharyngeus activation. For both muscles, the magnitude of this effect was dependent on current LVP activation, as was the effect of musculus uvulae activation on closure force.

4.3 Methods

Imaging

One healthy adult male, aged 27 years with body mass index under 27, with normal VP anatomy and perceptually healthy speech was scanned on a 1.5 Tesla Siemens Avanto scanner with head and neck coil arrays. The static, anatomical scan consisted of a three-dimensional (3D), high-resolution, T2-weighted turbo-spin-echo (TSE) scan called Sampling Perfection with Application optimized Contrasts using different flip angle Evolution (SPACE) (147) with 256 x 256 mm^2 field-of-view and 1 x 1 x 1 mm^3 resolution (Table 2.1). Using a real-time spiral gradient echo sequence (55), we acquired images of the VP mechanism during production of /sʌ/ and /i/ in the mid-sagittal and oblique-coronal planes simultaneously. The oblique-coronal plane was defined to lie along the length of the LVP muscle. Dynamic images in each slice were acquired

at 18.2 frames-per-second with 1.2 x 1.2 mm^2 in-plane resolution with 156 x 156 mm^2 field-of-view and 8 mm slice thickness.

Model Geometry

We manually outlined the following structures in the static MRI data with boundaries defined similar to previous MRI studies (54,168,169) using OsiriX image processing software (183): velum, posterior pharyngeal wall, LVP, musculus uvulae, palatopharyngeus, palatoglossus, and tensor veli palatini (TVP) tendon. The control points defining these outlines were imported into Autodesk Inventor Professional 2018 (7), the outlines of each structure were reconstructed and smoothed, and the 3D rendering of each structure was created by lofting between outlines (Figure 4.1). The 3D geometry was meshed into tetrahedral elements using Trelis Meshing Pre-processor (37). A mesh sensitivity study was carried out using a nominal model of the velum, posterior pharyngeal wall, and LVP muscle. The relevant material properties and boundary conditions as described below were applied to the nominal model, and 100% activation was applied to the LVP to simulate closure. Three mesh densities (mesh sizes 1 to 3) were tested with 451710, 164775, and 68521 elements respectively. Maximum closure force, velum posterior displacement (retraction), and velum superior displacement (elevation) were calculated for each mesh. All outputs differed by less than 0.5% between mesh sizes 1 and 2. We preceded with mesh size 2 for the full model due to simulation accuracy and for computational efficiency.

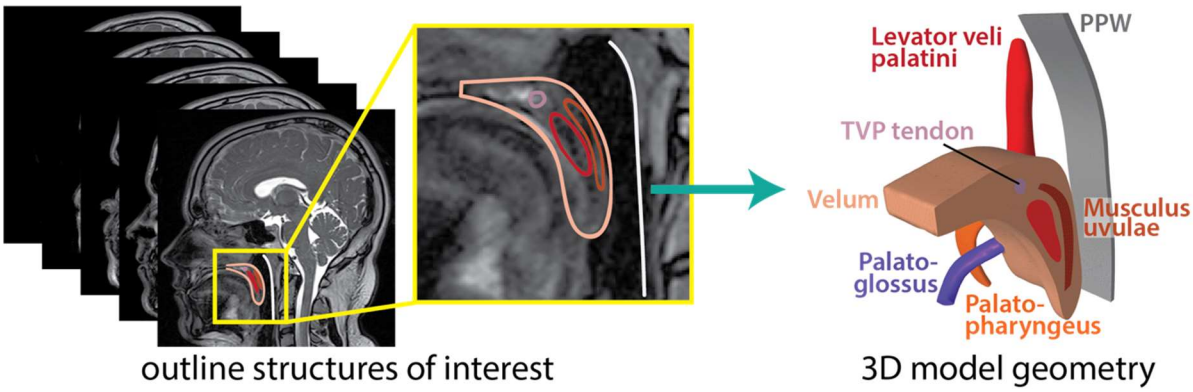

Figure 4.1 Creation of model geometry from three-dimensional static MRI

Material Properties

Each muscle was modeled as a transversely isotropic, hyperelastic, quasi-incompressible material (24,216). A full description of the constitutive model has been published previously (24). Briefly, the strain energy density function separates the deviatoric and dilatational tissue response and is defined as:

$$W(\lambda, \alpha, B_1, B_2, J) = W_1(\lambda, \alpha) + G_1 B_1^2 + G_2 B_2^2 + W_{vol}(J), \quad \textbf{(Equation 4.1)}$$

where λ is along-fiber stretch, α is muscle activation, B_1 is along-fiber shear, B_2 is cross-fiber stretch, and J is volume strain. W_1 incorporates the known force-length relationship of muscle with active and passive components (228), in which activation (α) scales the active force-length curve. Stress and strain are related by:

$$\boldsymbol{S} = 2\frac{\partial W}{\partial \boldsymbol{C}} \quad \textbf{(Equation 4.2)}$$

where $\mathbf{S}$ is the Second Piola-Kirchoff stress tensor and $\mathbf{C}$ is the right Cauchy-Green deformation tensor. Fiber directions for each muscle were determined using Laplacian flow simulations (71,85), and each muscle contracts along its fiber direction.

The velum was modeled as a nearly incompressible, Neo-Hookean material with a Young's modulus of 40 kPa. The TVP tendon was also modeled as nearly incompressible, Neo-Hookean with a Young's modulus of 270 MPa, similar to (72). The posterior pharyngeal wall was represented as an immovable rigid body consistent with previous studies (85,86).

Boundary Conditions

The anterior face of the velum was fixed in all directions to replicate attachment to the bony hard palate. Similarly, the surface representing the LVP origin was held fixed to represent attachment to the petrous portion of the temporal bone (25,82). For both the palatopharyngeus and palatoglossus, the extravelar end of each muscle was attached to a nearly incompressible Neo-Hookean block with Young's moduli of 750 kPa and 500 kPa respectively. Both of these muscles interdigitate with other musculature, rather than attach to bony structures. To represent the constraint on velar displacement caused by the tensor veli palatini (TVP) muscle, the lateral surface of the TVP tendon was attached to a nearly incompressible Neo-Hookean block with Young's modulus of 3 MPa. Finally, a frictionless sliding interface was set between the superoposterior surface of the velum and the anterior face of the posterior pharyngeal wall.

Model Comparison to Dynamic MRI

In the mid-sagittal slice of each dynamic imaging series, we outlined the velum and posterior pharyngeal wall in each frame. We determined the frame of maximum velar elevation and used the corresponding dynamic MRI velum shape for comparison with the model. For model velum shape, we used mid-sagittal velum shape predicted by the model at a given set of muscle activations and compared these shapes to MRI velum shapes by computing the geodesic distance between each pair of curves under the elastic Riemannian metric (202). This type of distance measurement has been exhibited for a variety of shape analyses and comparisons, including distal femur shapes in osteoarthritis (213) and endometrial tissue surfaces (116). We calculated the geodesic distance between each model velum shape and MRI velum shape and determined the minimum for each MRI velum shape (Figure 4.2). We also compared the geodesic distance between our model at rest and an MRI velum shape at rest.

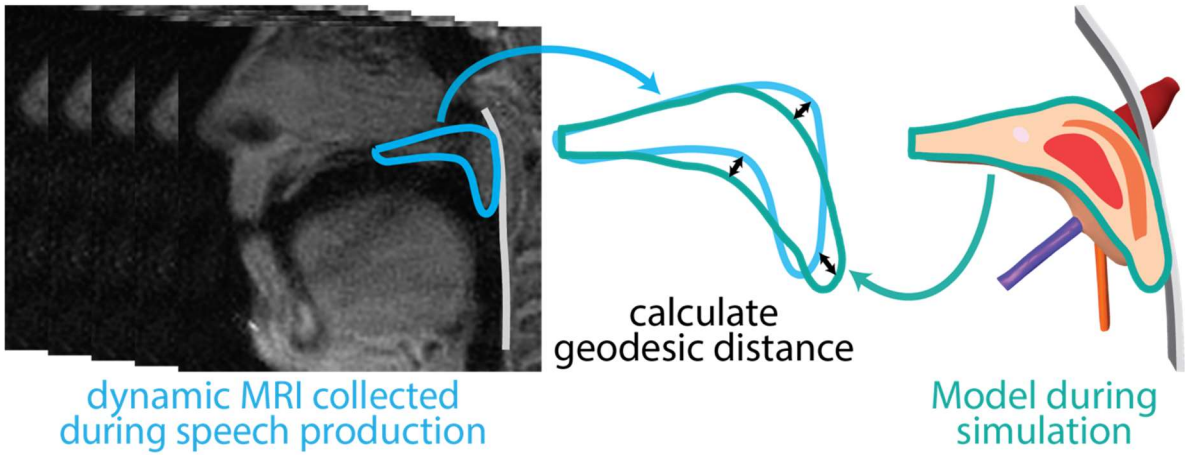

Figure 4.2 Comparison of model and MRI velum shapes

Simulations

All simulations were conducted in the nonlinear implicit finite element solver FEBio (133) and were quasi-static. To simulate VP function, we applied various levels of activation independently to each muscle, ranging from 0 (passive) to 1 (fully activated). In each simulation, we measured closure force, defined as the force exerted on the posterior pharyngeal wall by the velum, at each time step.

We performed four sets of simulations. The first set consisted of eight simulations, in which we fully activated the LVP and between one and three additional muscles. Closure forces predicted by these simulations were compared to experimental closure force data (114). In the second set of simulations, we perturbed activation of each muscle to best replicate the mid-sagittal velum shapes from dynamic MRI described above. For comparison with dynamic MRI, we determined mid-sagittal velum shape at 50%, 60%, 70%, 80%, 90%, and 100% of total simulation time to represent a larger range of muscle activation patterns.

The goal of our third set of simulations was to probe the question: for each muscle, how much does the velum close the VP port for an observed range of a muscle fiber shortening? To explore this, we activated each muscle in isolation and calculated average fiber length for the activated muscle at each time step in our simulations. We compared fiber length to velum displaced distance, defined as the posterior distance the velum has displaced toward contact with the posterior pharyngeal wall. Velum displaced distance equals zero at the start of simulations, and for this model geometry, closure occurred at 10.2 mm, so maximum velum displaced distance was 10.2 mm. If muscle contraction resulted in anterior velum displacement, then velum displaced distance is negative. We defined mechanical advantage for closure to be a

metric of the effect muscle fiber shortening has on velum displaced distance, a pseudo muscle moment arm (191). We calculated this metric as the derivative of fiber length with respect to velum displaced distance; therefore, negative values signify that fiber shortening results in posterior velum displacement (toward closure). Larger magnitudes of mechanical advantage for closure indicate that the velum displaces less for a given amount of fiber shortening compared to a muscle with a lower magnitude of mechanical advantage for closure.

Finally, in our fourth set of simulations, we wanted to investigate how activation of each muscle affects closure force and how this effect varies in different contexts, i.e. different muscle activation states. Therefore, we activated the LVP to 25% and then fully activated each other muscle in isolation with LVP activation constant at 25%. These simulations were repeated for LVP activation states of 50%, 75%, and 100% for the musculus uvulae, palatopharyngeus, and palatoglossus. Additionally, we wanted to examine how the effect of LVP contraction on closure changes in different contexts. We held the musculus uvulae at 25% activation and fully activated the LVP. We repeated this for 50%, 75%, and 100% musculus uvulae activation and those activation states for the palatopharyngeus and palatoglossus. We calculated closure force throughout these simulations and calculated the derivative of closure force with respect to muscle activation for each simulation to quantify how changes in closure force related to changes in muscle activation.

4.4 Results

When activating the LVP to 100% in isolation, our model predictions of closure force compare favorably with experimental closure force data (114); 89% of our simulation data fell within the experimental data mean and standard deviations of closure force (Figure 4.3). Our

simulations predicted greater maximum closure force for coactivation of LVP and musculus uvulae (MU) compared to LVP only simulation (1.38 N versus 1.23 N), as expected given the results of a previous computational modeling study (86). When the palatopharyngeus (PP) coactivated with the LVP, the model predicted a slight decrease in closure force (1.01 N), but when the MU was also activated with the LVP and PP, maximum closure force was nearly recovered (1.22 N). When the palatoglossus (PG) was activated, the model predicted a decrease in closure force for all simulations with the lowest maximum closure force predicted during LVP, PP, and PG coactivation (0.14 N).

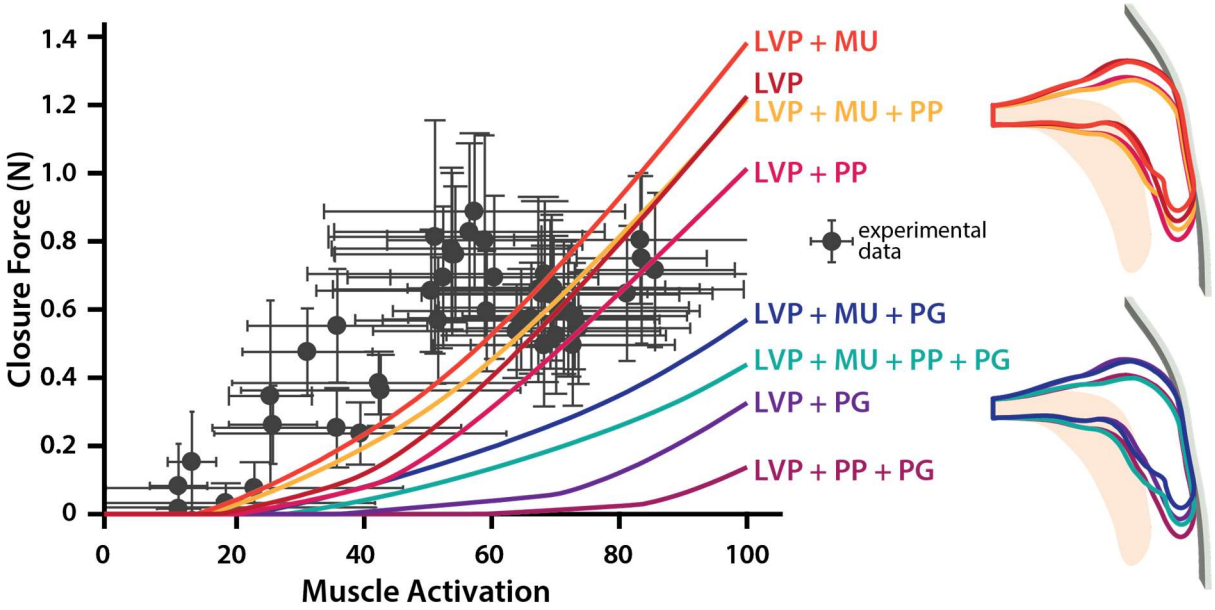

Figure 4.3 Model predictions of closure force
Model closure force predictions compare favorably with experimental data when the palatoglossus (PG) remains passive. Model predictions of velum shapes at full activation are shown.

Our model was able to reproduce velum shapes demonstrated in dynamic MRI and predicted different muscle activation patterns for /i/ and/sʌ/. At rest, model velum shape corresponded well with the velum shape observed at rest in the dynamic MRI (Figure 4.4). The

geodesic distance between the two shapes was 0.1603, and 92% of their within-shape areas overlapped. Our model predicted that the best match for /i/ occurred when LVP, MU, PP, and PG were at 45%, 20%, 35%, and 0% activation respectively, leading to a geodesic distance of 0.2254 (Table 4.1). Of the twenty model-predicted velum shapes with the shortest geodesic distances to /i/ velum shape, all occurred at 44.5 to 47.5% LVP activation, 15 to 30% MU and PP activations, and under 5% PG activation. For /sʌ/, our model-predicted closest velum shape occurred at 79% LVP and 12% MU activation with both the PP and PG passive, yielding a geodesic distance of 0.2116 (Table 4.1). Of the twenty model-predicted shapes closest to /sʌ/, LVP activation ranged from 59.5 to 81% with no more than 16% MU activation, PP activation less than MU activation, and 0% PG activation. For both /i/ and /sʌ/, our model is able to represent the anterior and velar knee regions of the dynamic MRI velum shape well. However, the inferoposterior velum (uvula) is much longer in the model than observed in MRI. There is the possibility that the anterior region of the model velum is too compliant and allows for too much anterior velum stretch, which leads to more velum tissue in contact with the posterior pharyngeal wall; however, the fixed anterior boundary and the constraint on anterior velum movement by the lateral TVP tendon attachment limits the anterior velum from displacing too far posteriorly (under 2.75 mm in 100% LVP activation simulation). Another possibility is segmentation error in our dynamic images due to noise in the region of the image (see Discussion). Our model predictions suggest that there are multiple possible muscle activation patterns capable of producing a given velum configuration, but the range of relative activations between muscles could be limited.

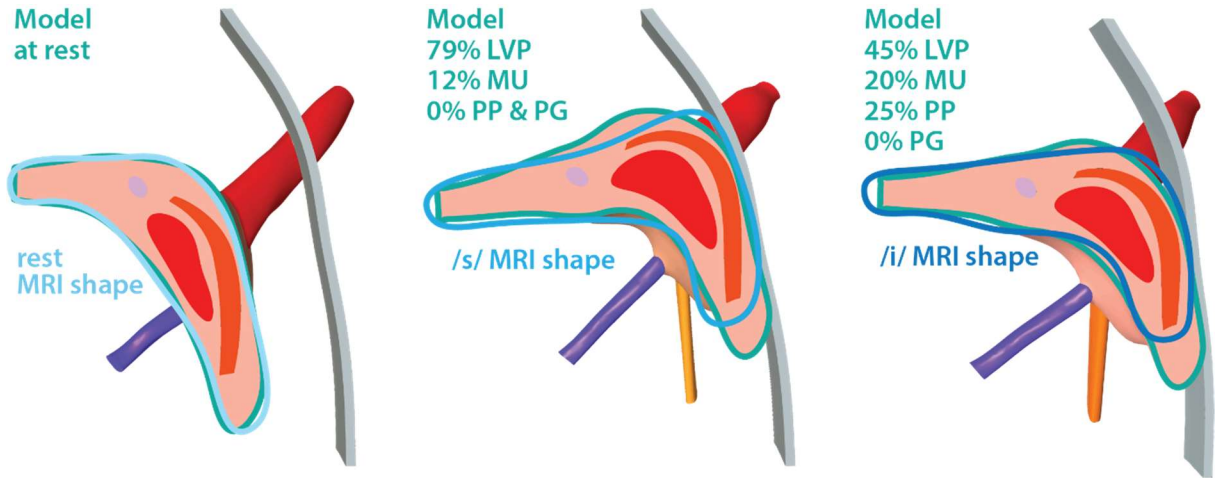

Figure 4.4 Velum shape comparisons between dynamic MRI and model predictions

MRI Shape	Model Activation					geodesic distance
		LVP	MU	PP	PG	
rest	rest	0	0	0	0	0.1603
/i/	closest	45	20	25	0	0.2254
	farthest	25	30	35	15	0.2900
	rest	0	0	0	0	0.2401
/sʌ/	closest	79	12	0	0	0.2116
	farthest	25	30	35	15	0.3298
	rest	0	0	0	0	0.3045

Table 4.1 Geodesic distances between pairs of velum shapes

When activating each muscle in isolation, the LVP was the only muscle able to produce closure. 18.6% activation of the LVP resulted in touch closure when average along-fiber shortening of the LVP was 6.7 mm (Figure 4.6). Contraction of the MU resulted in slight extension of the posterior velum but not enough for any contact between the velum and posterior pharyngeal wall (Figure 4.5). Activation of the PP resulted in inferior displacement of the velum with the posterior velum (uvula) displacing anteriorly. Similarly, PG activation resulted in anterior velum movement. Contraction of both the palatopharyngeus and palatoglossus increased the distance between the velum and posterior pharyngeal wall.

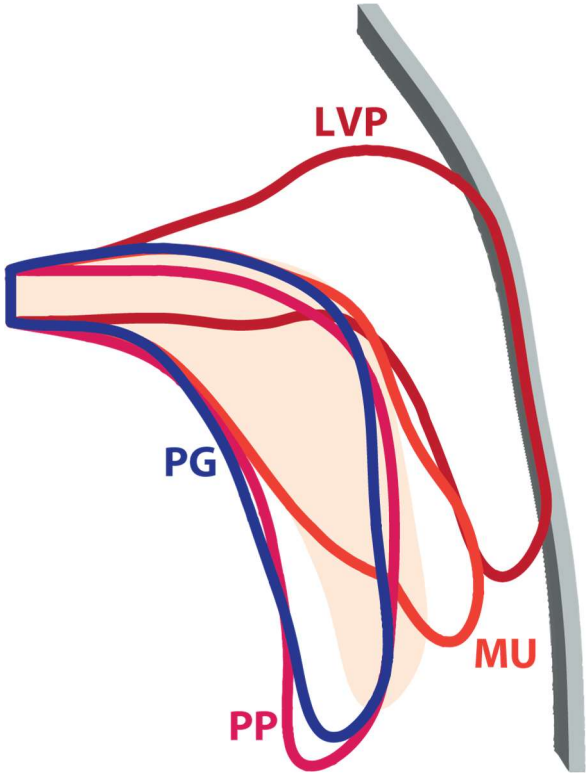

Figure 4.5 Model-predicted velum shapes in muscle isolation simulations

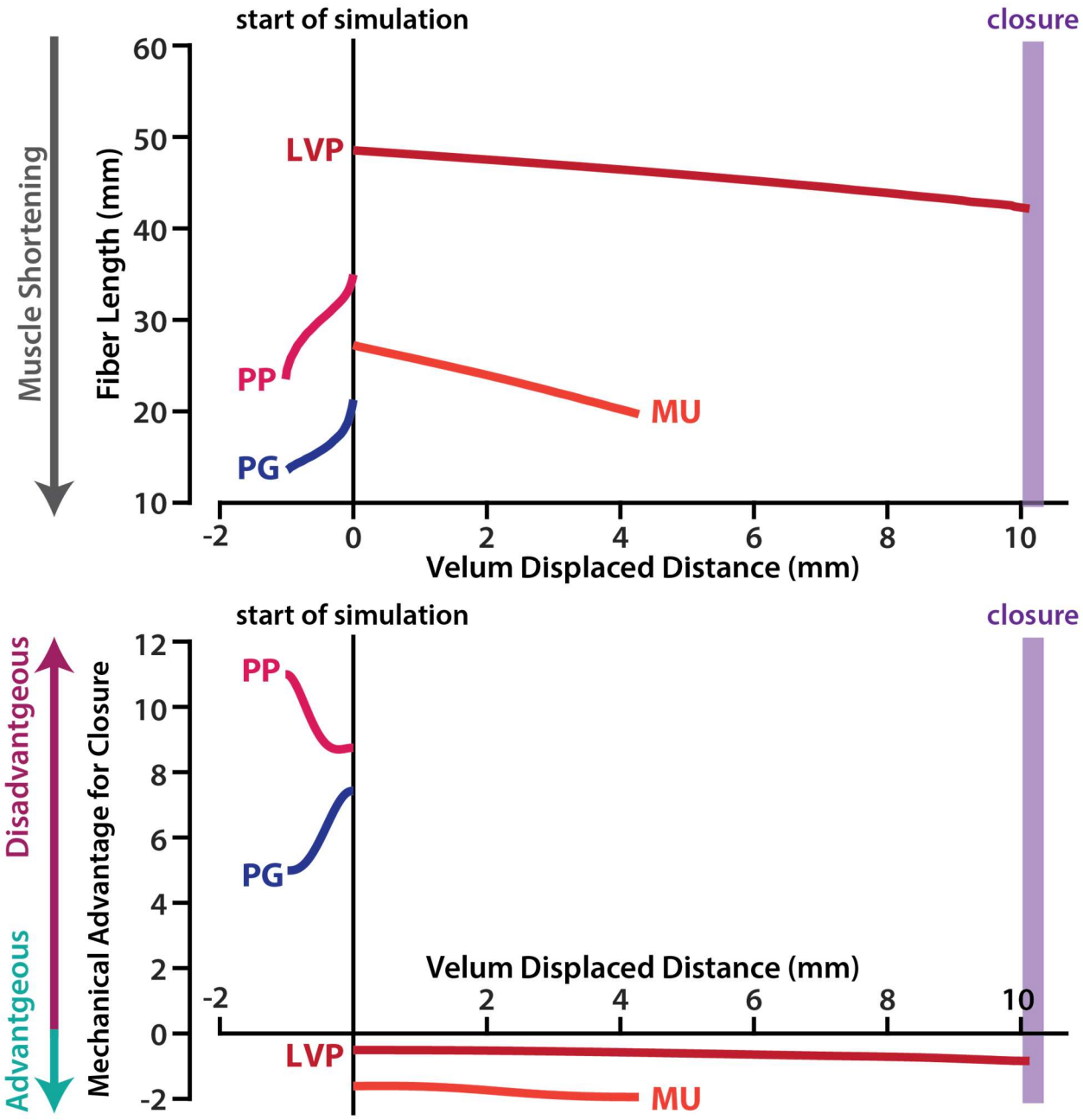

Figure 4.6 Fiber lengths and mechanical advantage for closure
We related these quantities to velum displaced distance for each muscle during muscle isolation simulations.

When examining the mechanical advantage for closure of each muscle, both the LVP and MU had negative values, as expected, which indicates that shortening of their fibers is advantageous for closure. The low magnitude of LVP mechanical advantage suggests that small amounts of LVP fiber shortening result in greater posterior velum displacement toward closure than comparable along-fiber shortening of the MU. Additionally, the LVP mechanical advantage magnitude increases as the velum moves closer to the posterior pharyngeal wall. This indicates that more LVP shortening is required to displace the velum a given distance as the velum nears the posterior pharyngeal wall. Conversely, the large positive values for PP and PG mechanical advantage imply that large changes in their fiber lengths produce minimal velum displacement and in the direction opposite of closure.

Finally, our fourth set of simulations revealed that the effect of MU, PP, and PG contraction on closure force is dependent on the LVP activation state. MU activation consistently increases closure force in all simulated LVP activation states (Figure 4.7). When LVP is at 25% activation, the immediate effect of MU activation on closure force is greater than the effect of low MU activation levels in other activation states. However, as MU activation approaches 100%, the increase in closure force with MU activation, i.e. d(Closure Force)/d(MU act), decreases. In the 50% LVP activation state, when the MU is near 43% activation, increases in MU activation result in the greatest increases in closure force across the MU activation simulations. For 75% and 100% LVP activation states, as MU activation increases, so do corresponding increases in closure force until 65% and 79% MU activation respectively. Thus, the effect of MU activation on closure force primarily increases as MU activation increases

when the LVP is at higher activations, whereas in lower LVP activation states, the effect of MU activation on closure force decreases as MU activates above 50%.

In all LVP activation states, PG activation results in immediate reduction in predicted closure force (Figure 4.8). The effect of PG activation on closure force was dependent on LVP activation state and changed as PG activation increased. With the LVP held at 25%, less than 17% PG activation results in separation of the velum from the posterior pharyngeal wall, i.e. closure force is zero. The effect of PG activation on decreases in closure force, i.e. magnitude of d(Closure Force)/d(PG act) is greater when the LVP is at a higher activation. Overall, the PG is able to lower the velum out of posterior wall contact, and thus reduce closure force, more than the MU is able to increase closure force, as indicated by the relative magnitudes of d(Closure Force)/d(muscle act).

Similar to the PG activation, PP activation reduced closure force in all LVP activation states (Figure 4.9), though to a lesser degree than PG activation. The change in closure force per change in muscle activation was smaller for the PP than for the PG. The small effect of PP activation on closure force supports the hypothesis that the PP adjusts velar position during elevation when the LVP is activated.

In all the muscle activation states simulated, 100% activation of the LVP produced closure (Figure 4.10). The effect of LVP activation on increases in closure force gets larger as LVP activation increases, i.e. d(Closure Force)/d(LVP activation) has positive slope, for nearly all LVP activations in all activation states. Low levels of LVP activation most increase closure force when the MU is activated; however, by 50% LVP activation, these differences have converged.

Overall, the effect of LVP activation on closure force is dependent on LVP activation state, similar to the MU, PP, and PG muscles.

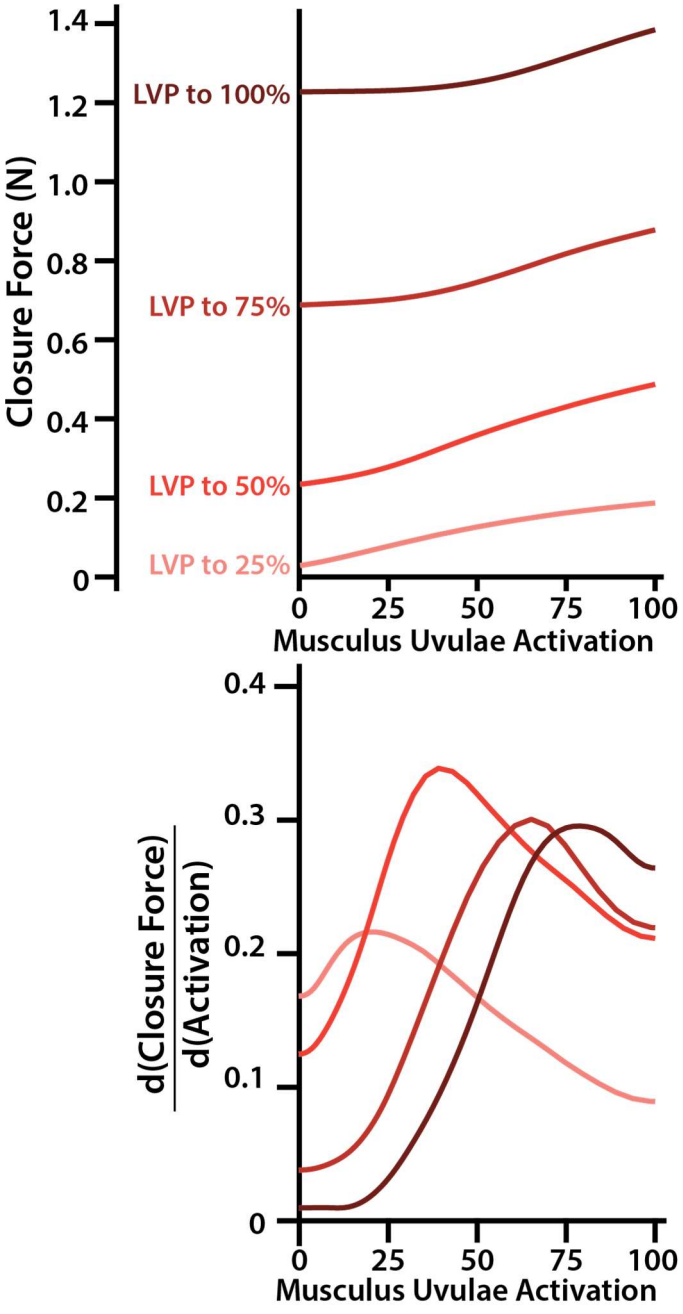

Figure 4.7 Effect of musculus uvulae activation on VP closure force

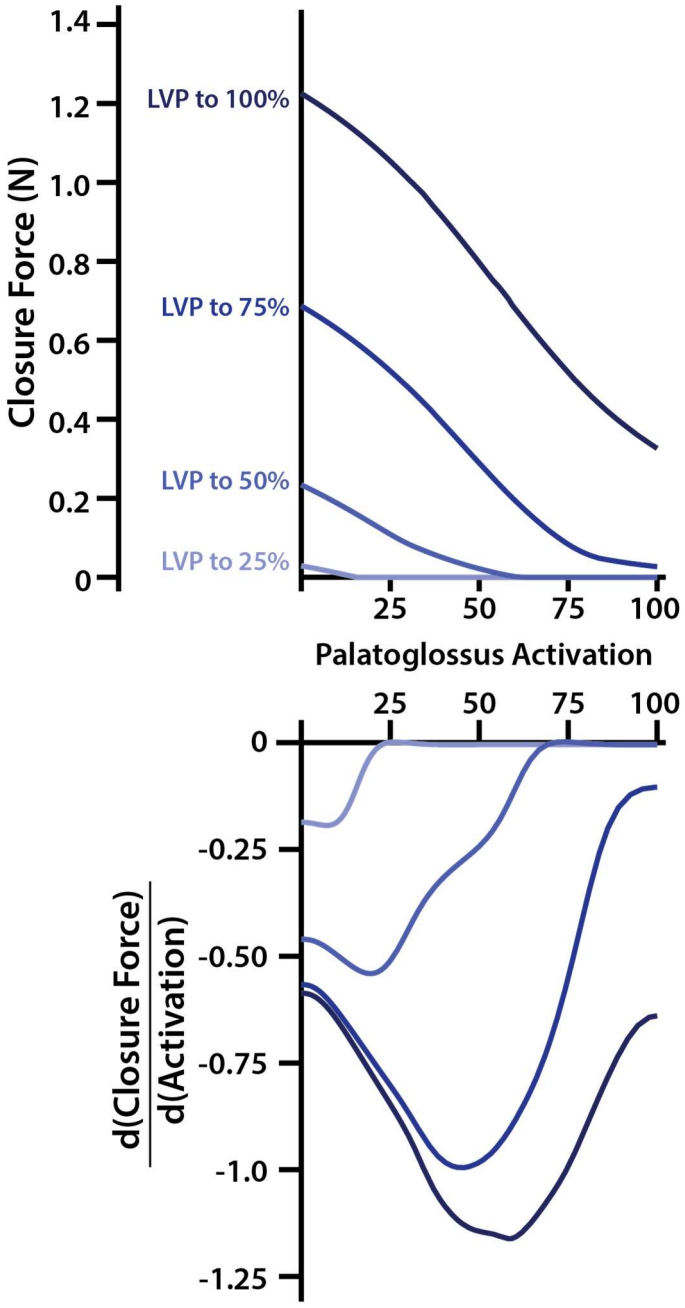

Figure 4.8 Effect of palatoglossus activation on VP closure force

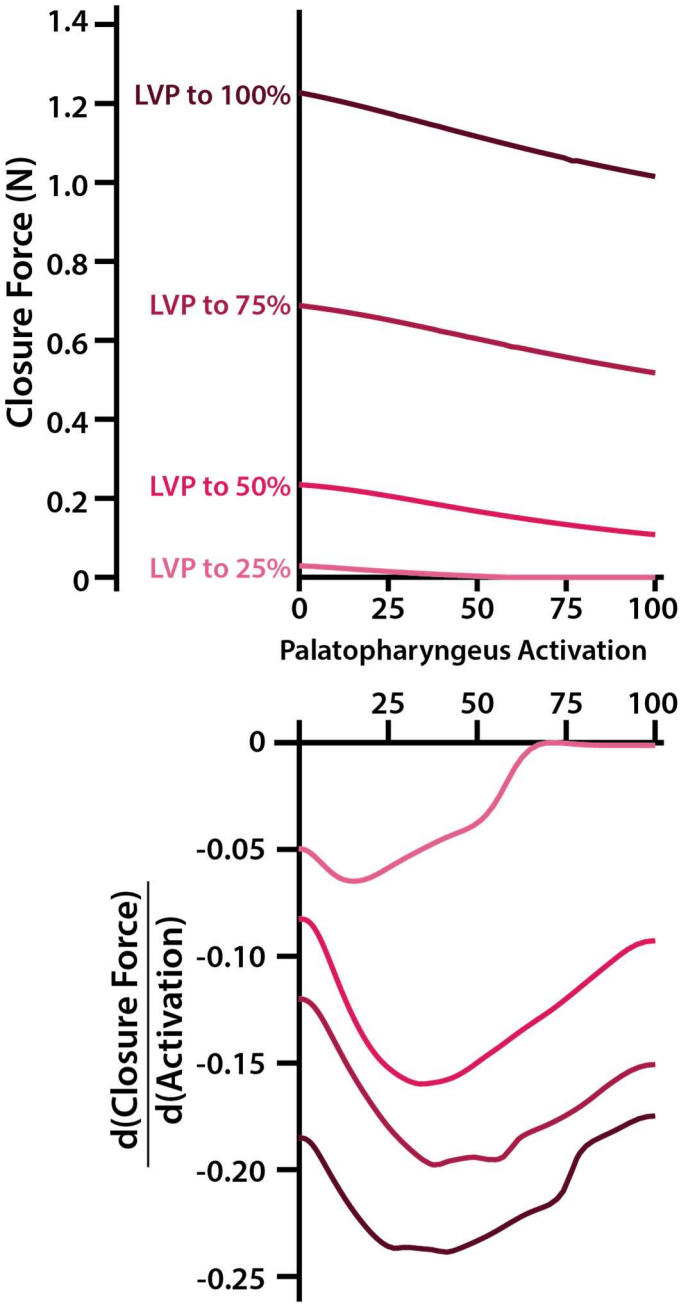

Figure 4.9 Effect of palatopharyngeus activation on closure force

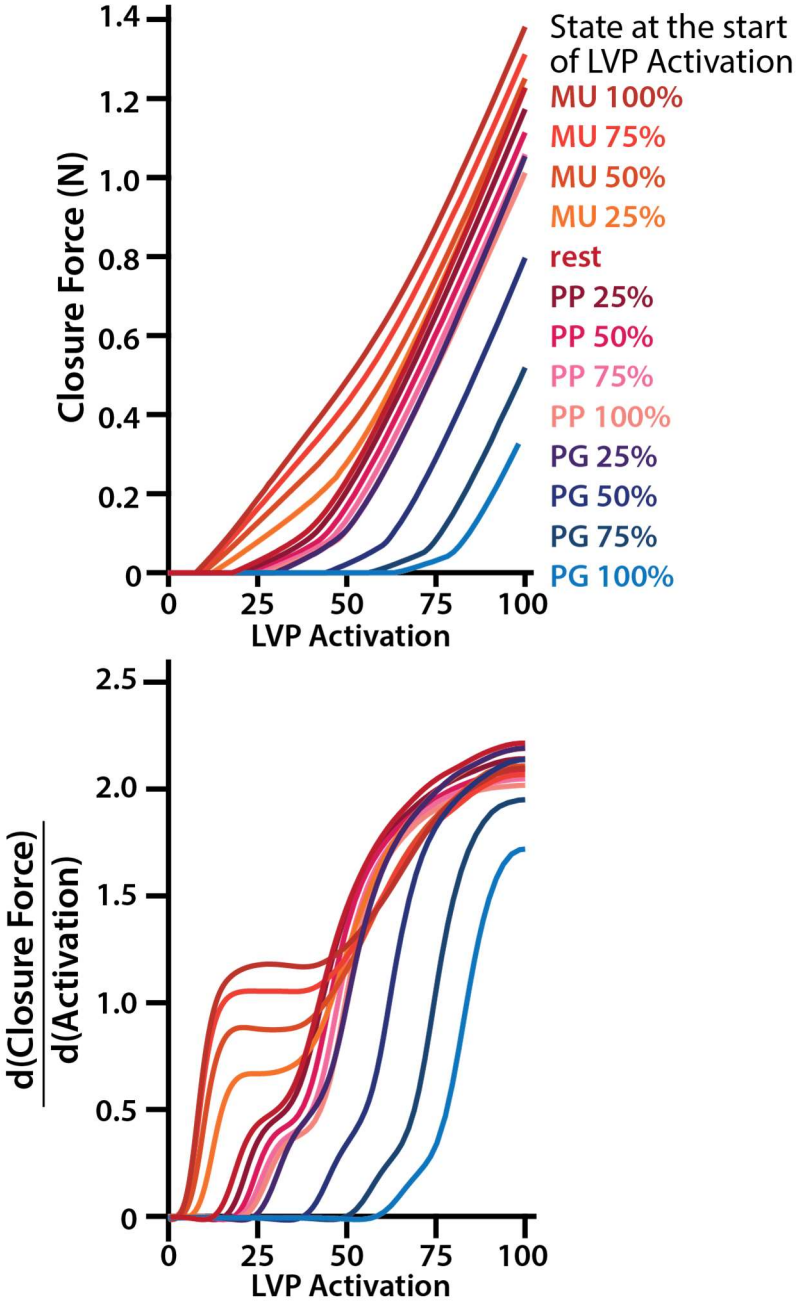

Figure 4.10 Effect of LVP Activation on closure in various activation states

4.5 Discussion

In this study, we created a novel 3D subject-specific finite element model of the VP mechanism to investigate the effect of palatopharyngeus and palatoglossus contraction on VP closure and compare these effects to comparable activation of the LVP and musculus uvulae. Our model was able to reproduce velum shapes demonstrated in subject dynamic MRI and compared favorably with experimental data of VP closure force. Model predictions suggest that the palatopharyngeus works to position the velum during VP closure and slightly opposes LVP contraction. Contraction of the palatoglossus resulted in decreased velar contact with the posterior pharyngeal wall and lower closer forces; thus, the palatoglossus could contribute to velum lowering or VP opening during speech, as previously hypothesized (130). Our model predicted muscle fiber shortening in four VP muscles and used these shortening predictions to compare mechanical advantage for closure between muscles. We also simulated isolated activation of each muscle in various LVP activation states and demonstrated that for each muscle, the effect of muscle activation on closure force varies with LVP activation. This work demonstrates insights possible using computational modeling that are not feasible with current *in vivo* experimental methods alone.

Our predictions of muscle activation pattern during /sʌ/ differ from experimental measurements of LVP, palatopharyngeus, and palatoglossus activations during sustained phonation, while our predictions for /i/ are closer to the reported experimental range (107). We predicted 79% LVP, 12% MU, 0% PP, and 0% PG activation to best replicate the velum shape during /sʌ/. Experimentally, palatopharyngeus activation was greater than zero during sustained /s/ production for all subjects with PP activation higher than LVP activation in two of

five subjects. These differences could be due partly to differences between sustained and natural speech production, as well as variability between individuals. However, the closure force predicted at 79% LVP and 12% MU activation with 0% PP or PG activation is 0.777N, which corresponds well to experimental measurements of /s/ production, ranging from 0.595N to 0.813 N in males, depending on the phonetic context. The model predictions for /i/ muscle activation pattern (45% LVP, 20% MU, 25% PP, and 0% PG) are more similar to experimental data (107). All 5 subjects in (107) had higher levels of PP and LVP activation than PG activation. The model predictions of closure force at that activation pattern is 0.186N, which is below the range reported in (114): 0.476 ± 0.128 N. However, our predictions of muscle activation patterns given velum deformations provide insight into relative muscle activations without invasive methods. This could be especially beneficial in cases where *in vivo* collection of these measurements is not possible, e.g. in children with repaired cleft palate or genetic syndromes.

The variability in muscle activations between subjects is high (107,114), suggesting the importance of subject-specific comparisons. Therefore, we compared LVP shortening predicted by the model to dynamic MRI measurements from Chapter 2. At model-predicted activation for /sʌ/, average LVP along-fiber stretch is 0.768, corresponding to 23.2% shortening. In dynamic MRI, this subject demonstrated 16.8% maximum shortening during /sʌ/ production, which corresponds well to the model-predicted extravelar LVP shortening of 19.4%. Similarly, for /i/, this subject demonstrated 14.8% LVP shortening in dynamic MRI, and the model predicted 18.6% total LVP shortening with 14.7% extravelar LVP shortening. The higher levels of shortening predicted by the model, especially intravelar shortening, could result from the free lateral boundaries of the velum in our model. *In vivo*, the lateral velum is attached to other soft

tissues, limiting its ability to contract laterally. Future modeling work should explore the possible effect of this constraint on LVP shortening and velum deformation.

Overall, the model predictions of closure force and muscle activation compare favorably with *in vivo* experimental data of these quantities (114). This experimental data provides invaluable insight into VP function but demonstrates the variability between individuals, which leads to difficulties drawing conclusions from average or limited data sets. In addition to inter-subject variability, there is the possibility of experimental error or inconsistencies. The force bulb used to measure *in vivo* closure force was calibrated using rigid wooden surfaces (144); however, the velum is a soft tissue and would not deform the force bulb in the same manner as a rigid object, which could lead to variations in closure force measurements. Additionally, placement of electromyography electrodes is challenging for these muscles, and one study demonstrated that electrode placement in the palatoglossus affects the measurement of activity (38).These possible experimental errors and inter-subject variability motivate our subject-specific framework, in which we validate our model with subject-specific dynamic MRI in addition to experimental data available in the literature.

Our model predictions of velum shape aligned well with velum shapes observed in dynamic MRI, especially in the anterior and middle regions of the velum. Our model predicted additional velum length along the posterior pharyngeal wall that was not observed in dynamic MRI. One possibility is that dynamic MRI is not capturing the uvula during velar elevation. Slice thickness in our dynamic images is 8mm, which is approximately the width of the uvula in this subject. The two-dimensional images are averaged through their thickness. Therefore, if the imaging plane was not centered around the uvula, either due to plane orientation or

asymmetric uvular motion during speech, the uvula could appear as noise in the dynamic image. Future studies should compare model-predicted velum shapes to MRI shapes at several time points during velar elevation to determine when the model stops adequately representing the velum shapes observed in dynamic MRI.

Experimental studies have shown mixed results regarding the effect of tensor veli palatini (TVP) activation on velum movement, ranging from no effect to depression of the anterior velum (1,13,49,70,80); however, the importance of the stiff TVP tendon in the anterior velum was noted (13,80). Preliminary computational modeling work agreed with these findings; the model predicted that the TVP muscle benefits closure primarily by its constraint on anterior velum movement, rather than by its activation (160). Because of this and for computational efficiency, our model incorporates the TVP tendon attached to a passive Neo-Hookean block, rather the entire TVP muscle. We tuned the stiffness of the block attachment to best represent the effect of the TVP muscle. We compared simulations of 100% LVP activation in the model described here to 100% LVP activation simulations in a model similar to ours with the addition of TVP muscle and hook of Hamulus geometry. A stiffness of 3 MPa for the attachment block yielded less than 5% difference in closure force predictions and less than 1% difference in velum posterior and superior displacement. However, in future modeling studies of repaired cleft palate anatomies, the effect of the TVP on velum movement should be considered. The TVP is shorter and oriented differently in these anatomies compared to healthy (65); thus, the effect of the TVP on velum movement could differ from healthy anatomies and should be further investigated.

Our model assumes a consistent velum stiffness throughout its length, similar to (86,87), of 40kPa. Although velum stiffness has been shown to vary throughout its length from stiffer near the hard palate to more compliant at the uvula (23,53,110), the use of 40kPa corresponded well with experimental data and *in vivo* velum configurations. Additionally, the experimental velum stiffness measurements include the TVP tendon and musculature of the velum. Inclusion of the TVP in the anterior velum of our model geometry results in a stiffer anterior velum than posterior velum in our model, similar to experimental findings.

The model predictions of closure force are dependent on velum stiffness, and the stiffnesses of the palatopharyngeus and palatoglossus attachments blocks. We performed a sensitivity analysis perturbing the stiffnesses of each material down by 50% (half stiffness) and up by 100% (double stiffness). We performed four simulations for each set of velum, patalopharyngeus block, and palatoglossus block stiffnesses: 100% LVP activation, 100% coactivation of the LVP and musculus uvulae, 100% coactivation of the LVP and palatopharyngeus, and 100% coactivation of the LVP and palatoglossus. Although the magnitudes of closure force were affected, the relative closure forces between the simulations remained the same. Our conclusions regarding the effect of palatopharyngeus and palatoglossus contraction on closure force remain valid, although the magnitudes of these effects could vary depending on velum stiffness and these boundary conditions.

Our model geometry is based on the orientation and location of muscles determined using MRI data from one subject. For the palatopharyngeus muscle geometry, we included the palatopharyngeus bundle identifiable in MRI, but anatomical studies report that the palatopharyngeus is likely two or more muscle bundles (62,206). In addition to the bundle with

primarily superior-inferior oriented fibers, the other major bundle courses more posteriorly from the velum to the superior constrictor (62) and was not included in our model. Based on anatomical dissection, the action of the bundle is hypothesized to act as partial VP port sphincter in conjunction with superior constrictor muscle, which could affect the closure forces and velum configurations predicted by the model. However, even with inclusion of only the primarily inferiorly oriented palatopharyngeus bundle, our model predicted the lowering effect on velar position suggested by previous studies (145,189). Consideration of this additional bundle should be considered in future modeling studies of the VP mechanism.

A critical assumption of our model is that optimal fiber length for each muscle occurs at muscle resting length. Sarcomere lengths in these muscles are currently unknown, but recent developments in minimally invasive *in vivo* imaging of sarcomeres could enable this investigation (186). Optimal fiber lengths different from resting length for any or all of these muscles would affect model predictions of closure force. However, predictions of fiber shortening and velum displaced distance would remain the same, as would the conclusion that for each muscle, the effect of muscle activation on closure force varies between LVP activation states.

Limitations of this framework include the lack of viscoelastic and force-velocity effects in our constitutive formulation. Further model developments should include these effects, which would likely reduce force production but remain near peak muscle power in the LVP, given *in vivo* LVP muscle velocities measured previously (Chapter 2). *In vivo* muscle velocities of the other VP muscles have yet to be investigated. Even with alterations in muscle force and closure force, our demonstration of fiber length and velum displaced distance remains insightful, as it

quantifies the differences in mechanical advantage for closure between the VP muscles. Inclusion of these effects would allow for investigation of the timing between muscle activation and contraction and how this could differ in individuals with VP dysfunction.

In conclusion, we created a novel 3D finite element model of the VP mechanism to probe the contributions of the palatopharyngeus and palatoglossus muscles to VP closure, quantify their effects on closure, and compare to the effects of the LVP and musculus uvulae on closure. Our model predictions of closure force compare favorably with experimental closure force data and agree with a previous computational modeling predictions of the advantageous effect of musculus uvulae contraction on VP closure (86). Our results suggest that the palatoglossus acts primarily to lower the velum away from the posterior pharyngeal wall, opposing the LVP, and the palatopharyngeus pulls the velum inferiorly for possible velum positioning during closure. For both muscles, as well as the LVP and musculus uvulae, the magnitude of their effect on closure is dependent on the current level of LVP activation. The framework presented here is, to our knowledge, the first to couple MRI and finite element model for investigations of VP closure mechanics. Future modeling studies should include additional healthy subjects, especially across a range of ages, sexes, and races, to examine the effect of anatomical variability on palatopharyngeus and palatoglossus function. The framework also empowers subject-specific investigation of VP dysfunction biomechanics. In particular, future work could utilize this framework to determine which anatomical or mechanical features contribute to VP dysfunction in a patient's anatomy and use these insights to inform treatment that optimizes patient outcomes.

Chapter 5

Conclusions

"Roads? Where we're going, we don't need roads"

- Dr. Emmett Brown, *Back to the Future*

5.1 Summary

In this dissertation, we focused on three questions critical to improving our understanding of velopharyngeal (VP) biomechanics: How does anatomy affect VP function in healthy individuals? How do anatomical alterations in children with VP dysfunction affect the structure-function relationship? And how, if at all, do the palatopharyngeus and palatoglossus contribute to VP closure? To answer these questions, we first developed a novel method to measure *in vivo* levator veli palatini (LVP) function using dynamic magnetic resonance imaging (MRI). Second, we coupled MRI with computational modeling to isolate the effects of specific anatomic or mechanical perturbations on VP closure, such as increasing LVP cross-sectional area in children with 22q11.2 deletion syndrome or altering muscle activation in muscles hypothesized to be LVP antagonists. Using these methods, we revealed a previously unknown relationship between VP anatomy and LVP muscle function: LVP muscle shortening and contraction velocity scale with VP port depth. Additionally, we quantified the effect of altered anatomical features on VP closure in children with 22q11.2 DS and probed the effects of palatopharyngeus and palatoglossus contraction on VP closure. These insights further our understanding of the VP structure-function relationship, and the methods developed here can be employed for further investigation of VP biomechanics in healthy and impaired speech populations.

5.2 Contributions

5.2.1 In Vivo Measurements of Levator Veli Palatini Shortening and Contraction Velocity

Although *in vivo* levator veli palatini (LVP) lengths have been reported previously (54,170,175,209), this dissertation is the first to place this functional measurement in the context of the force-length relationship (36,51,66,84,180). In our sample of healthy adults, LVP muscle shortening did not substantially reduce the force-generating potential of the LVP. However, the ascending limb of the force-length curve steepens sharply as fibers continue to shorten from optimal fiber length, greatly decreasing the muscle's force generating ability. Individuals with repaired cleft palate demonstrate greater pharyngeal depths (167), and LVP shortening likely increases as the VP port deepens (see Section 5.2.2). Therefore, the sharp decreases in potential force generation given greater LVP shortening could have important implications in individuals with repaired cleft palate.

Because of our novel methodology and adequate frame rate, we were able to calculate *in vivo* LVP muscle velocities for the first time. Velar velocities during speech have been reported from electromagnetic articulography (EMA) and cineradiography studies (52,104), but they were conducted in the mid-sagittal plane, which is unable to capture LVP function. Muscle contraction velocity is an especially important functional metric given the force-velocity relationship (12,78). Muscle force-generating ability declines substantially with even minimal contraction velocity, although there is a balance between muscle velocity and power, calculated as the product of muscle force and velocity. In our healthy subjects, the measured contraction velocities corresponded to near maximal power output. However, given that LVP contraction velocities scale with VP port depth (Chapter 2), the deeper VP ports seen in

individuals with repaired cleft palate could lead to greater contraction velocities. These higher velocities would lead to both reduced force generation and less muscle power.

5.2.2 Relationship between Levator Veli Palatini Shortening and Velopharyngeal Port Depth

The results of this dissertation are the first to demonstrate the relationship between LVP shortening and VP port depth. We showed this in both healthy adults using dynamic MRI and in children using computational modeling predictions (Figure 5.1). When comparing between the methods, the model overpredicts LVP shortening but by a mostly consistent offset in our healthy adult subjects. Our model predictions of LVP shortening correspond to the maximum closure possible given a subject's anatomy, which in combination with the model's simplification of the intravelar segment, could account for this offset.

Most MRI studies do not measure VP port depth and instead report pharyngeal depth, measured from the posterior nasal spine of the hard palate to the posterior pharyngeal wall (2,10,101,172,175). Tian and Redett found no meaningful predictors of maximal LVP shortening in a group of healthy adults, but they measured only pharyngeal depth, not VP port depth (209). In Chapter 2, we found that relative LVP shortening moderately correlated with pharyngeal depth ($R^2 = 0.6378$), but this relationship did not reach statistical significance ($p = 0.0568$). VP port depth is measured in the oblique-coronal plane of the LVP and is more indicative of the distance the LVP must shorten to achieve VP closure. However, this plane is often left out of imaging studies in favor of a mid-sagittal or axial plane. The results presented in this dissertation support previous work (175) emphasizing the importance of the oblique-coronal plane for understanding VP anatomy, function, and the relationship between them.

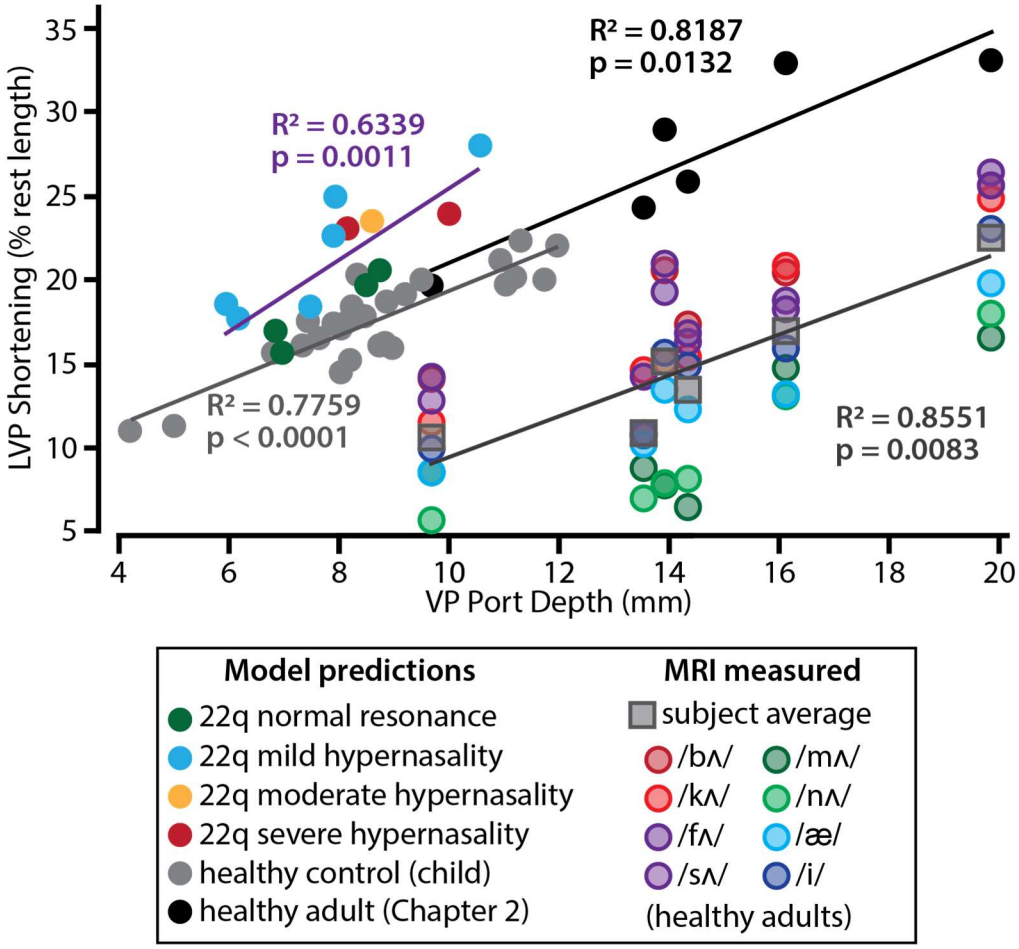

Figure 5.1 Relationship between LVP shortening and VP port depth
Both our dynamic imaging and computational modeling results demonstrate the relationship between LVP shortening and VP port depth.

5.2.3 Functional Differences Caused by Alterations in 22q11.2 DS anatomies

Differences between 22q11.2 DS and healthy VP anatomies are well-documented in MRI studies (45,56,77,97,185,215,226), though specific differences are debated and anatomical departures from healthy likely vary between individuals. Acquiring functional data in this population has been challenging due to behavioral constraints and movement artifacts that are common in this, and any, pediatric population (102). Therefore, the functional implications of these anatomical differences had not been assessed until this dissertation. Speech outcomes in children with 22q11.2 DS have been reported but to our knowledge never related to subject-specific anatomical measures. The modeling framework adapted in Chapter 3 allowed us to fill in the functional gap between anatomy and speech outcomes in children with 22q11.2 DS.

Additionally, this dissertation hypothesizes that differences in LVP cross-sectional area (CSA) play a large role in the reduced VP function of children with 22q11.2 DS. Our model predicted improved VP closure in all of our 22q11.2 DS subjects when LVP CSA was set equal to the age-, gender-matched healthy control value. In general, LVP thickness is reported in anatomical studies of LVP, rather than CSA (11,56,158). Thickness gives a one-dimensional estimate of CSA, and we would expect that increases in thickness imply increases in CSA. However, LVP thickness measurement is dependent on the oblique-coronal plane orientation through the LVP and location along the LVP length; in the oblique-coronal plane, the location of greatest LVP thickness might not correspond to the location of greatest CSA. Muscle force scales with muscle CSA (123), assuming LVP fibers are oriented along the LVP length), signifying the importance of LVP CSA when considering VP function.

5.2.4 Subject-specific Three-dimensional Finite Element Model of the VP Mechanism

In this dissertation, I have developed the first three-dimensional (3D) finite element model of the VP mechanism that includes geometric representation of four VP muscles – LVP, musculus uvulae, palatopharyngeus, palatoglossus, as well as representation of constraints placed on the velum by the tensor veli palatini. A previous finite element model to probe VP function included four VP muscles but was two-dimensional with simplified rectangular geometry of the velum and used force vectors to represent muscle contraction (22). Other existing finite element models examining VP closure included at most two muscles with no representation of the remaining musculature by force vector, constraint, or otherwise (86,87,203). A recent finite element model of the upper airway, including velum, included fiber directions for all VP muscles but combined them into one thin geometric layer within the velum to examine airway collapse in obstructive sleep apnea patients (128). With four muscles represented individually in our model, we could isolate and quantify the effects of each muscle's activation on VP closure and compare between muscles.

We sought to answer two questions about the contributions of each muscle to VP closure: (i) How much does the velum displace posteriorly (toward closure) for a range of muscle fiber shortening? (ii) How does muscle activation affect closure force and how does this effect change with changes in LVP activation or velar elevation? To explore these questions, we developed two new metrics to quantify the effectiveness of a muscle at contributing to VP closure, or a pseudo "muscle moment arm", for this biomechanical system. For a muscle's contribution to posterior velum displacement, we defined mechanical advantage for closure as the derivative of fiber length with respect to velum displacement toward closure. Secondly, we

quantified the change in closure force per change in muscle activation to probe how muscle activation affects closure force. In our modeling framework, this quantity can be calculated for various muscle activation states to investigate how the effect of muscle activation on closure force differs between levels of velar elevation and LVP (or other muscle) activation. These new metrics provide novel insights into the relative contributions of each muscle to VP closure and, in future modeling work, enable quantification of differences in VP muscles' contributions to closure between healthy and clinical populations.

This 3D finite element modeling framework is also novel in its geometric construction and method of validation. Our 3D geometry was constructed from static MRI data of one healthy adult, rather than average measurements from the literature (87). Because of this, we were able to validate our model with data from subject-specific dynamic MRI, in additional validating against previously published closure force data (114). Our validation method empowered us to estimate muscle activation patterns without electromyography, which is likely difficult to acquire in many relevant clinical populations. Additionally, VP anatomy varies significantly between people, especially in a clinical population, so models based on averages across subjects are likely unrepresentative of most, or any, subjects. This dissertation establishes a novel coupled imaging-modeling framework that can be used to further our understanding of the VP mechanism in healthy and impaired speakers.

5.3 Future Applications

The work in this dissertation lays the groundwork for studies and clinical trials that will provide mechanistic understanding of VP function, as well as patient-specific treatment plans for cleft palate repair and VPD informed by patient anatomy and VP function. In particular, the methods developed in this dissertation empower future comprehensive longitudinal clinical studies combining MRI and computational modeling to improve understanding of the VP structure-function relationship, how this relationship evolves throughout development, and how it differs in the case of a cleft palate anatomy.

One possible study involves collecting MRI data for a cohort of children from infancy until late adolescence or early adulthood. Ideally, we would enroll 100 or more patients born with cleft palate before primary repair and collect anatomical MRI of pre-surgical anatomy. By adapting previously developed MRI protocols (5,190,220), we hope to image these infants without sedation using a feed-and-sleep technique. Based on this MRI data, we would use the framework described in this dissertation to construct computational models of pre-repair anatomies, including the velum, posterior pharyngeal wall, and levator veli palatini (LVP) muscle. Depending on image quality, we will also attempt to include geometric representations of the other musculature in our models. With these models, we plan to perform virtual surgeries and predict the best surgery for a given anatomy. If we include VP muscles in addition to the LVP, even if possible only in a subset of subjects, we will explore how current surgical procedures reorient muscles other than the LVP, a topic of particular interest in the cleft palate research community.

In addition to virtual surgeries, we could partner with an existing Coulter Foundation-funded project to examine the fluid dynamics of feeding in our cohort of children. This project is currently running clinical trials on a novel feeding system for children born with cleft palate, and preliminary data indicates that many children feed more efficiently with this novel system (212). With the anatomical data provided by MRI, we could model different feeding systems in children with cleft palate and compare between systems to predict which system would provide the most efficient feeding for each patient. These predictions would then be validated against feeding evaluations performed by speech-language pathologists and parent/guardian feedback. We could then use our models to probe how differences in pre-surgical cleft palate anatomy influence the efficacy of different feeding systems

Approximately three months after each patient's palate repair, we will acquire anatomical MRI of post-repair anatomy and use this data as the geometric basis for a new set of computational models. In particular, we want to simulate VP function and compare this patient-specific model's predictions of VP function with the subject's virtual surgery models' predictions from above. A critical component of this study is collaboration with the plastic surgeon(s) performing palate repairs on our cohort of children. For completeness, we would want detailed notes of the type of surgery performed, and if possible, to observe the primary repairs of each patient in our cohort. This would empower comparison between our virtual surgery model predictions and our post-repair model predictions.

For each patient in our cohort, we plan to collect yearly anatomical MRIs, and starting at age 4, we will also collect dynamic MRIs during speech and swallowing. These dynamic data will be used as subject-specific model validation, as described in this dissertation, in addition to

speech-language pathologist (SLP) evaluations of speech. Each new set of MRI data will be used to construct subject-specific models that represent current VP function, and using growth curves derived from existing cross-sectional data, we will also predict future speech outcomes. This longitudinal MRI data will also serve as the basis for development of growth curves for velopharyngeal structures, e.g. velopharyngeal port dimensions and velum length, in repaired cleft palate anatomies.

When image quality allows, we plan to add additional structures to our model geometry, including the lateral walls, superior larynx, and simplified tongue geometry. This facilitates examination of different closure patterns, as well as quantification of the contributions of lateral wall contraction on VP closure. The primary role of the palatopharyngeus muscle is likely during swallowing to elevate the larynx in conjunction with slight velum lowering. With these additional structures represented, we could simulate swallowing in addition to velum elevation. Investigation of these other VP functions with our models is critical to providing surgeons with more information about how different surgical techniques affect function of the entire VP system, not just VP port closure.

We intend to collect MRI data and complete SLP speech evaluations yearly until each patient is approximately 18 years old. Given that 25-35% of patients with repaired cleft palate have VPD (136), we expect that approximately 25 of our recruited patients will require additional surgical intervention to achieve healthy speech. For these patients, we hope to work closely with clinicians and use our patient-specific models to predict the anatomical factor(s) leading to speech dysfunction and simulate various VPD surgical repairs, e.g. pharyngeal flap and sphincter pharyngoplasty. In particular, for this investigation, our models should include

more detailed and comprehensive geometry than the models described in this dissertation, as mentioned above. For instance, the contributions of the lateral walls are critical when evaluating the efficacy of a pharyngeal flap, and the effect of sphincter pharyngoplasty on swallowing should be explored before surgical intervention. In this cohort of patients with VPD, we will continue collecting anatomical MRI and dynamic MRI during speech production to empower construction of additional models. Predictions from these post-secondary repair models will be compared to predictions from the virtual surgeries using the pre-secondary repair model. Similar to the primary repair surgical data, we will record detailed notes on the surgical procedure to facilitate comparison between pre- and post-surgical model predictions.

An additional component to this study is the collection of yearly MRI data for a group of typically developing (TD) children from infancy to early adulthood. We hope to match the sexes and races of our TD cohort to our patient cohort to control for these effects when comparing between groups. Longitudinal collection of MRI data, both static and dynamic during speech, from TD children empowers comparison of VP structure growth curves between healthy children and those born with cleft palate. In addition, we plan to model VP function in our TD cohort and, similar to the repaired cleft patients, use existing cross-sectional data to predict how VP structures and function will change throughout development. These predictions will then be validated with subject-specific measurements from MRI at later ages.

This longitudinal study would provide an enormous database of anatomical and functional data across development. It would empower investigation of how VP structures grow in both TD and repaired cleft children and would provide critical insight into how the relationships between VP structures, e.g. VP ratio, change throughout development. From this

data, we could establish growth curves for healthy children and those born with cleft palate, and determine the optimal time to evaluate repaired cleft palate patients and determine the need for further surgical intervention. The modeling component to this study would provide key insights into the effect of various surgical techniques on future speech outcomes and supports the existing hypothesis that patient-specific surgical techniques informed by patient anatomy lead to improved speech outcomes. Overall, this study builds on the work described in this dissertation and would establish a physics-based, imaging-informed paradigm for treating cleft palate and VPD with improved outcomes for all those affected by cleft palate.

Although this proposed trial is unfeasible due to funding, timing, and other constraints, this dissertation lays the foundation for many feasible future directions. These involve novel imaging techniques and computational modeling based on the work described in this dissertation that would provide new insights into the VP structure-function relationship for healthy and altered anatomies.

Modeling of Individuals with Repaired Cleft Palate or Velopharyngeal Dysfunction

An immediate application of our coupled imaging-computational modeling framework is development of MRI-based models of individuals with repaired cleft palate and/or VPD. Collaboration with a speech pathology team experienced in child-friendly MRI provides an avenue for recruitment and imaging of children with repaired cleft palate using a child-friendly protocol (100,101,170). Our finite element models could probe the anatomical features, such as LVP or velum length, or mechanical parameters, such as velum stiffness, contributing to dysfunctional VP mechanics and predict which treatments could provide the optimal functional outcomes. The ideal age range for this type of study is between four and nine-years-old; within

this range, children with repaired cleft palate are evaluated to determine the need for secondary surgery.

We demonstrated the ability of our imaging-modeling framework to represent dysfunctional speech mechanics in a preliminary model of an adult with VPD (161). Using the model construction framework described in Chapter 4, we created a three-dimensional geometry including the velum, levator veli palatini, and posterior pharyngeal wall. We included both sides of the VP mechanism due to obvious asymmetries in the subject's anatomy. Our model replicated both mid-sagittal and oblique-coronal plane velum motion captured during speech with dynamic MRI (Figure 5.2). This framework empowers investigation into the causes of VPD and subject-specific treatments and facilitates quantification of how the contributions of each VP muscle to closure differ between healthy and VPD anatomies.

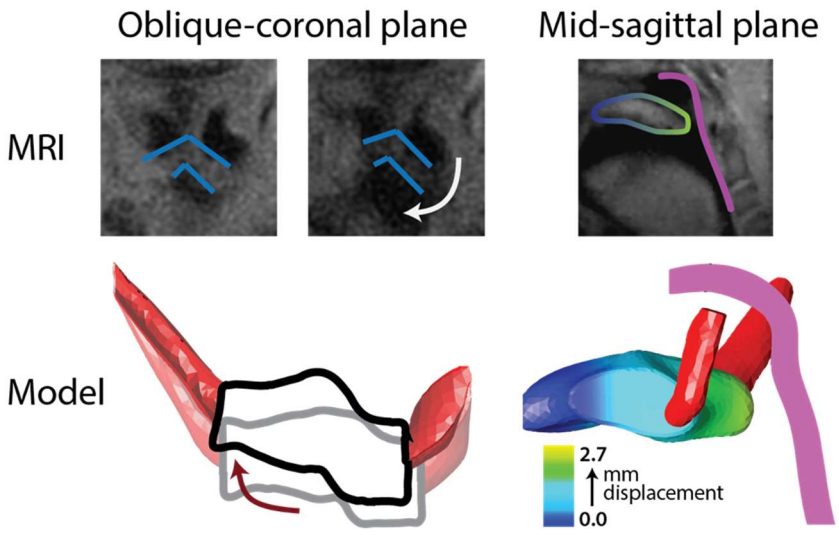

Figure 5.2 Preliminary VPD finite element model
A preliminary finite element model based on an adult with VPD reproduced velum elevations and oblique-coronal motion demonstrated in the subject's dynamic MRI.

Longitudinal Study

Cross-sectional studies have demonstrated that VP structures differ between ages (166), but how a given anatomy changes over time is unknown. Additionally, our understanding of how these structural changes affect function is limited, as the few VP functional studies in children do not relate observed function to structure (100,170,210,211). Our imaging-modeling framework lays the groundwork for a longitudinal study to elucidate changes in VP structure and function through development in both typically developing children and those born with cleft palate. VP muscles demonstrate a gender effect in adults (171), but this is not the case in prepubertal children (101), indicating that structural changes occur between child- and adulthood. When those changes take place and how that differs between individuals is unknown. With a longitudinal study, we could answer questions such as: How do child anatomy and function relate to adult anatomy and function? Does VP closure remain consistent through growth? How does the timing of growth differ in children born with cleft palate? In the repaired cleft palate population, decisions regarding the need for secondary surgery are made during a time of possible tremendous anatomical and functional change. This longitudinal study would provide insight into these questions and lead to more optimized timing and type of VPD surgical treatment accounting for the effects of growth.

Anatomically-based surgical plan

Our ultimate goal is to improve the outcomes of cleft palate repair surgery and eliminate the need for secondary surgeries by providing a physics-based framework to optimize repair surgery for each patient. Cleft palate is one of the most common birth defects in the United States, affecting 1 in 1000 births (159). Children born with cleft palate have repair

surgery typically between six and twelve months old, and the type of repair depends on surgeon preference. Currently, approximately 25% of patients with repaired cleft palate must undergo additional surgery to achieve adequate VP function (137). This high failure rate is due in part to the trial-and-error approach to surgical repair, instead of a mechanistic approach examining how pre-surgical structure will affect post-repair VP muscle function. Our framework could demonstrate the utility of considering patient-specific anatomy when devising surgical plans. With pre-surgical imaging and our computational modeling, various surgical techniques could be simulated and effects compared to predict the surgical technique leading to the optimal outcome. Results from these investigations would provide much needed insight into which surgical procedures are best suited for a given cleft palate anatomy. We hope that this would lead to a paradigm where subject anatomy is a primary consideration in surgical plans and outcomes are improved for all children born with cleft palate.

Novel Imaging Techniques to Improve our Finite Element Models

To our knowledge, our MRI-modeling framework is the first to use subject-specific MRI to construct the model and validate with novel analyses based on subject dynamic MRI. However, with any model, we make certain assumptions for computational efficiency or lack of experimental data. Three assumptions – fiber direction, velum stiffness, and starting sarcomere length – could be investigated with the advancement of additional imaging techniques.

In vivo fiber directions are critical to validate fiber directions used in our finite element modeling framework, which are determined by flow simulations (71,85). Diffusion Tensor Imaging (DTI) provides an *in vivo* evaluation of muscle fiber direction (46,75) and has been suggested as a possible solution to elucidate unknown LVP fiber directions in individuals with

VPD (97,167). DTI has been successfully implemented in skeletal muscle, including the human tongue (64,192). However, most of the VP muscular structures are especially small, so the voxel sizes used in the tongue studies are likely too large for effective evaluation of intravelar muscle fiber directions. Additionally, because the tongue is located more externally, surface coils placed on the cheek improved the signal-to-noise ratio in a tongue DTI study (64). The velum is less accessible, and thus, an intraoral coil is most likely the best option for sufficient signal. Even minimal motion of the relevant structures during acquisition can obscure measured diffusion (148), so immobilization of the structures is typically implemented for effective imaging (64,76,154). The velum moves during breathing and swallowing, so scan time must be minimized to limit this movement or techniques developed to compensate for this motion.

In our framework, we assume a velum stiffness based on the range of literature values and best representation of velum deformation. However, when extending our framework to children with repaired cleft palate, we will need to carefully consider velum stiffness. The effect of scar tissue pattern and stiffness on velar stretch and VP closure warrants exploration. Reported values of velum stiffness are from adults with no history of velopharyngeal surgery, and scar tissue likely alters velum stiffness in children with repaired cleft palate. Magnetic Resonance Elastography (MRE) allows for *in vivo* measurement of soft tissue viscoelastic properties by propagating mechanical shear waves through the tissue and capturing the tissue's response using MRI (135,149). MRE has been successfully utilized in the velum for a small cohort of healthy individuals and patients with obstructive sleep apnea (29,35), and the shear moduli compared favorably to the range of shear moduli determined using other methods (22,23,69,134). MRE of the velum is subject to many of the same drawbacks as DTI. Motion

artifacts are detrimental to accurate determination of shear moduli, as they are calculated from small displacements in the tissue of interest induced by the shear wave. The current method to induce shear waves into the velum, a vibrating mouth guard or bite bar, increases saliva production and increases the desire to swallow, during which the velum moves. One study mitigated this effect by using an oral appliance connected to a vacuum hose that extracted saliva during DTI acquisition of the tongue in two healthy adults (192). More investigation is required to determine what protocol adaptations are necessary for children to successfully complete these scans and to mitigate possible motion effects.

Finally, a critical assumption across this dissertation is that resting length of VP muscles, in particular the LVP, corresponds to optimal fiber length and is at the peak of the force-length curve. Resting sarcomere lengths are currently unknown in these muscles. Recently, the zebrascope, a new device leveraging laser-scanning second harmonic generation to image sarcomeres, was developed and made commercially available (186,229). The zebrascope's utility has been demonstrated in a variety of limb muscles using a needle-size probe inserted into the muscle of interest (33,34,122,186,219). Use of the insertion probe is unlikely to be feasible for the LVP or other VP muscles. However, this system also employs a flat probe that can rest on the surface of exposed muscle and image sarcomeres. This surface probe could be utilized during cleft palate repair surgeries when the LVP is exposed to image sarcomeres in the LVP. This would lead to experimental testing of our assumption that LVP resting length corresponds to optimal length. Further protocol development is required to accelerate device set-up and image collection to minimize disruption during repair surgery.

Inclusion of Lateral Pharyngeal Walls in Finite Element Models

Although elevation of the velum is the primary driver in VP port closure, the lateral pharyngeal walls can contribute to complete closure of the VP port (90,163). Our simulations model a coronal closure pattern, reported in 51 to 55% of healthy individuals (40,58), but there are three other closure patterns that involve varying degrees of lateral wall contraction. Lateral wall motion could be especially important in children with repaired cleft palate who have limited velum mobility. These children are prime candidates for pharyngeal flap surgery to treat their VPD; the flap compensates for minimal velum movement but depends on lateral wall contraction for sufficient closure. Additionally, the superior constrictor, which lies beneath a layer of mucosa in the lateral and posterior pharyngeal walls, has been shown to activate during speech production (107). A better mechanistic understanding of lateral wall contraction and closure patterns could provide additional insight into the VP structure-function relationship and how it varies between individuals. Men were found more likely to demonstrate coronal closure, although this difference could be due to the greater velar lengths in men, which corresponded to coronal closure patterns (90). Our computational modeling framework could further explore this hypothesis in addition to probing the anatomical or mechanical factors that influence type of closure pattern.

Additionally, inclusion of the lateral pharyngeal walls empowers investigation of upper airway collapse in obstructive sleep apnea (OSA), which affects an estimated 20% of adults in the U.S. (57). Although obesity is associated with OSA, how weight gain affects the tissues and mechanics of the upper airway is unknown (29). Additionally, OSA is not only a concern for individuals with high body mass index but also for other populations, including individuals with

pharyngeal flaps to address VPD (37). Though Continuous Positive Airway Pressure (CPAP) mitigates OSA in most patients, approximately 30% of people do not tolerate it (157), and other treatments are effective in approximately 50% of people (140). Upper airway collapse in OSA has been modeled previously but not with geometric representation of the velar musculature involved (126–128). Our framework could probe how changes in mechanical and anatomic factors contribute to OSA in specific patients to better inform treatment options.

5.4 Final Remarks

Blowing out candles, sucking a straw, speaking easily and intelligibly – These normal tasks can be exceptionally challenging for individuals with velopharyngeal dysfunction (VPD). Decades of primarily observational work generated an extensive database of knowledge and led to developments in cleft palate repair surgical techniques and improved treatments for VPD. Currently, however, 25% of cleft palate repairs require secondary surgical treatment, and VPD is not easily treated in many complex clinical populations like 22q11.2 DS. Our understanding of the complex relationship between VP structure and *in vivo* function remains limited. In this dissertation, I endeavored to develop methods to empower this investigation. Because the levator veli palatini is the primary muscle of VP closure, knowledge of *in vivo* LVP function is critical to our understanding of VP function. No method to measure *in vivo* LVP function existed, so I developed a method to measure LVP lengths and velocities during speech production using dynamic MRI. We used this method to reveal that LVP shortening and contraction velocity scale with VP port depth. Moving forward, this method will enable investigation of additional relationships between VP structure and *in vivo* LVP function. In healthy and clinical populations. In the 22q11.2 DS population, the relationship between

anatomy and function is likely more complex than in healthy individuals, so I adapted an existing computational model to explore this relationship. Simulations revealed that LVP cross-sectional area most disadvantaged closure in all 22q11.2 DS anatomies, even those from children with normal resonance. However, no other anatomical measure was consistently disadvantageous for VP closure across all anatomies, signifying the need for anatomy-informed, rather than "one size fits all", treatments of VPD in children with 22q11.2 DS. Finally, our ability to prevent and treat VPD remains limited because the contributions of each VP muscle to closure are unknown. Using a novel imaging-finite element modeling framework, I systematically probed the roles of two VP muscles – the palatopharyngeus and palatoglossus – in VP closure, quantified the effects of each muscle on closure force and posterior velum displacement, and related these effects to contributions of the LVP and musculus uvulae.

Recent advances in MRI have enabled collection of massive amounts of *in vivo* data and accelerated our knowledge of VP anatomy and function. When combined with computational modeling, MRI has the potential to forever change our approach to cleft palate repair and treatment of VPD. The framework developed in this dissertation integrates the wealth of literature with MRI-based anatomy and validation to provide new insights into VP biomechanics. Coupling imaging and computational modeling empowers us to unravel the complexities of the VP structure-function relationship and improve the lives of children born with cleft palate and those living with VPD.

References

1. Abe M, Murakami G, Noguchi M, Kitamura S, Shimada K, Kohama G-I. Variations in the tensor veli palatini muscle with special reference to its origin and insertion. The Cleft Palate-Craniofacial Journal. 2004;41(5):474–84.
2. Akgüner M. Velopharyngeal Anthropometric Analysis with MRI in Normal Subjects. Annals of plastic surgery. 1999;43(2):142–147.
3. Akgüner M, Karaca C, Barutçu A, Özaksoy D, Yurt A, Vayvada H. Evaluation of velopharyngeal pathophysiology and velopharyngeal insufficiency with magnetic resonance imaging. European Journal of Plastic Surgery. 1998;21(3):118–128.
4. Andreassen ML, Smith BE, Guyette TW. Pressure-Flow Measurements for Selected Oral and Nasal Sound Segments Produced by Normal Adults. Cleft Palate Journal. 1991;28(4):398–407.
5. Antonov NK, Ruzal-Shapiro CB, Morel KD, Millar WS, Kashyap S, Lauren CT, Garzon MC. Feed and Wrap MRI Technique in Infants. Clinical Pediatrics. 2017;56(12):1095–1103.
6. Atik B, Bekerecioglu M, Tan O, Etlik O, Davran R, Arslan H. Evaluation of Dynamic Magnetic Resonance Imaging in Assessing Velopharyngeal Insufficiency During Phonation. The Journal of Craniofacial Surgery. 2008;19(3):566–572.
7. Autodesk Inc., San Rafael, California, USA.
8. Azzam NA, Kuehn DP. The morphology of musculus uvulae. The Cleft Palate Journal. 1977;14(1):78–87.
9. Bae Y, Kuehn DP, Conway CA, Sutton BP. Real-time magnetic resonance imaging of velopharyngeal activities with simultaneous speech recordings. The Cleft Palate-Craniofacial Journal. 2011;48(6):695–707.
10. Bae Y, Kuehn DP, Conway CA, Sutton BP, Perry JL. Three-Dimensional Magnetic Resonance Imaging of Velopharyngeal Structures. Journal of Speech, Language, and Hearing Research. 2011;54(December):1538–1546.
11. Bae Y, Pfeil G. Structural Changes Following Velopharyngeal Resistance Training (Continuous Positive Airway Pressure Therapy): A Preliminary Report. The Cleft Palate-Craniofacial Journal. 2018;55(9):1321–1328.
12. Bahler AS, Fales JT, Zierler KL. The Dynamic Properties of Mammalian Skeletal Muscle. The Journal of General Physiology. 1968;51(3):369–384.
13. Barsoumian R, Kuehn DP, Moon JB, Canady JW. An Anatomic Study of the Tensor Veli Palatini and Dilatator Tubae Muscles in Relation to Eustachian Tube and Velar Function. The Cleft Palate-Craniofacial Journal. 1998;35(2):101–10.
14. Basmajian J V., Dutta CR. Electromyography of the pharyngeal constrictors and levator palati in man. The Anatomical Record. 1961;139(4):561–563.
15. Bassett AS, McDonald-McGinn DM, Devriendt K, Digilio MC, Goldenberg P, Habel A, Marino B, Oskarsdottir S, Philip N, Sullivan K, et al. Practical guidelines for managing patients with 22q11.2 deletion syndrome. Journal of Pediatrics. 2011;159(2):332–339.e1.
16. Basta MN, Silvestre J, Stransky CA, Solot C, Cohen M, McDonald-McGinn D, Zackai EH, Kirschner R, Low DW, Randall P, et al. A 35-Year Experience With Syndromic Cleft Palate Repair: Operative Outcomes and Long-term Speech Function. Annals of plastic surgery. 2014;73 Suppl 2(December):S130-5.

17. Baylis AL, Munson B, Moller KT. Factors affecting articulation skills in children with velocardiofacial syndrome and children with cleft palate or velopharyngeal dysfunction: A preliminary report. Cleft Palate-Craniofacial Journal. 2008;45(2):193–207.

18. Baylis AL, Watson PJ, Moller KT. Structural and functional causes of hypernasality in velocardiofacial syndrome. Folia Phoniatrica et Logopaedica. 2009;61(2):93–96.

19. Beer AJ, Hellerhoff P, Zimmermann A, Mady K, Sader R, Rummeny EJ, Hannig C. Dynamic near-real-time magnetic resonance imaging for analyzing the velopharyngeal closure in comparison with videofluoroscopy. Journal of Magnetic Resonance Imaging. 2004;20(5):791–7.

20. Bell-berti F. An Electromyographic Study of Velopharyngeal Function in Speech. Journal of Speech and Hearing Research. 1976;19:225–240.

21. Bell-berti F, Baer T, Harris KS, Niimi S. Coarticulatory Effects of Vowel Quality on Velar Function. Phonetica. 1979;36(3):187–193.

22. Berry DA, Moon JB, Kuehn DP. A Finite Element Model of the Soft Palate. The Cleft Palate-Craniofacial Journal. 1999;36(3):217–223.

23. Birch MJ, Srodon PD. Biomechanical Properties of the Human Soft Palate. The Cleft Palate-Craniofacial Journal. 2009;46(3):268–274.

24. Blemker SS, Pinsky PM, Delp SL. A 3D model of muscle reveals the causes of nonuniform strains in the biceps brachii. Journal of Biomechanics. 2005;38(4):657–665.

25. Boorman JG, Sommerlad BC. Levator palati and palatal dimples: their anatomy, relationship and clinical significance. British journal of plastic surgery. 1985;38(3):326–332.

26. Boorman JG, Sommerlad BC. Musculus uvulae and levator palati: their anatomical and functional relationship in velopharyngeal closure. British Journal of Plastic Surgery. 1985;38:333–338.

27. Brandão GR, De Souza Freitas JA, Genaro KF, Yamashita RP, Fukushiro AP, Lauris JRP. Speech outcomes and velopharyngeal function after surgical treatment of velopharyngeal insufficiency in individuals with signs of velocardiofacial syndrome. Journal of Craniofacial Surgery. 2011;22(5):1736–1742.

28. Brennan SF, Cresswell AG, Farris DJ, Lichtwark GA. The effect of cadence on the muscle-tendon mechanics of the gastrocnemius muscle during walking. Scandinavian Journal of Medicine & Science in Sports. 2017;27(3):289–298.

29. Brown EC, Cheng S, Mckenzie DK, Butler JE, Gandevia SC, Bilston LE. Tongue Stiffness is Lower in Patients with Obstructive Sleep Apnea during Wakefulness Compared with Matched Control Subjects. Sleep. 2015;38(4):537.

30. Cahill LM, Turner AB, Stabler P a., Addis PE, Theodoros DG, Murdoch BE. An Evaluation of Continuous Positive Airway Pressure (CPAP) Therapy in the Treatment of Hypernasality Following Traumatic Brain Injury. Journal of Head Trauma Rehabilitation. 2004;19(3):241–253.

31. Chegar BE, Tatum SA, Marrinan E, Shprintzen RJ. Upper airway asymmetry in velo-cardio-facial syndrome. International Journal of Pediatric Otorhinolaryngology. 2006;70(8):1375–1381.

32. Chen PK., Wu JT, Chen YR, Noordhoff M. Correction of secondary velopharyngeal insufficiency in cleft palate patients with the Furlow palatoplasty. Plastic and reconstructive surgery. 1994;94(7):933–941.

33. Chen X, Delp SL. Human soleus sarcomere lengths measured using in vivo microendoscopy at two ankle flexion angles. Journal of biomechanics. 2016;49(16):4164–4167.

34. Chen X, Sanchez GN, Schnitzer MJ, Delp SL. Changes in sarcomere lengths of the human vastus lateralis muscle with knee flexion measured using in vivo microendoscopy. Journal of Biomechanics. 2016;49(13):2989–2994.

35. Cheng S, Gandevia SC, Green MA, Sinkus R, Bilston LE. Viscoelastic properties of the tongue and soft palate using MR elastography. Journal of Biomechanics. 2011;44(3):450–4.

36. Close RI. Dynamic Properties of Mammalian Skeletal Muscles. Physiological Reviews. 1972;52(1):129–197.

37. Computational Simulation Software, LLC, American Fork, Utah, USA.

38. Cooper DS, Folkins JW. Comparison of electromyographic signals from different electrode placements in the palatoglossus muscle. The Journal of the Acoustical Society of America. 1985;78(5):1530–40.

39. Criscione JC, Douglas AS, Hunter WC. Physically based strain invariant set for materials exhibiting transversely isotropic behavior. Journal of the Mechanics and Physics of Solids. 2001;49(4):871–897.

40. Croft CB, Shprintzen RJ, Rakoff SJ. Patterns of Velopharyngeal Valving in Normal and Cleft Palate Subjects: A Multi-View Videofluoroscopic and Nasendoscopic Study. The Laryngoscope. 1981;91(2):265–271.

41. Cronin NJ, Lichtwark G. The use of ultrasound to study muscle-tendon function in human posture and locomotion. Gait & Posture. 2013;37:305–312.

42. Cutting CB, Rosenbaum J, Rovati L. The technique of muscle repair in the cleft soft palate. Operative Techniques in Plastic and Reconstructive Surgery. 1995;2(4):215–222.

43. D'Antonio LL, Davio M, Zoller K, Punjabi A, Harde. Results of Furlow Z-Plasty in Patients with Velocardiofacial Syndrome. Plastic and Reconstructive Surgery. 2001;107(4):1077–1079.

44. D'Antonio LL, Eichenberg BJ, Zimmerman GJ, Patel S, Riski JE, Herber SC, Hardesty RA. Radiographic and aerodynamic measures of velopharyngeal anatomy and function following Furlow Z-plasty. Plastic and reconstructive surgery. 2000;106(3):539–549.

45. Dalben GDS, Richieri-Costa A, Taveira LADA. Craniofacial morphology in patients with velocardiofacial syndrome. Cleft Palate-Craniofacial Journal. 2010;47(3):241–246.

46. Van Donkelaar CC, Kretzers LJG, Bovendeerd PHM, Lataster LMA, Nicolay K, Janssen JD, Drost MR. Diffusion tensor imaging in biomechanical studies of skeletal muscle function. Journal of Anatomy. 1999;194(Pt 1):79–88.

47. Dorrance GM. Lengthening the Soft Palate in Cleft Palate Operations. Annals of Surgery. 1925;82(2):208.

48. Doucet J-C, Herlin C, Captier G, Baylon H, Verdeil M, Bigorre M. Speech outcomes of early palatal repair with or without intravelar veloplasty in children with complete unilateral cleft lip and palate. The British journal of oral & maxillofacial surgery. 2013;51(8):845–50.

49. Doyle WJ, Casselbrandt JD, Swarts JD, Bluestone CD. Observations on a role for the tensor veli palatini muscle in intrinsic palatal function. The Cleft palate journal. 1990;27(3):317–18.

50. Drissi C, Mitrofanoff M, Talandier C, Falip C, Le Couls V, Adamsbaum C. Feasibility of dynamic MRI for evaluating velopharyngeal insufficiency in children. European Radiology. 2011;21(7):1462–9.

51. Edman KAP. The Relation Between Sarcomere Length and Active Tension in Isolated Semintendinosus Fibres of the Frog. The Journal of Physiology. 1966;183:407–417.

52. Engelke W, Bruns T, Striebeck M, Hoch G. Midsagittal Velar Kinematics during Production of VCV sequences. The Cleft Palate-Craniofacial Journal. 1996;33(3):236–244.

53. Ettema SL, Kuehn DP. A Quantitative Histologic Study of the Normal Human Adult Soft Palate. Journal of Speech and Hearing Research. 1994;37(April 1994):303–313.

54. Ettema SL, Kuehn DP, Perlman AL, Alperin N. Magnetic resonance imaging of the levator veli palatini muscle during speech. The Cleft Palate-Craniofacial Journal. 2002;39(2):130–44.

55. Feng X, Blemker SS, Inouye J, Pelland CM, Zhao L, Meyer CH. Assessment of velopharyngeal function with dual-planar high-resolution real-time spiral dynamic MRI. Magnetic Resonance in Medicine. 2018;80(4):1467–1474.

56. Filip C, Impieri D, Aagenæs I, Breugem CC, Høgevold HE, Særvold T, Aukner R, Lima K, Tønseth K, Abrahamsen TG. Adults with 22q11.2 deletion syndrome have a different velopharyngeal anatomy with predisposition to velopharyngeal insufficiency. Journal of Plastic, Reconstructive and Aesthetic Surgery. 2018;71(4):524–536.

57. Finkel KJ, Searleman AC, Tymkew H, Tanaka CY, Saager L, Safer-Zadeh E, Bottros M, Selvidge JA, Jacobsohn E, Pulley D, et al. Prevalence of undiagnosed obstructive sleep apnea among adult surgical patients in an academic medical center. Sleep Medicine. 2009;10(7):753–758.

58. Finkelstein Y, Shapiro-Feinberg M, Talmi YP, Nachmani A, DeRowe A, Ophir D. Axial configuration of the velopharyngeal valve and its valving mechanism. Cleft Palate-Craniofacial Journal. 1995;32(4):299–305.

59. Finkelstein Y, Talmi YP, Nachmani A, Hauben DJ, Zohar Y. On the variability of velopharyngeal valve anatomy and function: a combined peroral and nasendoscopic study. Plastic and reconstructive surgery. 1992;89(4):631–639.

60. Fu M, Barlaz MS, Holtrop JL, Perry JL, Kuehn DP, Shosted RK, Liang ZP, Sutton BP. High-frame-rate full-vocal-tract 3D dynamic speech imaging. Magnetic Resonance in Medicine. 2017;77(4):1619–1629.

61. Fu M, Zhao B, Carignan C, Shosted RK, Perry JL, Kuehn DP, Liang Z-P, Sutton BP. High-resolution dynamic speech imaging with joint low-rank and sparsity constraints. Magnetic Resonance in Medicine. 2015;73(5):1820–1832.

62. Fukino K, Tsutsumi M, Sanudo J, Ono T, Akita K. Anatomical Significance of the Spatial Distribution of the Palatopharyngeus With Regard to Velopharyngeal Closure. The Cleft Palate-Craniofacial Journal. 2018:105566561881308.

63. Furlow LT. Discussion: Radiographic and aerodynamic measures of velopharyngeal anatomy and function following Furlow Z-plasty. Plast Reconstr Surg. 2000;106(3):550–553.

64. Gaige TA, Benner T, Wang R, Wedeen VJ, Gilbert RJ. Three dimensional myoarchitecture of the human tongue determined in vivo by diffusion tensor imaging with tractography. Journal of Magnetic Resonance Imaging. 2007;26(3):654–661.

65. George TN, Kotlarek KJ, Kuehn DP, Sutton BP, Perry JL. Differences in the Tensor Veli Palatini Between Adults With and Without Cleft Palate Using High-Resolution 3-Dimensional Magnetic Resonance Imaging. The Cleft Palate-Craniofacial Journal. 2018:105566561775280.

66. Gordon AM, Huxley AF, Julian FJ. The variation in isometric tension with sarcomere length in vertebrate muscle fibres. The Journal of Physiology. 1966;184(May):170–192.

67. Ha S. The Levator Veli Palatini Muscle in Cleft Palate Anatomy and Its Implications for Assessing Velopharyngeal Function : A Literature Review. Korean Journal of Communication Disorders. 2007;12:77–89.

68. Ha S, Kuehn DP, Cohen M, Alperin N. Magnetic resonance imaging of the levator veli palatini muscle in speakers with repaired cleft palate. The Cleft Palate-Craniofacial Journal. 2007;44(5):494–505.

69. Haddad SMH, Dhaliwal SS, Rotenberg BW, Samani A, Ladak HM. Estimation of the Young's moduli of fresh human oropharyngeal soft tissues using indentation testing. Journal of the Mechanical Behavior of Biomedical Materials. 2018;86(July):352–358.

70. Hairston LE, Sauerland EK. Electromyography of the human palate: discharge patterns of the levator and tensor veli palatini. Electromyography and clinical neurophysiology. 1981;21(2–3):287–297.

71. Handsfield GG, Bolsterlee B, Inouye JM, Herbert RD, Besier TF, Fernandez JW. Determining skeletal muscle architecture with Laplacian simulations: a comparison with diffusion tensor imaging. Biomechanics and Modeling in Mechanobiology. 2017:1–11.

72. Handsfield GG, Inouye JM, Slane LC, Thelen DG, Miller GW, Blemker SS. A 3D model of the Achilles tendon to determine the mechanisms underlying nonuniform tendon displacements. Journal of Biomechanics. 2017;51:17–25.

73. Hanes MC, Weinzweig J, Kuzon WM, Panter KE, Buchman SR, Faulkner JA, Yu D, Cederna PS, Larkin LM. Contractile properties of single permeabilized muscle fibers from congenital cleft palates and normal palates of Spanish goats. Plastic and reconstructive surgery. 2007;119(6):1685–94.

74. Hanes MC, Weinzweig J, Panter KE, McClellan WT, Caterson SA, Buchman SR, Faulkner JA, Yu D, Cederna PS, Larkin LM. The effect of cleft palate repair on contractile properties of single permeabilized muscle fibers from congenitally cleft goat palates. Annals of Plastic Surgery. 2008;60(2):188–193.

75. Heemskerk AM, Damon BM. Diffusion Tensor MRI Assessment of Skeletal Muscle Architecture. Current Medical Imaging Reviews. 2007;3(3):152–160.

76. Heemskerk AM, Strijkers GJ, Vilanova A, Drost MR, Nicolay K. Determination of mouse skeletal muscle architecture using three-dimensional diffusion tensor imaging. Magnetic Resonance in Medicine. 2005;53(6):1333–1340.

77. Heliövaara A, Hurmerinta K. Craniofacial Cephalometric Morphology in Children with CATCH 22 Syndrome. Orthodontics and Craniofacial Research. 2006;9(4):186–192.

78. Hill A V. The Heat of Shortening and the Dynamic Constants of Muscle. Proceedings of the Royal Society B: Biological Sciences. 1938;126(843):136–195.

79. Hoit JD, Watson PJ, Hixon KE, McMahon P, Johnson CL. Age and velopharyngeal function during speech production. Journal of Speech & Hearing Research. 1994;37(2):295–302.

80. Honjo I, Okazaki N, Nozoe T, Hamasaki H. Role of the Tensor Veli Palatini Muscle in Movement of the Soft Palate. Acta Oto-Laryngologica. 1979;88(1–6):137–141.

81. Hoopes JE, Dellon AL, Fabrikant JI, Edgerton MT, Soliman AH. Cineradiographic Definition of the Functional Anatomy and Pathophysiology of the Velopharynx. The Cleft Palate Journal. 1970;7(2):443–454.

82. Huang MHS, Lee ST, Rajendran K. Anatomic Basis of Cleft Palate and Velopharyngeal Surgery: Implications from a Fresh Cadaveric Study. Plastic and reconstructive surgery. 1998;101(3):613–627.

83. Huang MHS, Lee ST, Rajendran K. Structure of the Musculus Uvulae: Functional and Surgical Implications of an Anatomic Study. The Cleft Palate-Craniofacial Journal. 1997;34(6).

84. Huxley HE. The Double Array of Filaments in Cross-Striated Muscle. The Journal of Biophysical and Biochemical Cytology. 1957;3(5):631–48.

85. Inouye J, Handsfield G, Blemker S. Fiber Tractography for Finite-Element Modeling of Transversely Isotropic Biological Tissues of Arbitrary Shape Using Computational Fluid Dynamics. Simulation Series. 2015;47(10):184–189.

86. Inouye JM, Lin KY, Perry JL, Blemker SS. Contributions of the Musculus Uvulae to Velopharyngeal Closure Quantified With a 3-Dimensional Multimuscle Computational Model. Annals of Plastic Surgery. 2016;77(August):70–75.

87. Inouye JM, Pelland CM, Lin KY, Borowitz KC, Blemker SS. A Computational Model of Velopharyngeal Closure for Simulating Cleft Palate Repair. The Journal of Craniofacial Surgery. 2015;26(3):658–662.

88. Inouye JM, Perry JL, Lin KY, Blemker SS. A Computational Model Quantifies the Effect of Anatomical Variability on Velopharyngeal Function. Journal of Speech, Language, and Hearing Research. 2015;58:1119–1133.

89. Isberg A, Henningsson G. Influence of Palatal Fistulas on Velopharyngeal Movements: A Cineradiographic Study. Plastic and reconstructive surgery. 1987;79(4):525–530.

90. Jordan HN, Schenck GC, Ellis C, Rangarathnam B, Fang X, Perry JL. Examining Velopharyngeal Closure Patterns Based on Anatomic Variables. Journal of Craniofacial Surgery. 2017;28(1):270–274.

91. Kane AA, Butman JA, Mullick R, Skopec M, Choyke P. A New Method for the Study of Velopharyngeal Function Using Gated Magnetic Resonance Imaging. Plastic and reconstructive surgery. 2002;109(2):472–481.

92. Kao DS, Soltysik DA, Hyde JS, Gosain AK. Magnetic Resonance Imaging as an Aid in the Dynamic Assessment of the Velopharyngeal Mechanism in Children. Plastic and reconstructive surgery. 2008;122(2):572–577.

93. Kaplan EN. Soft Palate Repair by Levator Muscle Reconstruction and a Buccal Mucosal Flap. Plastic and reconstructive surgery. 1975;56(2):129–136.

94. Kim H, Honda K, Maeda S. Stroboscopic-cine MRI study of the phasing between the tongue and the larynx in the Korean three-way phonation contrast. Journal of Phonetics. 2005;33(1):1–26.

95. Kirschner RE. Palatal anomalies and velopharyngeal dysfunction associated with velo-cardio-facial syndrome. In: Velo-Cardio-Facial Syndrome: A Model for Understanding Microdeletion Disorders. 2005. p. 83–104.

96. Kirschner RE, Baylis AL. Surgical considerations in 22Q11.2 deletion syndrome. Clinics in Plastic Surgery. 2014;41(2):271–282.

97. Kollara L. Variations in Craniofacial and Velopharyngeal Structures Among Individuals with 22q11.2 Deletion Syndrome. East Carolina University; 2016.

98. Kollara L, Baylis AL, Kirschner RE, Bates DG, Smith M, Fang X, Perry JL. An Innovative, Non-Sedated MRI Protocol to Assess Velopharyngeal Variations in Children with 22q11.2 Deletion Syndrome. The Cleft Palate-Craniofacial Journal. 2017;54(3):e69-70.

99. Kollara L, Pelland CM, Blemker SS, Perry JL. A Mathematical Model Of Closure Biomechanics Predicts Resonance Ratings Among Children With 22q11. 2 Deletion Syndrome. The Cleft palate-craniofacial journal. 2017.

100. Kollara L, Perry JL. Effects of Gravity on the Velopharyngeal Structures in Children Using Upright Magnetic Resonance Imaging. The Cleft Palate-Craniofacial Journal. 2014;51(6):669–76.

101. Kollara L, Perry JL, Hudson S. Racial Variations in Velopharyngeal and Craniometric Morphology in Children: An Imaging Study. Journal of Speech Language and Hearing Research. 2016;59(1):27–38.

102. Kollara L, Schenck G, Jaskolka M, Perry JL. Examining a New Method to Studying Velopharyngeal Structures in a Child With 22q11.2 Deletion Syndrome. Journal of Speech, Language, and Hearing Research. 2017;60(4):892.

103. Kotlarek KJ, Perry JL, Fang X. Morphology of the Levator Veli Palatini Muscle in Adults With Repaired Cleft Palate. The Journal of craniofacial surgery. 2017;28(3):1.

104. Kuehn DP. A Cineradiographic Investigation of Velar Movement Variables in Two Normals. The Cleft Palate Journal. 1976;13(April):88–103.

105. Kuehn DP. New therapy for treating hypernasal speech using continuous positive airway pressure (CPAP). Plastic and reconstructive surgery. 1991;88(6):959–966.

106. Kuehn DP, Ettema SL, Goldwasser MS, Barkmeier JC. Magnetic resonance imaging of the levator veli palatini muscle before and after primary palatoplasty. The Cleft Palate-Craniofacial Journal. 2004;41(6):584–92.

107. Kuehn DP, Folkins JW, Cutting CB. Relationships Between Muscle Activity and Velar Position. The Cleft Palate Journal. 1982;19(1):25–35.

108. Kuehn DP, Folkins JW, Linville RN. An Electromyographic Study of the Musculus Uvulae. The Cleft Palate Journal. 1988;25(4):348–355.

109. Kuehn DP, Imrey PB, Tomes L, Jones DL, O'Gara MM, Seaver EJ, Smith BE, Van Demark DR, Wachtel JM. Efficacy of continuous positive airway pressure for treatment of hypernasality. The Cleft Palate-Craniofacial Journal. 2002;39(3):267–76.

110. Kuehn DP, Kahane JC. Histologic Study of the Normal Human Adult Soft Palate. The Cleft Palate-Craniofacial Journal. 1990;27(1):26–35.

111. Kuehn DP, Moller KT. Speech and Language Issues in the Cleft Palate Population : The State of the Art. The Cleft Palate-Craniofacial Journal. 2000;37(4):348-1–35.

112. Kuehn DP, Moon JB. Induced Fatigue Effects on Velopharyngeal Closure Force. Journal of Speech, Language, and Hearing Research. 2000;43:486–500.

113. Kuehn DP, Moon JB. Levator Veli Palatini Muscle Activity in Relation to Intraoral Air Pressure Variation. Journal of Speech and Hearing Research. 1994;37(December 1994):1260–1270.

114. Kuehn DP, Moon JB. Velopharyngeal Closure Force and Levator Veli Palatini Activation Levels in Varying Phonetic Contexts. Journal of Speech, Language, and Hearing Research. 1998;41:51–62.

115. Kummer AW. Types and causes of velopharyngeal dysfunction. Seminars in speech and language. 2011;32(2):150–8.

116. Kurtek S, Xie Q, Samir C, Canis M. Statistical model for simulation of deformable elastic endometrial tissue shapes. Neurocomputing. 2016;173:36–41.

117. Lallh AK, Rochet AP. The Effect of Information on Listeners ' Attitudes Toward Speakers with Voice or Resonance Disorders. Journal of Speech, Language, and Hearing Research. 2000;43:782–795.

118. LaRossa D. The State of the Art in Cleft Palate Surgery. The Cleft Palate-Craniofacial Journal. 2000;37(3):225–228.

119. Larsson L, Moss RL. Maximum Velocity of Shortening in Relation to Myosin Isoform Composition in Single Fibres from Human Skeletal Muscles. The Journal of Physiology. 1993;472:595–614.

120. Lewin ML, Heller JC, Kojak DJ. Speech Results after Millard Island Flap Repair In Cleft Palate and Other Velopharyngeal Insufficiencies. Cleft Palate Journal. 1975;12(3):263–269.

121. Lichtwark GA, Bougoulias K, Wilson AM. Muscle fascicle and series elastic element length changes along the length of the human gastrocnemius during walking and running. Journal of Biomechanics. 2007;40(1):157–164.

122. Lichtwark GA, Farris DJ, Chen X, Hodges PW, Delp SL. Microendoscopy reveals positive correlation in multiscale length changes and variable sarcomere lengths across different regions of human muscle. Journal of Applied Physiology. 2018;125(6):1812–1820.

123. Lieber RL. Skeletal muscle structure, function, and plasticity. Lippincott Williams and Wilkins; 2002.

124. Lindman R, Paulin G, Stål PS. Morphological Characterization of the Levator Veli Palatini Muscle in Children Born With Cleft Palates. The Cleft Palate-Craniofacial Journal. 2001;38(5):438–448.

125. Lingala SG, Sutton BP, Miquel ME, Nayak KS. Recommendations for real-time speech MRI. Journal of Magnetic Resonance Imaging. 2016;43(1):28–44.

126. Liu H, Moxness MHS, Prot VE, Skallerud BH. Palatal implant surgery effectiveness in treatment of obstructive sleep apnea: A numerical method with 3D patient-specific geometries. Journal of Biomechanics. 2018;66:86–94.

127. Liu H, Prot VE, Skallerud BH. 3D patient-specific numerical modeling of the soft palate considering adhesion from the tongue. Journal of Biomechanics. 2018;77:107–114.

128. Liu H, Victorien EP, Skallerud BH. Soft palate muscle activation: a modeling approach for improved understanding of obstructive sleep apnea. Biomechanics and Modeling in Mechanobiology. 2018:1–16.

129. Losken A, Williams JK, Burstein FD, Malick DN, Riski JE. Surgical correction of velopharyngeal insufficiency in children with velocardiofacial syndrome. Plastic and Reconstructive Surgery. 2006;117(5):1493–1498.

130. Lubker J, Salinard JB, May K. Palatoglossus Function in Normal Speech Production—Electromyographic Implications. In: The Journal of the Acoustical Society of America. Vol. 53. 1973. p. 296.

131. Lubker JF, Fritzell J, Lindqvist J. Velopharyngeal Function: An Electromyographic Study. Speech Transmission Laboratory Quarterly Progress and Status Report, Royal Institute of Technology, Stockholm. 1970;4:9–20.

132. Luu LA, Zhang S, Pelland CM, Blemker SS. A Comprehensive Meta-Analysis of Skeletal Muscle Architecture in Humans. In: Annaul Meeting of the American Society of Biomechanics. 2015.

133. Maas SA, Ellis BJ, Ateshian GA, Weiss JA. FEBio: Finite Elements for Biomechanics. Journal of Biomechanical Engineering. 2012;134(1):011005.

134. Malhotra A, Huang Y, Fogel RB, Pillar G, Edwards JK, Kikinis R, Loring SH, White DP. The Male Predisposition to Pharyngeal Collapse Importance of Airway Length. American Journal of Respiratory and Critical Care Medicine. 2002;166(10):1388–1395.

135. Manduca A, Oliphant TE, Dresner MA, Mahowald JL, Kruse SA, Amromin E, Felmlee JP, Greenleaf JF, Ehman RL. Magnetic resonance elastography: Non-invasive mapping of tissue elasticity. Medical Image Analysis. 2001;5(4):237–254.

136. McWilliams BJ. The long-term speech results of primary and secondary surgical correction of palatal clefts. Multidisciplinary Management of Cleft Lip and Palate. Philadelphia: WB Saunders. 1990:815–819.

137. McWilliams BJ. The Long-Term Speech Results of Primary and Secondary Surgical Correction of Palatal Clefts. In: Bardach J, Morris HL, editors. Multidisciplinary Management of Cleft Lip and Palate. W.B. Saunders Company; 1990. p. 815–819.

138. McWilliams BJ. Unresolved Issues in Velopharyngeal Valving. Cleft Palate Journal. 1985;22(1):29–33.

139. Mehendale F V., Birch MJ, Birkett L, Sell D, Sommerlad BC. Surgical Management of Velopharyngeal Incompetence in Velocardiofacial Syndrome. Cleft Palate-Craniofacial Journal. 2004;41(2):124–135.

140. Mehta A, Qian J, Petocz P, Darendeliler MA, Cistulli PA. A Randomized, Controlled Study of a Mandibular Advancement Splint for Obstructive Sleep Apnea. American journal of respiratory and critical care medicine. 2001;163(6):1457–1461.

141. Milczuk HA, Smith DS, Brockman JH. Surgical outcomes for velopharyngeal insufficiency in velocardiofacial syndrome and nonsyndromic patients. Cleft Palate-Craniofacial Journal. 2007;44(4):412–417.

142. Moll KL. A Cinefluorographic Study of Velopharyngeal Function in Normals During Various Activities. The Cleft Palate Journal. 1965;31(2):112–122.

143. Moon JB, Kuehn DP, Chan G, Zhao L. Induced Velopharyngeal Fatigue Effects in Speakers With Repaired Palatal Clefts. The Cleft Palate-Craniofacial Journal. 2007;44(3):251–60.

144. Moon JB, Kuehn DP, Huisman JJ. Measurement of Velopharyngeal Closure Force during Vowel Production. The Cleft Palate-Craniofacial Journal. 1994;31(5):356–363.

145. Moon JB, Smith AE, Folkins JW, Lemke JH, Gartlan M. Coordination of Velopharyngeal Muscle Activity during Positioning of the Soft Palate. The Cleft Palate-Craniofacial Journal. 1994;31(1):45–55.

146. Moon JB, Thompson SA, Jaeckel E, Canady JW. Muscle Fiber Type Distribution in the Normal Human Levator Veli Palatini Muscle. The Cleft Palate-Craniofacial Journal. 1998;35(5):419–24.

147. Mugler III JP. Optimized Three-Dimensional Fast-Spin-Echo MRI. Journal of Magnetic Resonance Imaging. 2014;39(4):745–767.

148. Mukherjee P, Chung SW, Berman JI, Hess CP, Henry RG. Diffusion tensor MR imaging and fiber tractography: technical considerations. AJNR. American journal of neuroradiology. 2008;29(5):843–852.

149. Muthupillai R, Lomas DJ, Rossman PJ, Greenleaf JF, Manduca A, Ehman RL. Magnetic Resonance Elastography by Direct Visualization of Propagating Acoustic Strain Waves. Science. 1995;269(5232):1854–1857.

150. Narayanan SS, Nayak KS, Lee S, Sethy A, Byrd D. An approach to real-time magnetic resonance imaging for speech production. The Journal of the Acoustical Society of America. 2004;115(4):1771.

151. NessAiver MS, Stone M, Parthasarathy V, Kahana Y, Paritsky A. Recording high quality speech during tagged cine-MRI studies using a fiber optic microphone. Journal of Magnetic Resonance Imaging. 2006;23(1):92–97.

152. Nguyen DC, Patel KB, Skolnick GB, Skladman R, Grames LM, Stahl MB, Marsh JL, Woo AS. Progressive Tightening of the Levator Veli Palatini Muscle Improves Velopharyngeal Dysfunction in Early Outcomes of Primary Palatoplasty. Plastic and reconstructive surgery. 2015;136(1):131–141.

153. Noone RB, Randall P, Stool SE, Hamilton R, Winchester RA. The Effect on Middle Ear Disease of Fracture of the Pterygoid Hamulus during Palatoplasty. Cleft Palate Journal. 1973;10(1):23–33.

154. Noseworthy MD, Davis AD, Elzibak AH. Advanced MR Imaging Techniques for Skeletal Muscle Evaluation. Seminars in Musculoskeletal Radiology. 2010;14(2):257–268.

155. Nunthayanon K, Honda E, Shimazaki K, Ohmori H, Inoue-arai MS, Kurabayashi T, Ono T. Differences in Velopharyngeal Structure during Speech among Asians Revealed by 3-Tesla Magnetic Resonance Imaging Movie Mode. BioMed Research International. 2015.

156. Paal S, Reulbach U, Strobel-Schwarthoff K, Nkenke E, Schuster M. Evaluation of Speech Disorders in Children with Cleft Lip and PalateBewertung von Sprechauffälligkeiten bei Kindern mit Lippen-Kiefer-Gaumen-Spaltfehlbildungen. Journal of Orofacial Orthopedics. 2005;66(4):270–278.

157. Parish JM, Lyng PJ, Wisbey J. Compliance with CPAP in elderly patients with OSA. Sleep Medicine. 2000;1(3):209–214.

158. Park M, Ahn SH, Jeong JH, Baek R-MM. Evaluation of the levator veli palatini muscle thickness in patients with velocardiofacial syndrome using magnetic resonance imaging. Journal of Plastic, Reconstructive and Aesthetic Surgery. 2015;68(8):1100–1105.

159. Parker SE, Mai CT, Canfield MA, Rickard R, Wang Y, Meyer RE, Anderson P, Mason CA, Collins JS, Kirby RS, et al. Updated national birth prevalence estimates for selected birth defects in the United States, 2004-2006. Birth Defects Research Part A - Clinical and Molecular Teratology. 2010;88(12):1008–1016.

160. Pelland CM, Perry JL, Blemker SS. How Does the Tensor Veli Palatini Muscle Affect Velopharyngeal Closure? Cleft Palate-Craniofacial Journal. 2018;55(1_suppl, April):67.

161. Pelland CM, Tran T, Kollara L, Lin KY, Perry JL, Blemker SS. A Three-dimensional Subject-specific Computational Model Of Vpd Represents Velar Movements And LVP Function During Hypernasal Speech. The Cleft Palate-craniofacial Journal. 2017;54(3):e73.

162. Perkins JA, Lewis CW, Gruss JS, Eblen LE, Sie KCY. Furlow palatoplasty for management of velopharyngeal insufficiency: A prospective study of 148 consecutive patients. Plastic and Reconstructive Surgery. 2005;116(1):72–80.

163. Perry JL. Anatomy and physiology of the velopharyngeal mechanism. Seminars in Speech and Language. 2011;32(2):83–92.

164. Perry JL. Variations in velopharyngeal structures between upright and supine positions using upright magnetic resonance imaging. The Cleft Palate-Craniofacial Journal. 2011;48(2):123–33.

165. Perry JL, Chen JY, Kotlarek KJ, Haenssler A, Sutton BP, Kuehn DP, Sitzman TJ, Fang X. Morphology of the Musculus Uvulae In Vivo Using MRI and 3D Modeling Among Adults With Normal Anatomy and Preliminary Comparisons to Cleft Palate Anatomy. Cleft Palate-Craniofacial Journal. 2019:1055665619828226.

166. Perry JL, Kollara L, Kuehn DP, Sutton BP, Fang X. Examining age, sex, and race characteristics of velopharyngeal structures in 4- to 9-year-old children using magnetic resonance imaging. Cleft Palate-Craniofacial Journal. 2018;55(1):21–34.

167. Perry JL, Kotlarek KJ, Sutton BP, Kuehn DP, Jaskolka MS, Fang X, Point SW, Rauccio F. Variations in Velopharyngeal Structure in Adults With Repaired Cleft Palate. The Cleft palate-craniofacial journal. 2018;55(10):1055665617752803.

168. Perry JL, Kuehn DP. Three-dimensional computer reconstruction of the levator veli palatini muscle in situ using magnetic resonance imaging. The Cleft Palate-Craniofacial Journal. 2007;44(4):421–3.

169. Perry JL, Kuehn DP, Sutton BP. Morphology of the Levator Veli Palatini Muscle Using Magnetic Resonance Imaging. The Cleft Palate-Craniofacial Journal. 2013;50(1):64–75.

170. Perry JL, Kuehn DP, Sutton BP, Fang X. Velopharyngeal Structural and Functional Assessment of Speech in Young Children Using Dynamic Magnetic Resonance Imaging. The Cleft Palate-Craniofacial Journal. 2017;54(4):408–422.

171. Perry JL, Kuehn DP, Sutton BP, Gamage JK. Sexual Dimorphism of the Levator Veli Palatini Muscle: An Imaging Study. The Cleft Palate-Craniofacial Journal. 2014;51(5):544–552.

172. Perry JL, Kuehn DP, Sutton BP, Gamage JK, Fang X. Anthropometric Analysis of the Velopharynx and Related Craniometric Dimensions in Three Adult Populations Using MRI. The Cleft Palate-Craniofacial Journal. 2016;53(1):e1–e13.

173. Perry JL, Kuehn DP, Sutton BP, Goldwasser MS, Jerez AD. Craniometric and velopharyngeal assessment of infants with and without cleft palate. The Journal of Craniofacial Surgery. 2011;22(2):499–503.

174. Perry JL, Kuehn DP, Wachtel JM, Bailey JS, Luginbuhl LL. Using Magnetic Resonance Imaging for Early Assessment of Submucous Cleft Palate: A Case Report. The Cleft Palate-Craniofacial Journal. 2012;49(4):e35-41.

175. Perry JL, Sutton BP, Kuehn DP, Gamage JK. Using MRI for Assessing Velopharyngeal Structures and Function. The Cleft Palate-Craniofacial Journal. 2014;51(4):476–485.

176. Pet MA, Marty-Grames L, Blount-Stahl M, Saltzman BS, Molter DW, Woo AS. The Furlow Palatoplasty for Velopharyngeal Dysfunction: Velopharyngeal Changes, Speech Improvements, and Where They Intersect. The Cleft Palate-Craniofacial Journal. 2015;52(1):12–22.

177. Pigott RW. An analysis of the strengths and weaknesses of endoscopic and radiological investigations of velopharyngeal incompetence based on a 20 year experience of simultaneous recording. British Journal of Plastic Surgery. 2002;55(1):32–34.

178. Pigott RW. The Nasendoscopic Appearance of the Normal Palato-Pharyngeal Valve. Plastic and Reconstructive Surgery. 1969;43(1):19–24.

179. Poppelreuter S, Engelke W, Bruns T. Quantitative Analysis of the Velopharyngeal Sphincter Function During Speech. The Cleft Palate-Craniofacial Journal. 2000;37(2):157–165.

180. Ramsey RW, Street SF. The isometric length-tension diagram of isolated skeletal muscle fibers of the frog. Journal of Cellular and Comparative Physiology. 1940;15(1):11–34.

181. Rintala AE, Haapanen ML. The correlation between training and skill of the surgeon and reoperation rate for persistent cleft palate speech. British Journal of Oral and Maxillofacial Surgery. 1995;33(5):295–298.

182. Robin NH, Shprintzen RJ. Defining the Spectrum of Deletion 22q11.2. The Journal of Pediatrics. 2005;147(1):90–96.

183. Rosset A, Spadola L, Ratib O. OsiriX: An open-source software for navigating in multidimensional DICOM images. Journal of Digital Imaging. 2004;17(3):205–216.

184. Rouillon I, Maulet M, Roger G, Leboulanger N, Marlin S, Denoyelle F, Garabédian EN, Portnoï MF, Loundon N. Velopharyngoplasty for Noncleft Velopharyngeal Insufficiency. Archives of Otolaryngology–Head & Neck Surgery. 2009;135(7):652.

185. Ruotolo RA, Veitia NA, Corbin A, McDonough J, Solot CB, McDonald-McGinn D, Zackai EH, Emanuel BS, Cnaan A, LaRossa D, et al. Velopharyngeal anatomy in 22q11.2 deletion syndrome: A three-dimensional cephalometric analysis. Cleft Palate-Craniofacial Journal. 2006;43(4):446–456.

186. Sanchez GN, Sinha S, Liske H, Chen X, Nguyen V, Delp SL, Schnitzer MJ. In Vivo Imaging of Human Sarcomere Twitch Dynamics in Individual Motor Units. Neuron. 2015;88(6):1109–1120.

187. Satoh K, Wada T, Tachimura T, Shiba R. The effect of growth of nasopharyngeal structures in velopharyngeal closure in patients with repaired cleft palate and controls without clefts:a cephalometric study. British Journal of Oral and Maxillofacial Surgery. 2002;40(2):105–109.

188. Schenck GC, Perry JL, Fang X. Normative Velopharyngeal Data in Infants: Implications for Treatment of Cleft Palate. Journal of Craniofacial Surgery. 2016;27(6):1430–1439.

189. Seaver EJ, Kuehn DP. A Cineradiographic and Electromyographic Investigation of Velar Positioning in Non-Nasal Speech. The Cleft Palate Journal. 1980;17(3):216–226.

190. Shariat M, Mertens L, Seed M, Grosse-Wortmann L, Golding F, Mercer-Rosa L, Harris M, Whitehead KK, Li C, Fogel MA, et al. Utility of Feed-and-Sleep Cardiovascular Magnetic Resonance in Young Infants with Complex Cardiovascular Disease. Pediatr Cardiol. 2015;36:809–812.

191. Sherman MA, Seth A, Delp SL. What is a moment arm? Calculating muscle effectiveness in biomechanical models using generalized coordinates. Proceedings of the ASME Design Engineering Technical Conferences. 2013;2013:NIH Public Access.

192. Shinagawa H, Murano EZ, Zhuo J, Landman B, Gullapalli RP, Prince JL, Stone M. Tongue muscle fiber tracking during rest and tongue protrusion with oral appliances: A preliminary study with diffusion tensor imaging. Acoustical Science & Technology. 2008;29(4):291–294.

193. Shinagawa H, Ono T, Honda E-I, Masaki S, Shimada Y, Fujimoto I, Sasaki T, Iriki A, Ohyama K. Dynamic analysis of articulatory movement using magnetic resonance imaging movies: methods and implications in cleft lip and palate. The Cleft Palate-Craniofacial Journal. 2005;42(3):225–30.

194. Shprintzen RJ. Velo-cardio-facial syndrome: 30 Years of study. Developmental Disabilities Research Reviews. 2008;14(1):3–10.

195. Sie KC, Tampakopoulou DA, Sorom J, Gruss JS, Eblen L. Results with Furlow palatoplasty in management of Velopharyngeal Insufficiency. Plastic and reconstructive surgery. 2001;108(1):17–25.

196. Smith BE, Kuehn DP. Speech Evaluation of Velopharyngeal Dysfunction. The Journal of Craniofacial Surgery. 2007;18(2):251–261.

197. Sommerlad BC. A Technique for Cleft Palate Repair. Plastic and reconstructive surgery. 2003;112(6):1542–1548.

198. Sommerlad BC, Henley M, Birch MJ, Harland K, Moiemen N, Boorman JG. Cleft palate re-repair--a clinical and radiographic study of 32 consecutive cases. British Journal of Plastic Surgery. 1994;47(6):406–410.

199. Sommerlad BC, Mehendale F V., Birch MJ, Sell D, Hattee C, Harland K. Palate Re-Repair Revisited. The Cleft Palate-Craniofacial Journal. 2002;39(3):295–307.

200. Spruijt NE, ReijmanHinze J, Hens G, Vander Poorten V, Mink van der Molen AB. In search of the optimal surgical treatment for velopharyngeal dysfunction in 22q11.2 deletion syndrome: A systematic review. PLoS ONE. 2012;7(3).

201. Spruijt NE, Widdershoven JCC, Breugem CC, Speleman L, Homveld ILM, Kon M, Mink Van Der Molen AB. Velopharyngeal dysfunction and 22q11.2 deletion syndrome: A longitudinal study of functional outcome and preoperative prognostic factors. Cleft Palate-Craniofacial Journal. 2012;49(4):447–455.

202. Srivastava A, Klassen E, Joshi S, Jermyn IH. Shape Analysis of Elastic Curves in Euclidean Spaces. IEEE Transactions on Pattern Analysis and Machine Intelligence. 2011;33(7):1415–1428.

203. Srodon PD, Miquel ME, Birch MJ. Finite Element Analysis Animated Simulation of Velopharyngeal Closure. The Cleft Palate-Craniofacial Journal. 2012;49(1):44–50.

204. Sullivan SR, Marrinan EM, LaBrie RA, Rogers GF, Mulliken JB. Palatoplasty Outcomes in Nonsyndromic Patients With Cleft Palate. Journal of Craniofacial Surgery. 2009;20(Suppl 1):612–616.

205. Sumida K, Kashiwaya G, Seki S, Masui T, Ando Y, Yamashita K, Fujimura A, Kitamura S. Anatomical status of the human musculus uvulae and its functional implications. Clinical Anatomy. 2014;27(7):1009–1015.

206. Sumida K, Yamashita K, Kitamura S. Gross anatomical study of the human palatopharyngeus muscle throughout its entire course from origin to insertion. Clinical Anatomy. 2012;25(3):314–323.

207. Sutton BP, Conway CA, Bae Y, Seethamraju R, Kuehn DP. Faster dynamic imaging of speech with field inhomogeneity corrected spiral fast low angle shot (FLASH) at 3 T. Journal of Magnetic Resonance Imaging. 2010;32(5):1228–37.

208. Swanson EW, Sullivan SR, Ridgway EB, Marrinan EM, Mulliken JB. Speech outcomes following pharyngeal flap in patients with velocardiofacial syndrome. Plastic and Reconstructive Surgery. 2011;127(5):2045–2053.

209. Tian W, Redett RJ. New Velopharyngeal Measurements at Rest and During Speech: Implications and Applications. The Journal of Craniofacial Surgery. 2009;20(2):532–9.

210. Tian W, Yin H, Li Y, Zhao S-F, Zheng Q, Shi B. Magnetic resonance imaging assessment of velopharyngeal structures in Chinese children after primary palatal repair. The Journal of Craniofacial Surgery. 2010;21(2):568–77.

211. Tian W, Yin H, Redett RJ, Shi B, Shi J, Zhang R, Zheng Q. Magnetic Resonance Imaging Assessment of the Velopharyngeal Mechanism at Rest and During Speech in Chinese Adults and Children. Journal of Speech, Language, and Hearing Research. 2010;53(6):1595–615.

212. Tran T, Borowitz KC, Jenkins L, Blemker SS. Clinical Trial Evaluation of a New Feeding Mechanism for Babies Born With Cleft Palate. Cleft Palate-Craniofacial Journal. 2019;56(1S):66.

213. von Tycowicz C, Ambellan F, Mukhopadhyay A, Zachow S. An efficient Riemannian statistical shape model using differential coordinates: With application to the classification of data from the Osteoarthritis Initiative. Medical Image Analysis. 2018;43:1–9.

214. Vadodaria S, Goodacre TEE, Anslow P. Does MRI contribute to the investigation of palatal function? British Journal of Plastic Surgery. 2000;53:191–199.

215. Veerapandiyan A, Blalock D, Ghosh S, Ip E, Barnes C, Shashi V. The role of cephalometry in assessing velopharyngeal dysfunction in velocardiofacial syndrome. Laryngoscope. 2011;121(4):732–737.

216. Weiss JA, Gardiner JC. Computational Modeling of Ligament Mechanics. Critical Reviews in Biomedical Engineering. 2001;29(4):303–71.

217. Weiss JA, Maker BN, Govindjeed S. Finite element implementation of incompressible, transversely isotropic hyperelasticity. Computer methods in Applied Mechanics and Engineering. 1996;7825(96).

218. Widdershoven JCC, Stubenitsky BM, Breugem CC, MinkvanderMolen AB. Outcome of velopharyngoplasty in patients with velocardiofacial syndrome. Archives of Otolaryngology - Head and Neck Surgery. 2008;134(11):1159–1164.

219. Williams JC, Campagnola PJ. Wearable Second Harmonic Generation Imaging: The Sarcomeric Bridge to the Clinic. Neuron. 2015;88(6):1067–1069.

220. Windram J, Grosse-Wortmann L, Shariat M, Greer M-L, Crawford MW, Yoo S-J. Cardiovascular MRI without sedation or general anesthesia using a feed-and-sleep technique in neonates and infants. Pediatric Radiology. 2012;42:183–187.

221. Witt P, Cohen D, Grames LM, Marsh J. Sphincter pharyngoplasty for the surgical management of speech dysfunction associated with velocardiofacial syndrome. British Journal of Plastic Surgery. 1999;52(8):613–618.

222. Witt PD, Wahlen JC, Marsh JL, Grames LM, Pilgram TK. The Effect of Surgeon Experience on Velopharyngeal Functional Outcome following Palatoplasty: Is There a Learning Curve? Plastic and Reconstructive Surgery. 1998;102(5):1375–1384.

223. Witzel MA, Stringer DA. Methods of Assessing Velopharyngeal Function. In: Bardach J, Morris HL, editors. Multidisciplinary Management of Cleft Lip and Palate. W.B. Saunders Company; 1990. p. 763–776.

224. Woo AS. Velopharyngeal Dysfunction. Seminars in Plastic Surgery. 2012;26(4):170–177.

225. Woo AS, Skolnick GB, Sachanandani NS, Grames LM. Evaluation of two Palatal Repair Techniques for the Surgical Management of Velopharyngeal Insufficiency. Plastic and reconstructive surgery. 2014;134(4):588e–596e.

226. Ysunza A, Carmen Pamplona M, Santiago Morales MA. Velopharyngeal valving during speech, in patients with velocardiofacial syndrome and patients with non-syndromic palatal clefts after surgical and speech pathology management. International Journal of Pediatric Otorhinolaryngology. 2011;75(10):1255–1259.

227. Ysunza A, Pamplona MC, Molina F, Hernández A. Surgical planning for restoring velopharyngeal function in velocardiofacial syndrome. International Journal of Pediatric Otorhinolaryngology. 2009;73(11):1572–1575.

228. Zajac FE. Muscle and Tendon: Properties, Models, Scaling, and Application to Biomechanics and Motor Control. Critical Reviews in Biomedical Engineering. 1989;17(4):359–411.

229. Zebra Medical Technologies, Mountain View, California, USA.